

Metamodel Based Optimization for Dynamic Blade Pitch Control on a Vertical Axis Wind Turbine Using Analytical and CFD Methods

by

Pablo Andrés Guevara Álvarez

B.Sc. (Mechanical Engineering), Escuela Superior Politécnica del Litoral, 2014

Thesis Submitted in Partial Fulfillment of the
Requirements for the Degree of
Master of Applied Science

in the
School of Mechatronic Systems Engineering
Faculty of Applied Sciences

© Pablo Andrés Guevara Álvarez 2019

SIMON FRASER UNIVERSITY

Fall 2019

Copyright in this work rests with the author. Please ensure that any reproduction or re-use is done in accordance with the relevant national copyright legislation.

Approval

Name: Pablo Andrés Guevara Álvarez

Degree: Master of Applied Science (Mechatronic Systems Engineering)

Title: Metamodel Based Optimization for Dynamic Blade Pitch Control on a Vertical Axis Wind Turbine Using Analytical and CFD Methods

Examining Committee:

Chair: Amr Marzouk
Lecturer

Krishna Vijayaraghavan
Senior Supervisor
Associate Professor

Siamak Arzanpour
Supervisor
Associate Professor

Gary Wang
Internal Examiner
Professor

Date Defended/Approved: August 19, 2019

Abstract

In this study, the blade pitching motion on a representative (12 kW) vertical axis wind turbine (VAWT) is optimized over a wide range of operating conditions. The pitching is referred to as active blade pitching (ABP) when it is not constrained by a predetermined motion, while the operating condition is referred to as the tip speed ratio (TSR). Computational fluid dynamics (CFD) simulations are used to estimate the instantaneous torque produced by the VAWT blades. The torque is considered the system output and is dependent on the ABP which serves as the system input.

This work initially used a preliminary ABP derived using an analytic model; the VAWT was then simulated at a TSR of 2.3 with fixed blades using an analytic-ABP strategy. The simulation with the analytic-ABP generated a 33.4% increase in torque output compared to the fixed pitch strategy simulation.

The analytic-ABP curve was then approximated by a function of two variables, via parameterization of the ABP. The parameters of this ABP are the optimization variables of a response surface methodology (RSM) optimization, the objective function being the CFD “black-box” simulation and the output variable being the average torque of a blade. The optimization used a three-level full factorial design (FFD) as the design of experiment (DOE) strategy in order to sample the function with an initial set of points, generate a metamodel, and search for the optimum. The ABP derived from this method, termed the FFD-ABP, was simulated; the results show that it increased the torque output by 15.5% relative to the previous analytic-ABP.

A new optimization procedure is proposed in this work. It starts from the simulation results of the analytic-ABP as well as $+2^\circ$ and -2° offset perturbations. The optimization procedure generates an optimal ABP using a modified quadratic regression metamodel over a discretized domain; the metamodel is updated with the response of the first optimal-ABP to generate a second optimal-ABP. The procedure is repeated until the ABP converges into a narrow band. The optimal-ABP simulations resulted in a 6.5% increase in torque output with fewer function calls compared to the previous FFD-ABP.

The optimization procedure was extended to several TSRs and the data used to develop a governing function and power performance charts. The governing function was based on a novel nonlinear curve fit model and it estimated the pitch based on the TSR and azimuthal angle. The maximum power operation point is increased by 13% and the torque performance at low TSR is improved.

Keywords: Active blade pitch (ABP) control; Computational fluid dynamics (CFD); Metamodel-based optimization; Response surface methodology (RSM); Tip speed ratio (TSR); Vertical axis wind turbine (VAWT)

To my Parents

To my Family

To my Friends

To everyone who supported this work directly or indirectly

*To all researchers whose passion and work is to extend the
frontiers of science*

Acknowledgments

“The secret to creativity is knowing how to hide your sources” – Albert Einstein

My interpretation of this quote is very clear: new research builds upon the work of others, no one starts from scratch. In that regard my sincere acknowledgment to my supervisor Dr. Krishna Vijayaraghavan from the school of Mechatronic Systems Engineering at Simon Fraser University, for his support, expertise, and previous work on computation fluid dynamics; his contribution was invaluable and made it possible for this work to be built on the foundation of his.

I would like to thank my co-supervisor, Dr. Siamak Arzapour, from the school of Mechatronic Systems Engineering, for his insightful comments regarding computational fluid dynamics and for his advice on the groundwork models for this research.

I would like to thank professor Dr. Gary Wang, also from the school of Mechatronic Systems Engineering , who provided his time to review this work and discussed with me several guidelines on the subject of optimization theory; his suggestions led to improvements in this work.

My deep esteem to Phillip Rochester who not only collaborated in this work but became a friend; his enthusiasm for wind turbines science and computational fluid dynamics simulations and his knowledge of experimental tests with vertical axis wind turbines were essential to the development and completion of this research thesis.

I would like to acknowledge the funding from NSERC Discovery Grant (RGPIN418375) and Mitacs Globalink Research Internship program 2017, which supported Philip Rochester’s internship at SFU.

I would like to acknowledge the institutional support of WestGrid and Compute Canada; this work would not have been possible without the computational resources they provided. I feel a responsibility to cite their shared goal, *“The acceleration of innovation by deploying advanced research computing (ARC) for the Canadian research community to enable world-class research.”*

I would like to acknowledge the Government of the Republic of Ecuador, which funded my studies at SFU through the scholarship program 2016 (SENECYT-DMPF-2016-0399-CO).

Many thanks to Tom Moss Gamblin member of the Editor's Association of Canada, for his assistance in proofreading the final version of this work.

Finally, I must express my gratitude to my parents, family, and old and new friends, all of whom have encouraged me to take on challenges and supported me on a personal basis. *Thank you all.*

Table of Contents

Approval.....	ii
Abstract.....	iii
Dedication.....	v
Acknowledgments.....	vi
Table of Contents.....	viii
List of Tables.....	x
List of Figures.....	xi
List of Acronyms.....	xiii
List of Notations.....	xiv
Chapter 1. Introduction.....	1
1.1. Literature Review on Flow Modeling.....	1
1.2. Review of Metamodel-Based Optimization.....	3
1.3. Purpose and Motivation.....	4
1.4. Vertical Axis Wind Turbine Study Case.....	5
1.5. Thesis Outline.....	7
Chapter 2. Computational Fluid Dynamics Setup.....	9
2.1. Mesh implementation.....	9
2.2. Case Structure Setup.....	12
2.2.1. Computational Parameters.....	12
2.2.2. Tabulated Movement for Rotating Fluid Domains.....	13
2.2.3. Acceleration Profile.....	14
2.3. CFD Validation for NACA0021 Airfoil.....	15
2.4. VAWT CFD 2D Simulation and Experimental Data.....	18
2.4.1. Mesh and Time-Step Independence.....	19
2.4.2. CFD Validation Using Previously Published Experiments.....	20
Chapter 3. Preliminary Active Blade Pitching for VAWT.....	26
3.1. Blade Element Model Development.....	26
3.2. Blade Element Model Implementation.....	30
3.3. Analytically Derived ABP for TSR 2.3.....	31
3.4. Comparison of Analytic-ABP Versus Fixed-Pitch.....	33
Chapter 4. Optimization of Parameterized Active Blade Pitching Function.....	35
4.1. Black-Box Optimization Overview.....	35
4.2. Parameterization of the Input Stimulus.....	36
4.3. Response Surface Methodology Description.....	37
4.4. Study Case for TSR = 2.3.....	39
4.5. Comparison of FFD-ABP Versus Analytic-ABP.....	42

Chapter 5. Optimization of Active Blade Pitching at Discrete Azimuthal Angles	45
5.1. Methodology.....	45
5.2. Initial Data Set Generation.....	46
5.3. Metamodel Optimization of Torque Versus Pitch	48
5.4. CFD Simulation of the First optimal ABP	50
5.5. Iteration and Convergence Procedure	51
5.6. Comparison of Optimal-ABP Versus FFD-ABP.....	52
Chapter 6. Optimization Procedure Over a Wide TSR Range.....	56
6.1. ABP as a Function of TSR and Azimuthal Angle.....	56
6.2. Torque Performance Curve	59
6.3. Power Performance for Maximum Power Tracking	60
6.4. Torque Performance at Low TSR	61
Chapter 7. Conclusions and Future Work	64
References.....	66
Appendix A. CFD Case Description in OpenFOAM3.0.1	70
Appendix B. Estimation of Drag in VAWT Struts	73
Appendix C. MATLAB Scripts to Implement the Analytic-ABP	77
Appendix D Mesh Generation Script Files for 2D VAWT Model	85
Appendix E. Script File for Generating Tabulated Data.....	86
Appendix F. VAWT Simulation Script Files OpenFOAM.....	87
Appendix G. Metamodel Implementation in MATLAB.....	88
Appendix H. Simulation Data and Post-Processed Results	89

List of Tables

Table 1.1.	VAWT characteristics.....	5
Table 2.1.	Boundary conditions.....	9
Table 2.2.	Air transport properties.....	12
Table 2.3.	Simulation results, $y^+ = 8$, $Co = 8$, mesh of 163,666 cells.....	20
Table 4.1.	Optimization variables.....	39
Table 4.2.	Initial FFD set.....	41
Table 4.3.	Second FFD set.....	42
Table 5.1.	Quantitative attributes of optimization procedures.....	54
Table 5.2.	Qualitative attributes of the optimization procedures.....	55
Table 6.1.	Curve fitting constants.....	57
Table 6.2.	Normalized mean square error by TSR.....	58

List of Figures

Figure 1.1.	Block diagram, input and output data	4
Figure 1.2.	H-Darrieus VAWT schematic.....	6
Figure 1.3.	2D VAWT model	6
Figure 2.1.	Computational domain for the VAWT (not to scale).....	10
Figure 2.2.	Mesh fields on the computational domain.....	11
Figure 2.3.	Tabulated data file structure	13
Figure 2.4.	Black-box diagram of the bash script for the tabulated data files	14
Figure 2.5.	Motion profile within the tabulated data	14
Figure 2.6.	Domain dimensions for airfoil validations.....	15
Figure 2.7.	High-density mesh snapshots, cell count $\approx 274,000$	15
Figure 2.8.	Boundary layer cells thickness: $y^+ = 8$ (left), $y^+ = 0.8$ (right).....	16
Figure 2.9.	Mesh independence study, $Re = 360,000$, wall cells at $y^+ = 0.8$; lift coefficient (left) and drag coefficient (right).....	17
Figure 2.10.	Simulation versus experiment comparison, $Re = 360,000$, wall cells at $y^+ = 0.8$; lift coefficient (left) and drag coefficient (right)	17
Figure 2.11.	Mesh independence study, $Re = 360,000$, wall cells at $y^+ = 8$; lift coefficient (left) and drag coefficient (right).....	18
Figure 2.12.	Simulation versus experiment comparison, $Re = 360,000$, wall cells at $y^+ = 8$; lift coefficient (left) and drag coefficient (right)	18
Figure 2.13.	Simulation mesh and time-step independence study.....	19
Figure 2.14.	H-Darrieus rotor VAWT	20
Figure 2.15.	Real design considerations for a) blades and b) struts	21
Figure 2.16.	Comparison of experimental and CFD results	23
Figure 2.17.	Normalized velocity field with fixed 2° pitch, $TSR = 3.3$, $\theta = 0^\circ$, time $t = 10.9$ s	24
Figure 2.18.	Normalized pressure field with fixed 2° pitch, $TSR = 3.3$, $\theta = 0^\circ$, time $t = 10.9$ s	24
Figure 3.1.	VAWT kinematics diagram, for any azimuthal angle.....	26
Figure 3.2.	VAWT force diagram for upwind sweep ($90^\circ < \theta < 270^\circ$).....	29
Figure 3.3.	VAWT force diagram for downwind sweep ($\theta < 90^\circ$ or $\theta > 270^\circ$)	29
Figure 3.4.	Angle of Attack functions, $TSR = 2.3$	31
Figure 3.5.	Analytic-ABP control function, $TSR = 2.3$	32
Figure 3.6.	Torque output of a VAWT blade, fixed pitch at 2° and analytic-ABP, $U_\infty = 7.78$, $TSR = 2.3$	33
Figure 4.1.	CFD simulation as the black-box with periodic pitching of blades as input and periodic instantaneous torque output.....	35
Figure 4.2.	Block diagram schematic for a black-box optimization with parameterization of input stimulus and output response	36

Figure 4.3.	Effects of amplitude a and skewness b in equation (4.1)	37
Figure 4.4.	Optimization procedure block diagram	39
Figure 4.5.	Initial parameter values for amplitude a and skewness b	40
Figure 4.6.	First FFD data set and curve fit by quadratic regression.....	41
Figure 4.7.	Second FFD data set and curve fit by quadratic regression.....	42
Figure 4.8.	Input stimulus for a VAWT blade: analytic-ABP and FFD-ABP	43
Figure 4.9.	Torque output of a VAWT blade using analytic-ABP and optimization- based FFD-ABP, $U_\infty = 7.78$, $TSR = 2.3$	44
Figure 5.1.	Procedure flow diagram for point-wise metamodel optimization	46
Figure 5.2.	Analytic-ABP functions, offsets 0, +2, -2, $TSR = 2.3$	47
Figure 5.3.	Torque output using the three initial ABP functions, $TSR = 2.3$	47
Figure 5.4.	Metamodel for three data points at $\theta = 270^\circ$, $TSR = 2.3$	48
Figure 5.5.	Metamodel for three data points at $\theta = 200^\circ$, $TSR = 2.3$	49
Figure 5.6.	Convex metamodel case at $\theta = 107^\circ$, $TSR = 3.3$	49
Figure 5.7.	Torque output of 1 st procedure run, $TSR = 2.3$	50
Figure 5.8.	Optimum ABP function convergence.....	51
Figure 5.9.	Torque function convergence	52
Figure 5.10.	Input stimulus for a VAWT blade, FFD-ABP and optimal-ABP.....	53
Figure 5.11.	Torque output for a VAWT blade, using the FFD-ABP and the optimal- ABP, $U_\infty = 7.78$, $TSR = 2.3$	54
Figure 6.1.	Optimized ABP for multiple TSRs.....	56
Figure 6.2.	3D surface plot with nonlinear curve fit for optimized pitching.....	58
Figure 6.3.	Effect of TSR on α_0	59
Figure 6.4.	Optimal ABP torque performance.....	60
Figure 6.5.	Comparison of VAWT C_p performance	61
Figure 6.6.	Torque profile at $TSR = 0.5$ for ABP and fixed-pitch strategies.....	62
Figure 6.7.	Torque profile at $TSR = 1.0$ for ABP and fixed pitch strategies.....	63

List of Acronyms

ABP	Active blade pitching
AOA	Angle of attack
ARC	Advanced research computing
BET	Blade element theory
BEM	Blade element model
BEMT	Blade element momentum theory
CM	Cascade model
CFD	Computational fluid dynamics
DOE	Design of experiments
DMST	Double multiple stream-tube
FFD	Full factorial design
MSM	Multiple stream-tube model
MT	Momentum theory
NACA	National advisory committee for aeronautics
NMSE	Normalized mean square error
RMSE	Root mean square error
HAWT	Horizontal axis wind turbines
SST	Shear stress transport
RSM	Response surface methodology
TSR	Tip speed ratio
VAWT	Vertical axis wind turbine
VM	Vortex model

List of Notations

A	VAWT cross section sweep area
C	VAWT blade chord length
D	VAWT cross section diameter
r	VAWT cross section radius
H	VAWT cross section height
L	VAWT blade length
P_{VAWT}	VAWT rated power
Bld	VAWT blade number
Re	Reynolds number
Re_L	Local Reynolds number on a VAWT blade
U_∞	Free-stream wind speed (wind speed far away)
U_{exp}	Wind speed experienced by a VAWT blade
Co	Courant number
y^+	Dimensionless height of a cell adjacent to the blade wall
ω	VAWT rotational speed
ρ	Air density
μ	Air dynamic viscosity
T	Instantaneous VAWT torque
T_{CFD}	Average VAWT torque by CFD data
T_{eff}	Effective average torque of VAWT
η_{chord}	Compensation factor for chord length variation
η_{vortex}	Compensation factor for tip vortex losses
$T_{Dragstruts}$	Total struts drag torque
$T_{Drag_{1-rod}}$	Strut drag torque, one rod
T_{Bld}	Torque on a single VAWT blade
t	Time
C_P	Power coefficient
C_T	Torque coefficient
C_L	Lift coefficient
C_D	Drag coefficient
F_L	Lift force

F_D	Drag force
\vec{r}_1	Position of blade chord center on $-\emptyset$ rotated frame
\vec{r}_2	Position of forces action point on $-\emptyset$ rotated frame
A_{Bld}	Blade reference area ($C \times H$ or $C \times L$)
θ	Azimuthal angle of a blade (or azimuthal position)
θ_p	Pitch angle of a blade
$\theta_{p_{opt}}$	Optimum pitch angle
α	Angle of attack of a blade
α_0	Angle of attack for a blade at zero pitch
α_{opt}	Optimum angle of attack
\emptyset	Angle of U_{exp} relative to the global x coordinates
P	Pitch angle of a blade as a function of θ
T_0	Blade torque corresponding to analytic ABP
T_{+2}	Blade torque corresponding to analytic ABP offset +2
T_{-2}	Blade torque corresponding to analytic ABP offset -2

Chapter 1.

Introduction

Wind turbines are classified into vertical axis wind turbines (VAWTs) and horizontal axis wind turbines (HAWTs). Compared to HAWTs, VAWTs emit less noise, are easier to install and maintain owing to the on-ground generator, are omnidirectional, and can better handle turbulent winds [1]. However, VAWTs have lower efficiency compared to HAWTs and lift-based VAWTs, a subclass of VAWTs, cannot self-start [2]. Nonetheless, VAWTs offer an opportunity to expand wind energy extraction in nontraditional and urban environments. In HAWTs and VAWTs, the magnitude and direction of the instantaneous forces are a function of the angle of attack (AOA; i.e., the orientation of the blade relative to the effective wind flow). As will be seen later, the AOA of the individual blades changes as the VAWT rotates. Consequently, a single AOA may not generate optimal power. This makes the VAWT a good candidate for active blade pitching (ABP), in which the blades are cyclically pitched (rotated) about their axis to maximize the instantaneous torque [1,3].

1.1. Literature Review on Flow Modeling

The blade element momentum theory (BEMT) [4], double multiple stream tube model (DMSM) [5,6], cascade models (CM) [7,8], and vortex models (VM) [9,10] are a few of the most representative analytic models used to calculate forces acting on wind turbine blades. These models have been widely used as a first approach to optimize VAWTs [11,12]. BEMT is a two-step analytic approach consisting of blade element theory (BET) and momentum theory (MT) analyses. BET extrapolates the forces acting on an elemental section of the blade in freestream to the entire blade while MT models the effective flow field approaching and leaving the VAWT based on a momentum balance, effectively modeling the flow field variation due to the very presence of the VAWT [4]. The DMSM is one of several models based on BEMT. Here the flow is divided into several streams parallel to the main flow, taking into account the flow variation between the upstream and downstream sections [13]. CM analysis begins by rearranging the blades in a horizontal line in a sequence known as a cascade; the

potential flow field with the induced velocity field of the wakes are then predicted with semi-empiric equations [7,8]. In VM analysis, the potential flow fields under the influence of the wake vorticity produced by the blade are replaced by lifting-line vortices and a new flow field is computed with analytic formulas [9,10]. A comprehensive review of these analytic models can be found in the literature [11,12].

Kosaku et al. [14] used a BEMT model to develop a pitch control strategy for VAWTs for various tip speed ratios (TSRs), showing the dependence of the control function on the TSR. Zhang et al. [15] used another BEMT model to generate several performance curves and concluded that ABP can significantly improve the power coefficient at low TSRs. They noted, however, that if the TSR was already optimized for maximum power, active pitching resulted in only a small increase in the power coefficient. Chen et al. [1] got similar results and concluded that ABP would result in higher power at low TSRs. These studies determined that the pitching function was predominantly sinusoidal in shape with a positive pitch angle on the upwind area and negative pitch angles on the downwind area, and that the pitching magnitude decreased at high TSRs [1,15].

While analytic formulas require less computational effort to determine the pitching function, they fail to consider all physical phenomena. For instance, the very presence of the VAWT will result in vortices, wind slowdown or deflection close to the VAWT (i.e., the wind speed near the VAWT is less than the freestream velocity owing to the VAWT's presence), linear and rotational momentum transfer to the wind domain, and viscous dissipation effects [11]. These physical phenomena are better handled by CFD simulations, with carefully set up CFD results very closely matching experimental ones [16]. However, simulating ABP control using CFD is rather challenging as it requires multiple rotating domains (as discussed later in the thesis), whereas past literature has predominantly focused on optimizing the performance of fixed-blade VAWTs. Howell et al. [17] showed that 2D and 3D simulations agree well with experimental results up to the experimental maximum power point. Their study suggests that 2D models can overpredict the torque at high TSRs while 3D models tend to underpredict it. A full 3D setup of the overall flow field on a straight-bladed VAWT was developed by Zhang et al. [16], who showed a close match with experimental results; hence CFD can predict VAWT performance. Rezaeiha et al. [18] studied the effect of fixed nonzero pitch angles on the power and torque of a VAWT. The study concluded that a positive fixed pitch

increased the torque in the section facing the wind while increasing negative torque on the downwind area, while negative pitch angles were shown to have the opposite effect. The study then optimized the fixed pitch angle for a particular TSR and VAWT geometry. Kirke et al. [19] studied a VAWT whose blades were pivoted at the leading edge, and the trailing edge was connected to a pitch amplitude ring that generated sinusoidal pitching of fixed magnitude. This study utilized both CFD simulations and experiments to establish the viability of the pitch amplitude ring. However, the study did not aim to optimize the pitching motion, and the effectiveness of the approach is limited to a narrow range of working conditions. Abdalrahman et al. [20] proposed a pitch angle controller using a multilayer perceptron artificial neural network (MLP-ANN). The MLP-ANN is trained using the power coefficients obtained from fixed-blade CFD simulations. The controller then maps an optimal pitch angle for the current TSR and azimuthal angle using the MLP-ANN. It should be noted that the study does not truly optimize the pitching motion based on pitching CFD simulations but instead relies on fixed-blade simulations, which do not capture nonlinear secondary aerodynamic effects. Furthermore, their “optimum” is not a smooth function but several “fix pitch angles” within a given azimuthal angle range.

1.2. Review of Metamodel-Based Optimization

When performing optimization, we aim to manipulate a set of inputs known as design variables to maximize (or minimize) an objective function. Optimization requires multiple experiments or evaluations of computationally expensive models of the underlying system for different permutations of the design variables. Metamodeling techniques aim to speed up the optimization by constructing a simplified representative model of the system, the metamodel. This methodology is also known as “black-box optimization” as the physical model of the system can be unknown (or ignored) and the system is treated as a “black box.”

We begin by simultaneously evaluating the underlying system at a predetermined set of points in the design space. These points may either be selected randomly or strategically with design of experiments (DOE) [21]. Since the metamodel needs to be either concave or convex for an optimum to exist, we typically use a second-order polynomial of the design variables as a metamodel [22]. We then determine the coefficients of the polynomial using regression analysis [23]. We can now determine the

optimal values of the design variable by applying our optimization algorithm to the metamodel. The system is evaluated again with the new optimal value of the design variable and the new response data is used to refine the metamodel. This procedure is repeated until the parameters converge to their optimal values. Figure 1.1 shows a block diagram for a black-box optimization. More information on metamodeling and DOE techniques can be found in Gunst et al. [24] and Box et al. [25].

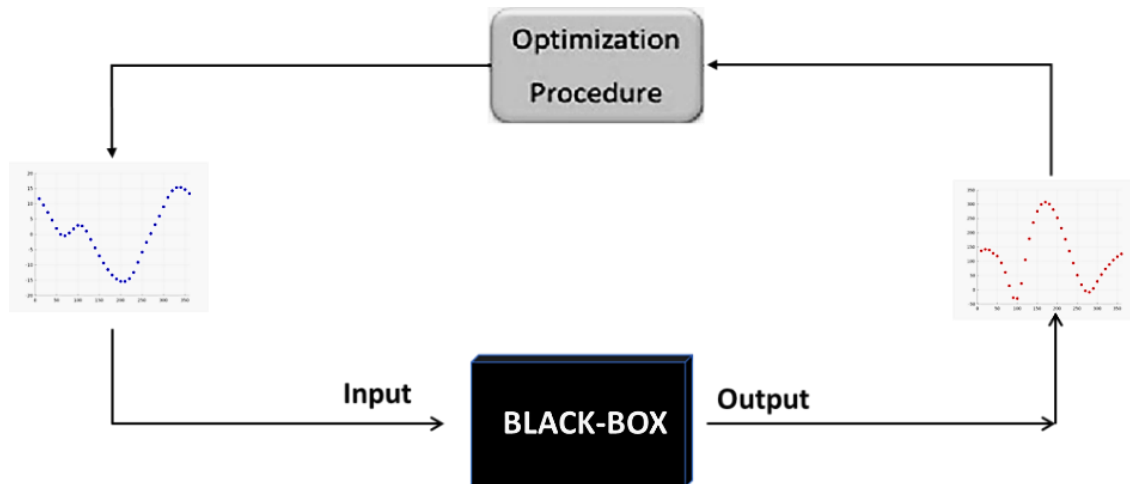


Figure 1.1. Block diagram, input and output data

In this work, the VAWT system is simulated by a CFD model, which is the black-box. The system output response will be dependent on the input stimulus, and will be the periodic torque produced by the blades; the input will be the periodic pitching of the blades. The optimization procedure collects input and output data to estimate a candidate input which is meant to maximize (or minimize) the output.

1.3. Purpose and Motivation

Most literature on ABP optimization for VAWTs uses analytical models. The literature that uses CFD simulations mainly addresses fixed-blade optimization, while those studies that do address ABP do not optimize but instead focus on a comparison with analytic and experimental models. The experimental literature on VAWTs is mainly for power performance testing, passive blade pitching testing (using strings or cams), and fixed-blade pitch optimization. In summary, the non-analytical models which do examine ABP do not present an optimization of the control function based on experimental or simulation data.

This work aims to improve VAWT performance by developing a procedure that optimizes the ABP using simulation data. To improve convergence speed, the analytical model computes a preliminary ABP; the model is derived from a blade element theory (BET) analysis [4] applied to VAWTs. Since the analytical model does not capture any secondary fluid dynamics, a CFD-based optimization procedure is used to refine the ABP; using a metamodel that is progressively updated with results from intermediate simulations. The metamodeling methodology allows us to run multiple simulations in parallel while significantly reducing the overall number of simulations required, as seen in earlier literature [26,27]. The optimization procedure is repeated for different TSRs in order to determine an optimal ABP as a function of the TSR.

To the best of the author's knowledge, there are no metamodels procedures for ABP optimization on VAWTs via CFD simulations over a wide range of TSRs. These results have the potential to solve challenges in VAWT such as inability to self-start and also to improve maximum power output. Furthermore, the procedure currently using simulation data is compatible with experimental results by means of measuring instantaneous torque using piezoelectric sensors [28] [29].

1.4. Vertical Axis Wind Turbine Study Case

A representative 12-kW VAWT has been chosen for this study; its parameters are summarized in Table 1.1. This model was chosen to match the model used in Kjellin et al. [30], whose experimental data is used in the validation study.

Table 1.1. VAWT characteristics

Parameter	Variable	Value
Rated power	P_{VAWT}	12 kW
Rated rotation speed	ω	127 rpm
Rated blade tip speed ratio	TSR	3.3
Rated wind speed	U	12 m/s
Number of blades	Bl	3
Swept area	A	30 m ²
Turbine radius	R	3 m
Turbine diameter	D	6 m
Blade length (VAWT height)	L (H)	5 m
Chord length	C	0.25 m
Airfoil profile		NACA 0021

A 3D schematic of the VAWT is shown in Figure 1.2. The airflow is characterized by the freestream wind speed U_∞ . The VAWT blades spin at a radius r from the center with a rotational speed ω . The instantaneous linear velocity of a blade is ωr .

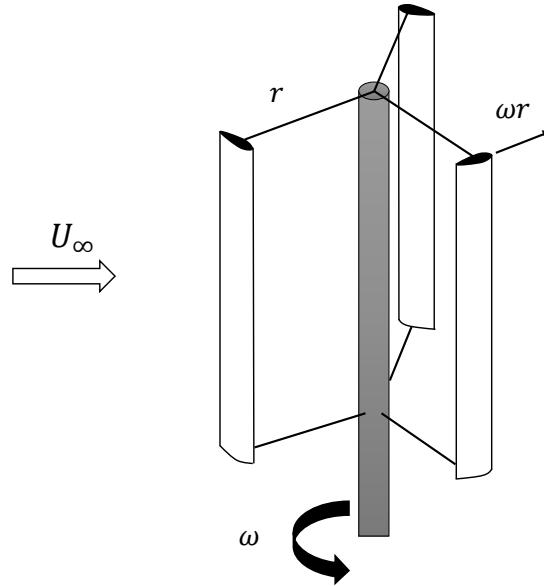


Figure 1.2. H-Darrieus VAWT schematic

Figure 1.3 shows a 2D section along the rotation axis with the upwind and downwind areas; this 2D model is used in this work to derive the analytic-ABP and for the rest of the CFD simulations.

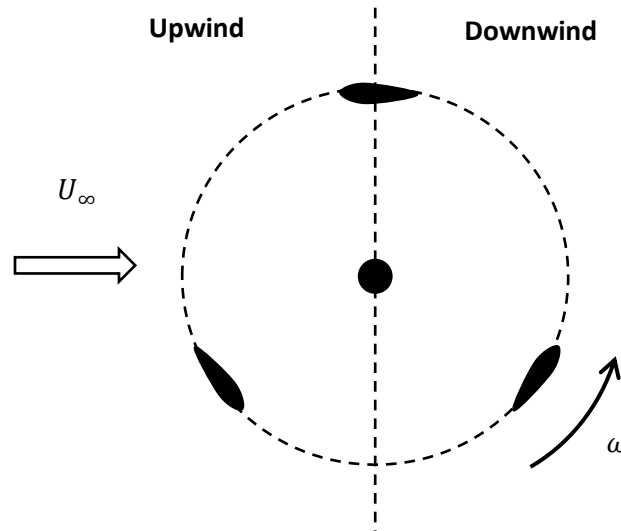


Figure 1.3. 2D VAWT model

1.5. Thesis Outline

Chapter 1 has summarized current research on VAWT analysis; these studies show that a performance increase in VAWTs is achieved when using a pitching strategy. Given the lack of research on ABP using simulations, this work proposes a CFD optimization methodology for VAWT ABP. Compared to a traditional optimization methodology, the procedure generated a better solution with fewer function calls, as demonstrated in the upcoming Chapters.

Chapter 2 describes the CFD simulation setup. It begins with the mesh (Section 2.1), in which the fluid domain around the VAWT is partitioned into embedded moving regions. The case setup in Section 2.2 is done in OpenFOAM 3.01 for a time-dependent (transient) simulation and dynamic mesh. A validation study for the airfoil (Section 2.3) compares the lift and drag coefficient generated by the simulations against experiments; the Reynolds number (Re) of the airfoil validation is equivalent to the VAWT blades in operation. The chapter ends (Section 2.4) with an experimental and simulation comparison of the VAWT's power coefficient (C_p) over a wide TSR operating range.

In Chapter 3, a blade element model (BEM) is used to analyze the VAWT and develop an equation that estimates the VAWT torque based on the angle of attack (α) of the blade. The model assumes freestream flow behavior at the blades at an instantaneous blade position with no secondary effects. An optimal pitch is computed based on the optimal angle of attack (α_{opt}), evaluated for a 360° blade cycle (in 1° increments) at a TSR of 2.3. The pitching function is termed analytic-ABP. Finally, simulations are run using the fixed-blade pitch strategy and the analytic-ABP strategy and we compare the steady-state blade torque given by the two simulations.

Chapter 4 presents a traditional black-box optimization approach for the VAWT ABP. First, the analytic-ABP is approximated by a function of two variables, namely the optimization variables of a response surface methodology (RSM) optimization; the simulation is defined as the (black-box) objective function and the average torque of a blade as the output variable (to be maximized). The optimization used a three-level full factorial design (FFD) as design of experiment (DOE) strategy to determine the initial set

of points in the design space (needed to generate the quadratic metamodel). We term the ABP derived from this method the FFD-ABP. A simulation is run with this control strategy to obtain the steady-state blade torque. The new blade torque data is then compared with the data obtained previously in Chapter 3.

Chapter 5 proposes a novel CFD optimization procedure. In contrast to Chapter 4, a point-wise optimization is done on the ABP. The analytic-ABP is perturbed by $\pm 2^\circ$ at each azimuthal angle (in 1° increments) and a metamodel is constructed for each azimuthal position. The metamodels are used to generate a new optimal ABP (the first step of the procedure). The optimal ABP is simulated and the results are used to update the discretized metamodels and generate a second optimal ABP. The procedure is repeated until the optimal ABP converges into a narrow band. Finally, the steady-state blade torque is compared with the results obtained previously in Chapter 4.

In Chapter 6 the procedure is extended for other TSR operating points. The new data is used to develop a governing function with a nonlinear curve fit model, and the VAWT torque and power performance charts are developed and discussed.

The thesis concludes with Chapter 7, summarizing important results and suggesting future research to extend the scope of the present work.

Chapter 2.

Computational Fluid Dynamics Setup

This chapter describes the mesh setup and the computational parameters of the simulation. A 2D CFD model is used as 3D models are significantly more expensive. Next, the 2D CFD simulation results are compared to experimental results for a single airfoil and for a fixed pitch VAWT. The turbulence model, mesh density, and computational parameters thus validated are used in subsequent chapters.

2.1. Mesh implementation

In order to simulate ABP, the blades would need to simultaneously rotate about the axis of the VAWT and pitch (rotate) about their own axes. To this end, the domain is divided into multiple regions as shown in Figure 2.1. The relative dimensions were adapted from the computational domain used in Rezaeiha et al. [18]. While Rezaeiha et al. [18] used a domain height of $20 \times D$ with no-slip walls, we have used a domain height of $10 \times D$ with slip walls. While Rezaeiha et al. [18] used a downstream length of $25 \times D$, we determined that a downstream domain length of $15 \times D$ is sufficient for the trailing flow turbulence to develop fully; further increase in the downstream domain distance did not affect simulation results. The boundary conditions for the mesh patches are listed in Table 2.1

Table 2.1. Boundary conditions

B. C.	Type	Value	Description
Inlet (left)	Velocity inlet	TSR dependent	Uniform fluid velocity at the wall
Outlet (right)	Pressure outlet	0	Uniform and zero at the wall
Upper wall	Fixed walls	Slip condition	No shear force at the wall
Lower wall	Fixed walls	Slip condition	No shear force at the wall
Blades	Moving wall	No-slip condition	Fluid velocity equal to the wall

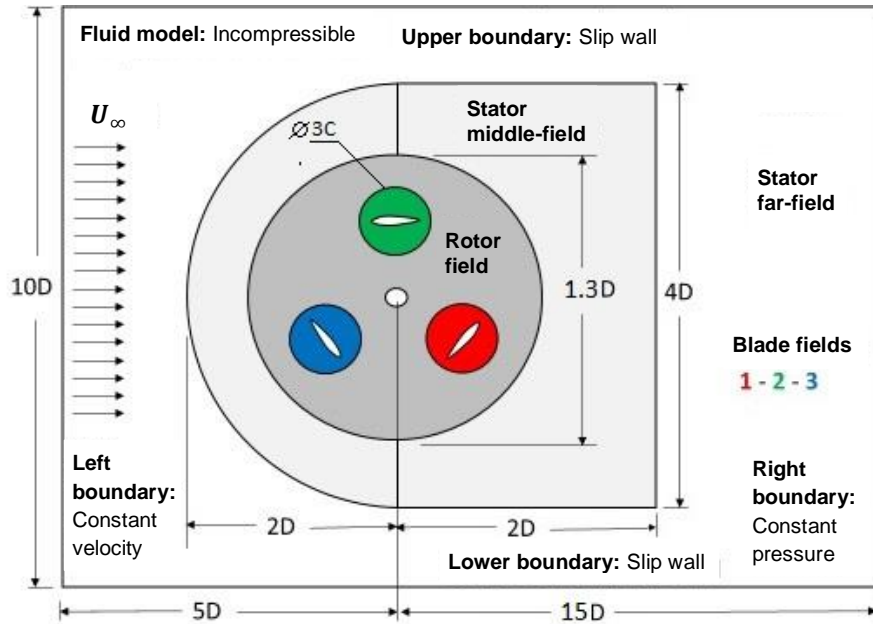


Figure 2.1. Computational domain for the VAWT (not to scale)

The stationary region of the mesh is termed the “stator field.” For computation efficiency, this region is divided into a far-field region with coarse unstructured elements and a middle-field region where the elements become structured and progressively finer near the VAWT region. The moving regions of the mesh are subdivided into the “blade fields” and the “rotor field.” The blade fields consist of the blade walls and the regions immediately surrounding the blades and are made up of a very high element-density mesh. During the CFD simulation, the blade-field meshes are subject to the superposition of the rotation of the blade around the center of the VAWT and the ABP of the blades about their axes. The rotor field consists of the intermediary region between the stator field and the blade field. This region consists of unstructured circular mesh that rotates about the axis of the VAWT; the mesh elements become progressively finer near the blade-fields region. Figure 2.2 shows the mesh regions. The relative diameter of the blade field is set to $3 \times C$; while Abdalrahman et al. [20] used a blade field diameter of $1.6 \times C$ for their ABP simulations, we chose to increase this dimension in order to improve the transition from the rotor field to the blade fields.

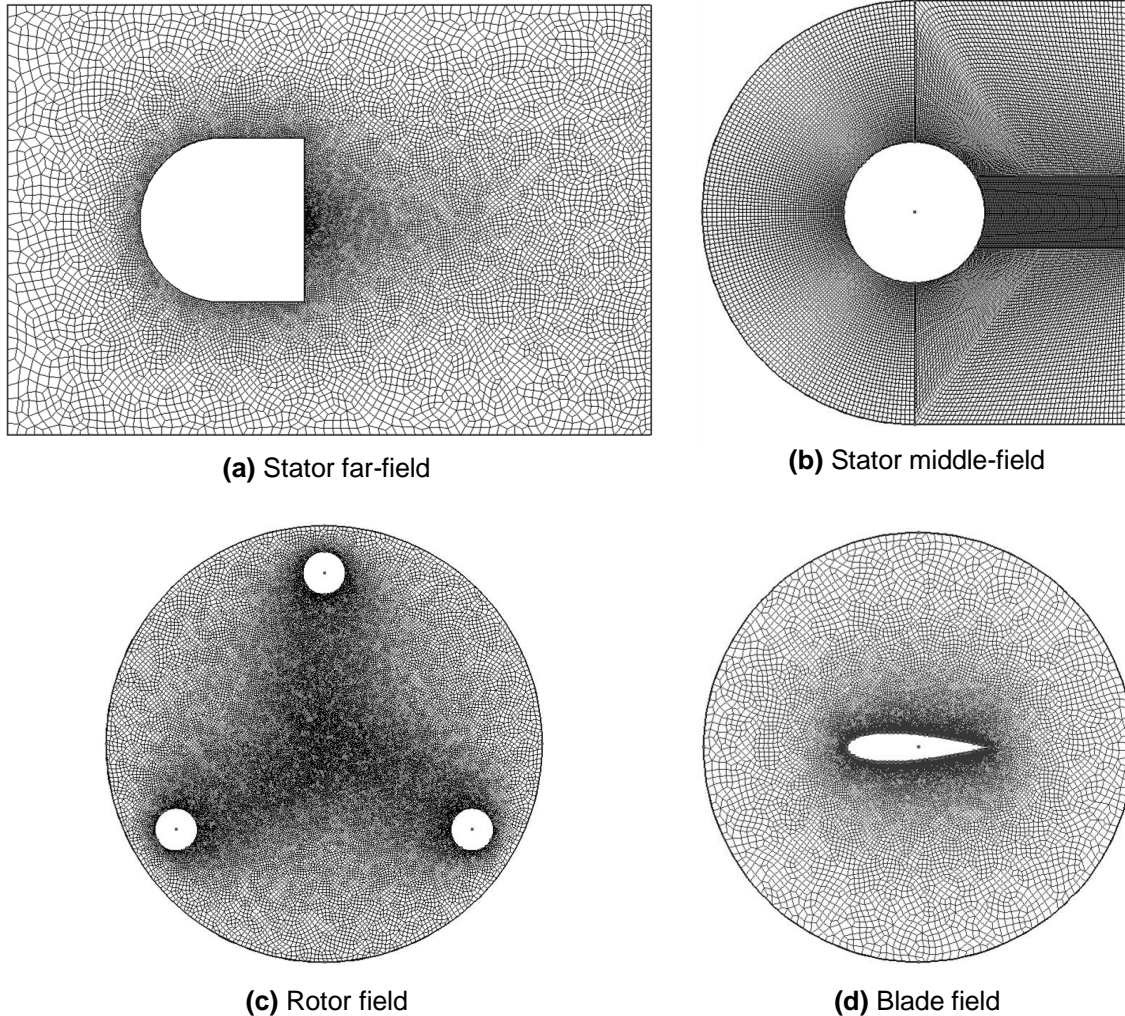


Figure 2.2. Mesh fields on the computational domain

This multi-region mesh was implemented in Gmsh (v 2.8.5). The software was chosen because the scripting language of Gmsh allowed parametric mesh generation. The following files are used in generating the mesh:

parameters.geo: specifies the values of the following parameters: chord length, VAWT diameter, height, number blades, blade profile; mesh density instructions; and so on. It also specifies the dimensions of the fluid field domains surrounding the VAWT, the stator field, the rotor field, and the blades field.

NACA4.geo: generates the blade profile and the circle envelope to fit into the rotor field into a mesh file called *NACA4.msh*. It also generates a highly structured boundary layer mesh surrounding the airfoil walls.

Rotor.geo: generates the rotor field (called Rotor.msh) and includes equally spaced areas for the blade fields and the circle envelope that fit into the stator field.

Stator.geo: generates the stator field (Stator.msh) which includes the far-field stator and the near-field stator; basically, the fluid fields away from the VAWT.

merge.awk: AWK script used to merge the individual mesh regions into a single mesh.

The final merged mesh is imported into OpenFOAM using the `gmshToFOAM` command. The code for these script files can be found in Appendix D.

2.2. Case Structure Setup

2.2.1. Computational Parameters

OpenFOAM (v3.0.1) was used to construct the CFD case as it is open source software, so no additional licenses were needed to run multiple simulations. The software is also available at a supercomputer facility located at Compute Canada.

The CFD simulations use a Reynolds-averaged Navier–Stokes (RANS) model with a $k-\omega$ SST turbulence model. The simulations assume air to be an incompressible fluid and use a transient `pimpleDyMFoam` solver with a second-order scheme. The $k-\omega$ SST turbulence model was chosen because it accurately captures the flow both near the walls and in the freestream [18] [31]. Further, the flow can be assumed to be incompressible due to the flow speeds being well below Mach one [18][31]. The fluid properties of the air used in the simulation are presented in Table 2.2.

Table 2.2. Air transport properties

Constant	Description	Value	Units
ρ	Density	1.205	kg/m ³
μ	Dynamic viscosity	1.9137E-5	kg/ms
ν	Kinematic viscosity	1.588E-5	m ² /s
T_{ref}	Temperature	300.0	K

Default air properties values in OpenFOAM3.0.1

The simulations used a variable time step constrained by a maximum Courant number (Co) of 8 at any given location in the mesh and any given time of the simulation. The Courant number can be interpreted as the local distance a fluid particle travels in a

given time step (i.e. local velocity \times time step) relative to the mesh size [32]. A Co of 8 offers a good balance between simulation speed and simulation stability (note that lowering the Co value also reduces the time step); a time-step independence study in Section 2.3 will show that the simulation reached stability for a Co of 8. The 2D model dimension follows the same VAWT physical characteristics presented in Table 1.1. In addition, Appendix A provides the OpenFOAM folder and file structure for this case.

2.2.2. Tabulated Movement for Rotating Fluid Domains

The pitching movements of the blade field meshes may not be expressible as a simple mathematical function (such as a sine or cosine). While it may be possible to use the harmonics of a Fourier series expansion, this approach is inaccurate, difficult to automate, and lacks flexibility (especially if a smooth acceleration ramp is needed at the beginning of the simulation). Hence the motion for the moving regions is read in a tabulated form in a text file by OpenFOAM. Figure 2.3 illustrates the structure of the tabulated data read by OpenFOAM.

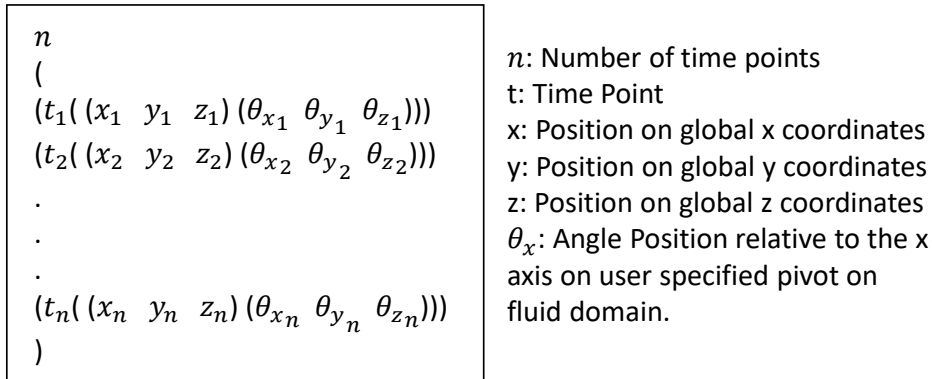
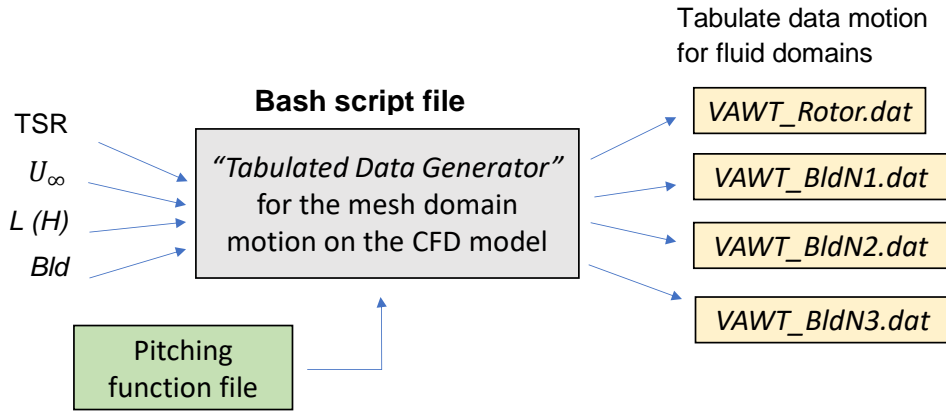


Figure 2.3. Tabulated data file structure

A script was written to automate the generation of this tabulated data. The script takes the ABP over one revolution, the TSR, the freestream wind velocity, and the radius of the VAWT as inputs, and writes out VAWT_Rotor.dat, VAWT_BldN1, VAWT_BldN2, and VAWT_BldN3.dat with explicit displacements and rotation data for Rotor, Blade 1, Blade 2, and Blade 3 respectively. Figure 2.4 illustrates a black-box diagram of the script file that generates the tabulated data, which can be reviewed in Appendix E.



VAWT_Rotor.dat file moves the rotor field and VAWT_BldN#.dat files move the blade fields.

Figure 2.4. Black-box diagram of the bash script for the tabulated data files

2.2.3. Acceleration Profile

It was desirable to provide a smooth acceleration at the beginning of the simulation, as shown in Figure 2.5. This profile was chosen to minimize vortices and high-velocity gradients due to sudden value changes in the velocity field. By reducing the initial transient phenomena, we speed up the transition to steady-state flow.

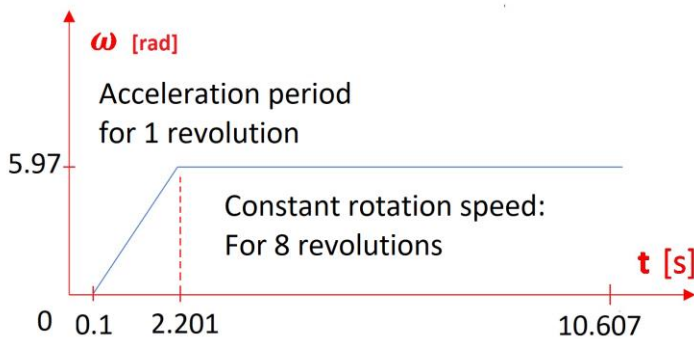


Figure 2.5. Motion profile within the tabulated data

2.3. CFD Validation for NACA0021 Airfoil

As mentioned earlier, we employ a 2D Reynolds-averaged Navier–Stokes equations (RANS) CFD simulation with a $k-\omega$ SST turbulence model. The simulations used a transient pimpleDyMFoam solver with a variable time step determined by the Courant number. A NACA0021 with a chord length of 0.57 m is used in this validation study. Figure 2.6 provides the domain dimensions used in the simulations, which were adapted from Rezaeiha et al. [18]. The freestream wind velocity is set to 10 m/s with standard air properties at 27° C at ground level resulting in a Reynolds number of 360,000. This Reynolds number was chosen as representing the average Reynolds number experienced by the VAWT blades. The mesh was chosen to ensure that the dimensionless thickness parameter of the first layer $y^+ \lesssim 8$, and the maximum Courant number was set to 1. Figure 2.7 shows snapshots of the mesh near the airfoil.

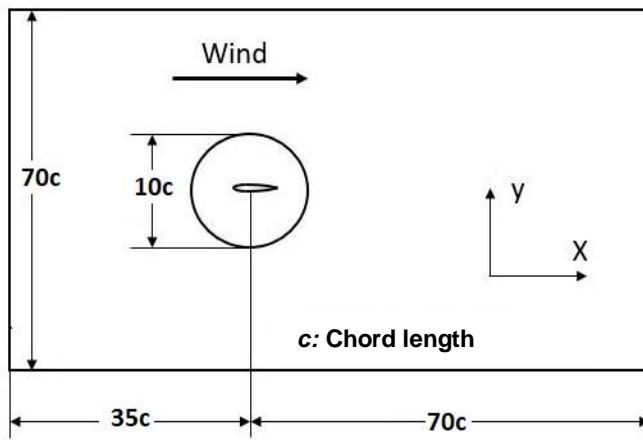


Figure 2.6. Domain dimensions for airfoil validations

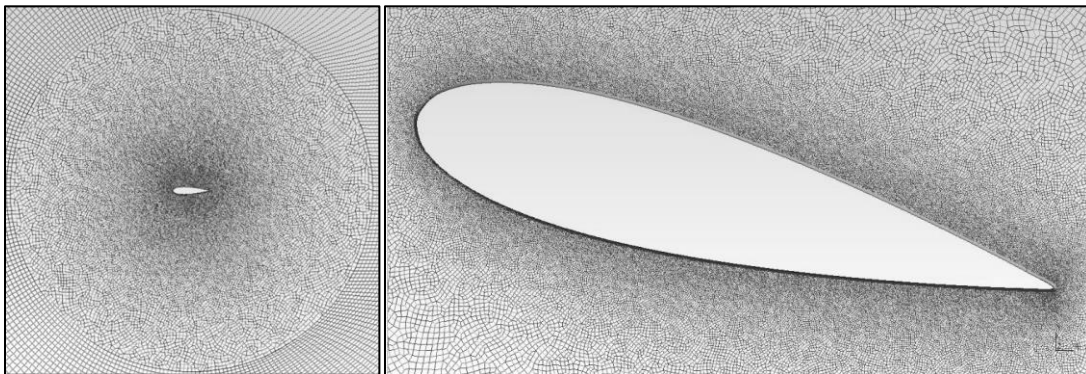


Figure 2.7. High-density mesh snapshots, cell count $\approx 274,000$

The lift and drag coefficients of a NACA0021 airfoil are attained via CFD simulations for angles of attack from 0° to 25° . The mesh independence study is done by proportionally increasing the number of elements over the whole domain. For simulations with fixed Courant numbers, increasing mesh density decreases the simulation time step, so that the simulation also becomes insensitive to lower time steps (time-step independence). The dimensionless parameter y^+ measures the thickness of the mesh cells at the wall boundaries relative to the boundary layer thickness; the value of y^+ is estimated by semi-empirical formulas derived from flat plate boundary layer theory. OpenFOAM computes the forces at the walls differently depending on the value of y^+ , and we expect the simulations to be sensitive to this parameter. For low y^+ values (close to 1 or lower), the cells slice the laminar interface of the boundary layer, while for $y^+ > 1$, the cell will be thicker than the laminar interfaces of the boundary layer and OpenFOAM will use a different algorithm to compute forces. Figure 2.8 shows two y^+ values subject to study.

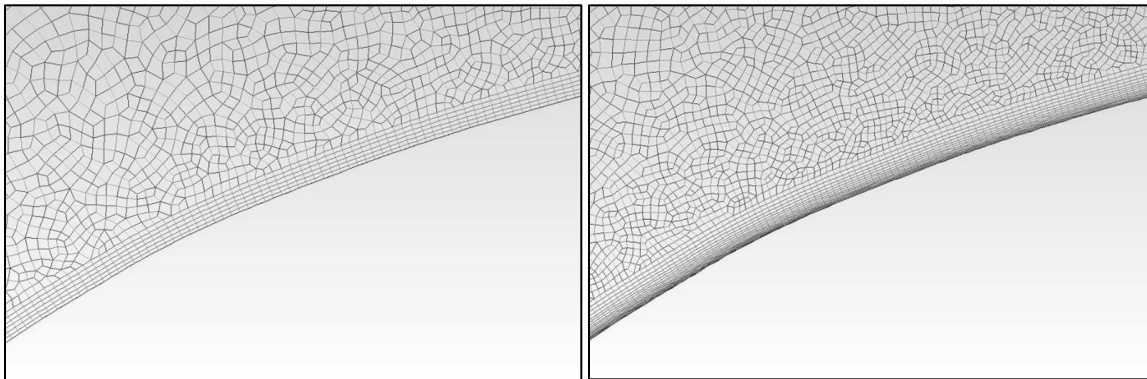


Figure 2.8. Boundary layer cells thickness: $y^+ = 8$ (left), $y^+ = 0.8$ (right)

Figure 2.9 shows the mesh independence study and Figure 2.10 compares the CFD results for a high mesh with experimental results for $y^+ = 0.8$. Similarly, Figure 2.11 presents a mesh independence study and Figure 2.12 a CFD versus experiment comparison for $y^+ = 8$.

For angles below the maximum lift, the CFD results for C_L are within 3% of the experimental values for $y^+ = 0.8$ and within 4% of the experimental values for $y^+ = 8$. As we approach and exceed the critical angle of attack (where aerodynamic stall occurs, 15° in this case), the error reaches a maximum of 18% at 22° for $y^+ = 0.8$ and of 8% at 20° for $y^+ = 8$. When examining the C_D values, we see that the CFD overpredicts the occurrence of aerodynamic stall and also overpredicts the drag coefficients by about

16%. While in the experiments, stall occurs abruptly at 15° (as apparent from the sudden increase in C_D), the CFD simulation exhibits a gradual transition between 15° and 20° . This may be attributed to smooth back vacuum bubble development, also seen and discussed in studies [17,33,34]. The parameter of $y^+ = 0.8$ will not be used for the succeeding VAWT simulations since it has a higher computational demand compared to $y^+ = 8$, the later having less error over a wide range of angles of attack.

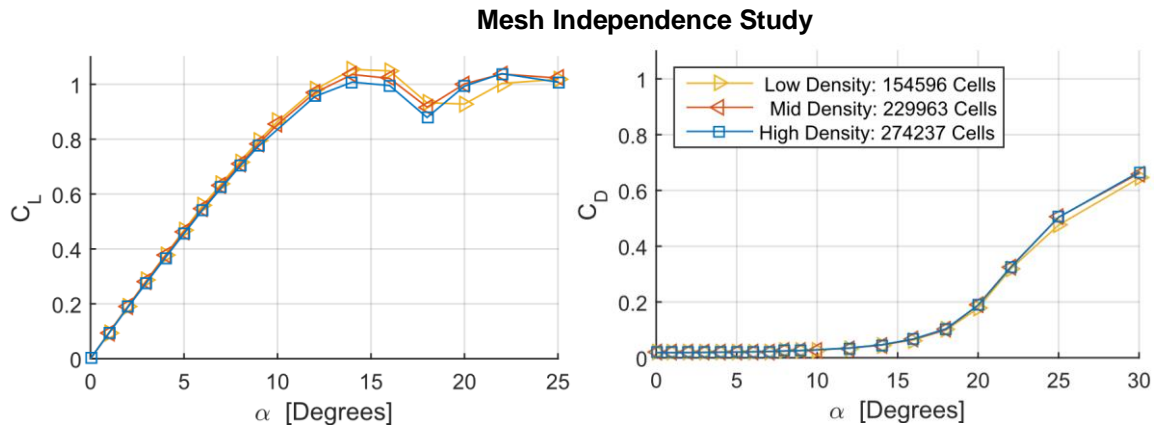


Figure 2.9. Mesh independence study, $Re = 360,000$, wall cells at $y^+ = 0.8$; lift coefficient (left) and drag coefficient (right)

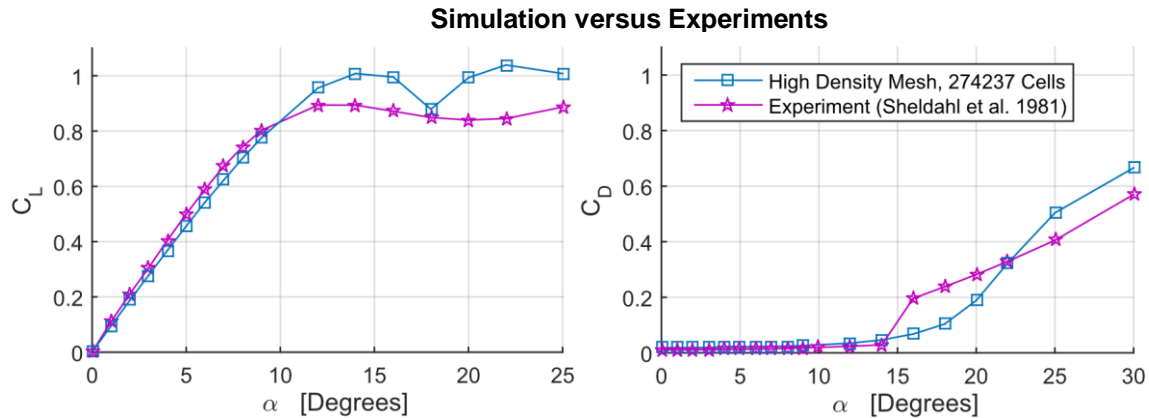


Figure 2.10. Simulation versus experiment comparison, $Re = 360,000$, wall cells at $y^+=0.8$; lift coefficient (left) and drag coefficient (right)

Mesh Independence Study

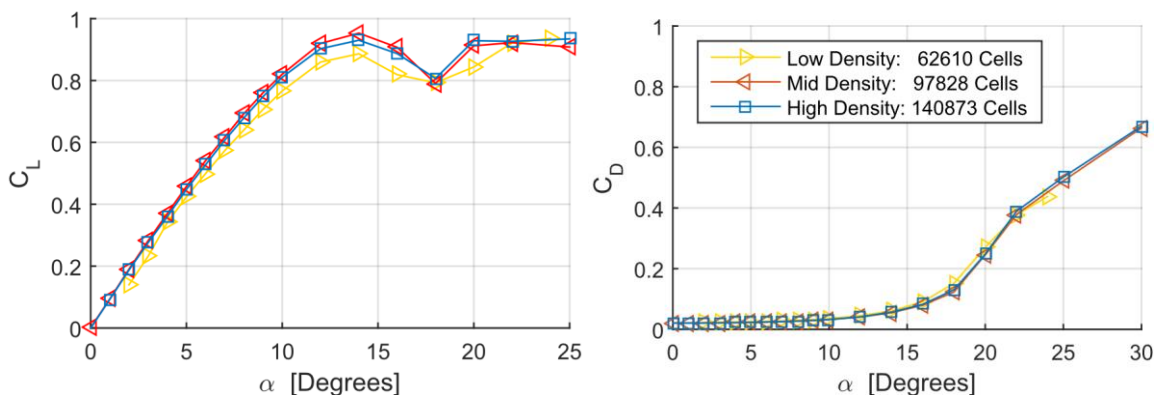


Figure 2.11. Mesh independence study, $Re = 360,000$, wall cells at $y^+ = 8$; lift coefficient (left) and drag coefficient (right)

Simulation versus Experiments

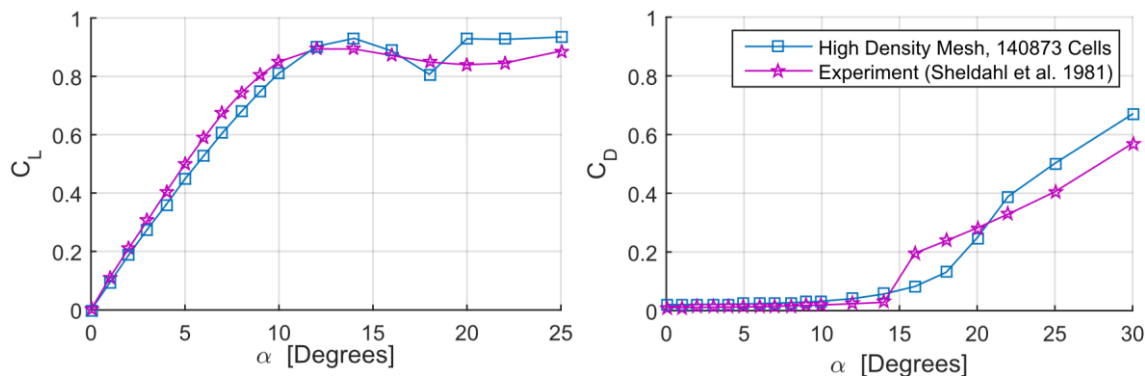


Figure 2.12. Simulation versus experiment comparison, $Re = 360,000$, wall cells at $y^+ = 8$; lift coefficient (left) and drag coefficient (right)

2.4. VAWT CFD 2D Simulation and Experimental Data

The mesh was constructed based on the discussion in Section 2.1 and the CFD simulations were set up as discussed in Section 2.2. The TSR was varied from 4.5 to 1.5 by varying the wind speed from 3.98 m/s to 11.9 m/s while keeping the rotation speed at 5.97 rad/s. This method of varying the TSR was chosen to match those adopted in the validation study in Kjellin et al. [30]. For a TSR range of 3.8 to 4.5, the torque results were found to reach steady state after 16 revolutions, while only 8 revolutions were needed for the TSR range of 1.5 to 3.3. The simulation time step is automatically selected by OpenFOAM to ensure a maximum Courant number (Co) of 8.

2.4.1. Mesh and Time-Step Independence

To test for mesh independence and time independence, simulations were run for three cases: i) mesh with 163,666 cells for $Co = 8$; ii) mesh with 117,356 cells for $Co = 8$; and iii) mesh with 117,356 cells for $Co = 4$ (at $TSR = 2.3, 2.8, 3.3, 3.8, 4.3, 4.5$). The VAWT average torque (T_{cfd}) is collected from the CFD simulations and the power coefficient C_p is computed using equations (2.1) and (2.2). Note that T_{cfd} corresponds to the sum of all three blades' average torques. Figure 2.13 presents the power performance curves and the results show a variation of less than 3% between the three cases, indicating both mesh and time independence.

$$C_T = \frac{T_{cfd}}{0.5\rho ArU_\infty^2} \quad (2.1)$$

$$C_p = C_T \times TSR \quad (2.2)$$

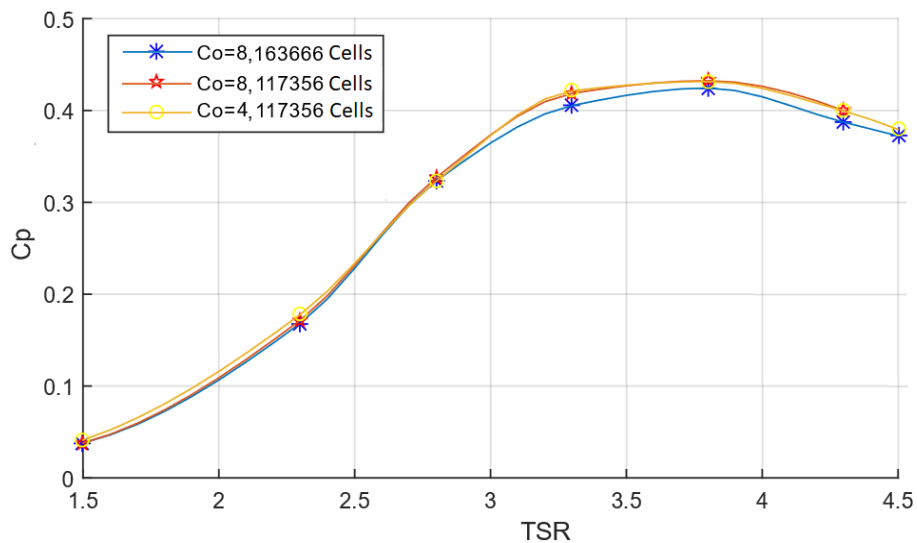


Figure 2.13. Simulation mesh and time-step independence study

Table 2.3 shows the data output for the group of simulations evaluated for a mesh with 163,666 cells and $Co = 8$.

Table 2.3. Simulation results, $y^+ = 8$, $Co = 8$, mesh of 163,666 cells

TSR	U_∞ [m/s]	ω [rad/s]	Revs	T_{cfd} [Nm]	C_T	C_P
4.5	3.98	5.97	16	71.056	0.0827	0.3723
4.3	4.16	5.97	16	84.505	0.0901	0.3872
3.8	4.71	5.97	16	134.39	0.1117	0.4244
3.3	5.42	5.97	8	195.95	0.1228	0.4053
2.8	6.39	5.97	8	255.55	0.1154	0.3232
2.3	7.78	5.97	8	240.18	0.0732	0.1683
1.5	11.9	5.97	8	179.03	0.0026	0.0380

2.4.2. CFD Validation Using Previously Published Experiments

We compare the CFD results for the mesh with 163,666 elements and $Co = 8$ with experimental results provided in Kjellin et al. [30]. Figure 2.14 shows the schematic of the H-Darrieus VAWT; the design choices are discussed in Solum et al. [35]. The VAWT has a height (H) of 5 m, a chord length (C) of 25 cm with a NACA0021 profile pitched at 2° outward, and a diameter (D) of 6 m (or radius $r = 3$ m), providing a cross-section swept area (A) of 30 m^2 . To reduce the tip vortex losses and drag, the ends of the blades are tapered to 60% of the chord length; the transition is uniform and starts 1 m away from the edge, as shown in Figure 2.15(a). Each blade is connected by two struts that have a NACA0025 profile that shortens at the end, with chord length 320 mm close to the hub and 200 mm at the end. The mounting angle of the struts is 17.6° as shown in Figure 2.15(b).

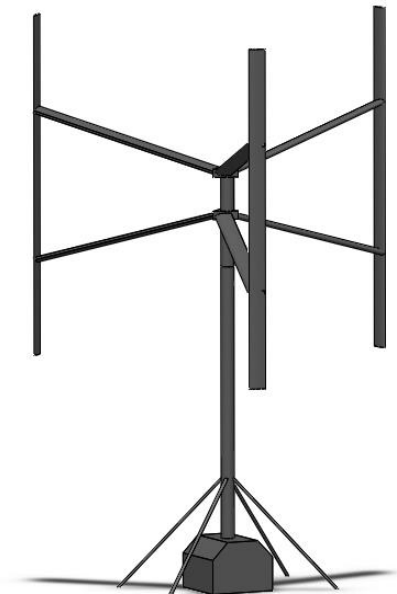


Figure 2.14. H-Darrieus rotor VAWT

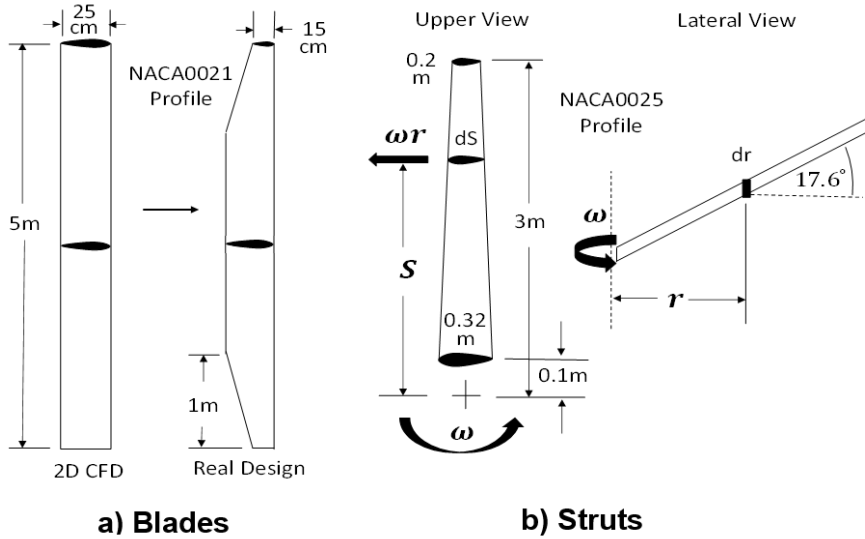


Figure 2.15. Real design considerations for a) blades and b) struts

The effective torque T_{eff} , which will be used to determine the C_p , is calculated from T_{cfd} as follows:

$$T_{eff} = \eta_{chord} \times \eta_{vortex} \times T_{cfd} - T_{Drag_{struts}} \quad (2.3)$$

where

η_{chord} is the compensation factor for the variation in the chord length,

η_{vortex} is the compensation factor to account for tip vortexes, and

$T_{Drag_{rod}}$ is the drag torque experienced by the struts.

Now for a given airfoil, as will be seen later in equation (3.17), the torque produced is proportional to the product of the chord length C and the blade length L (and also the VAWT height H). Consequently, the torque would scale with the chord length.

Using the data provided by Kjellin et al. [30], the chord length is given by

$$\frac{C}{C_{center}} = \begin{cases} 0.6 + 0.4 \times (1 - z) & 0 \leq z < 1 \\ 1 & 1 \leq z < 4 \\ 0.6 + 0.4 \times (5 - z) & 4 \leq z \leq 5 \end{cases} \quad (2.4)$$

This yields an average $C/C_{center} = 0.92$. Hence a multiplier 0.92 will be used to compensate for blade surface reduction.

$$\eta_{chord} = 0.92 \quad (2.5)$$

Solum et al. [35] have calculated the tip vortex losses analysis of the 12-kW VAWT using a modified Prandtl lifting-line theory [36] [37]. They reported that the maximum tip vortex losses resulted in a 16% reduction in the overall power output. Hence,

$$\eta_{vortex} = 1 - 0.16 = 0.84 \quad (2.6)$$

Solum et al. [35] do not provide sufficient explanation of the struts drag. We therefore use a BET model to determine the drag torque (Appendix B provide further description of this procedure). Using (3.11) on an elemental area, the elemental torque is given by

$$dT_{Drag_{1-rod}} = 1/2 \rho (\omega r)^2 C_{d-strut} r \times dA \quad (2.7)$$

Owing to the configuration of the struts,

$$C_{strut} = 324.14 - 41.4r \quad (2.8)$$

$$dA = C_{strut} \frac{dr}{\cos(17.6^\circ)} \quad (2.9)$$

$$Re = \frac{\rho(\omega r)C_{strut}}{\mu} \quad (2.10)$$

Hence the drag torque for a single rod is given by

$$T_{Drag_{1-rod}} = \frac{\rho \omega^2}{2 \cos(17.6^\circ)} \int_{r=0.1}^{r=3} r^3 C_d C \times dr \quad (2.11)$$

The drag coefficients are taken from static drag tables for NACA0025 [38], and by substituting $\omega = 5.97$ rad/s we find the drag of a single strut rod to be 1.5 Nm. Hence, the total drag torque for all six struts is given by

$$T_{Drag_{struts}} = 6 \times T_{Drag_{1-rod}} = 6 \times 1.5 \text{ Nm} = 9 \text{ Nm} \quad (2.12)$$

The effective power coefficient C_p for the CFD simulation (obtained by using T_{eff}) is compared with the experimental work of Kjellin et al [30]. The experiment used the averaging method of bins recommended by International Standard IEC 61400-12-1, the measured data is used to create a curve with an error band, shown in Figure 2.16. As discussed before, the experimental measurements and the simulation data were taken by letting the VAWT rotate at fixed speed while measuring the freestream wind speed, and the C_p is computed following that strategy. The CFD power coefficient curve agrees well with experimental results up to the point of maximum power.

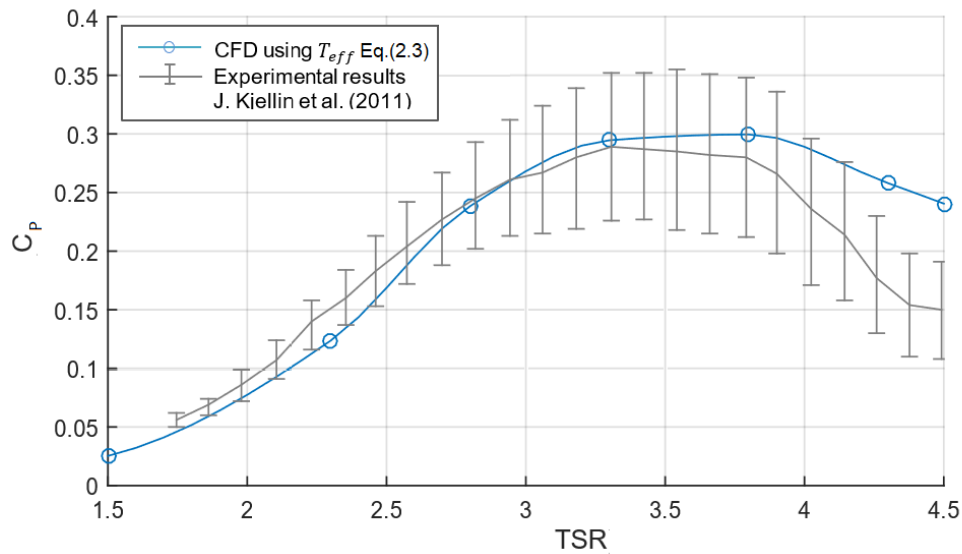


Figure 2.16. Comparison of experimental and CFD results

The deviations at higher TSR (3.8 in Figure 2.16) can be attributed to phenomena not captured by the current analysis: The interaction of the center shaft and struts with the flow pattern in the downwind section of the VAWT, which affects the torque produced by the blades during the backswept phase, and the incoming flow interaction with the struts, which affects the total struts drag. In earlier studies the authors also attribute differences among the results of 2D simulations, 3D simulations, and experiments to tip vortex losses and center shaft and struts drag [17] and [19]. It should be noted that these explanations were not verified numerically. For the purpose of this work, the current analysis provides a non-exhaustive numerical approach to compensate for 3D effects in 2D simulation data. Finally, the compensated CFD results maintain the experiment tendencies within a narrow range over a wide range of TSRs.

Figure 2.17 and Figure 2.18 show the normalized velocity and pressure fields respectively corresponding to a TSR of 3.3.

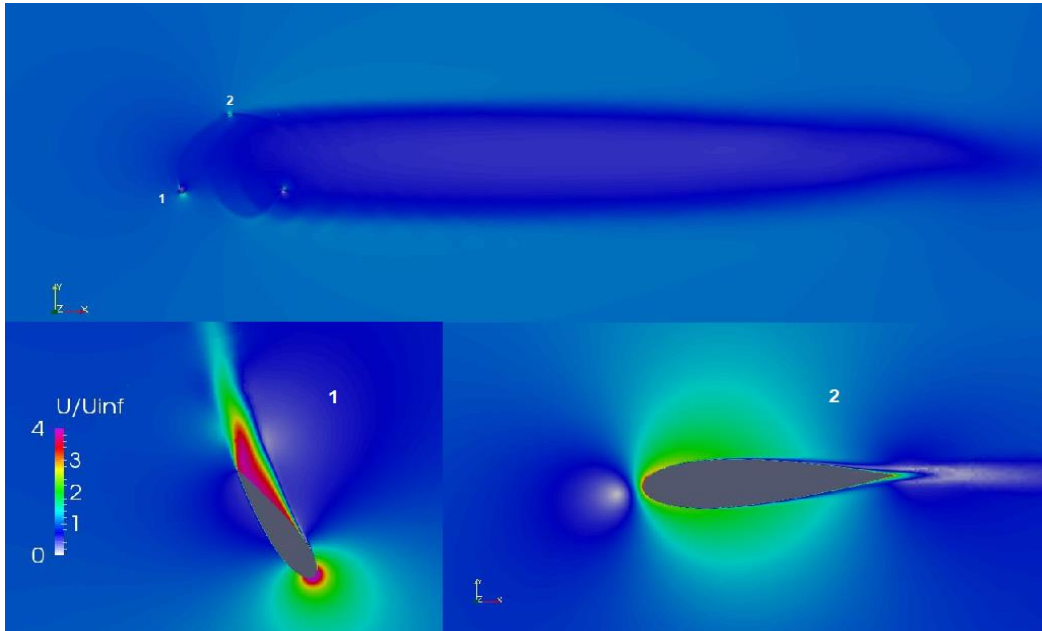


Figure 2.17. Normalized velocity field with fixed 2° pitch, TSR = 3.3, $\theta = 0^\circ$, time $t = 10.9$ s

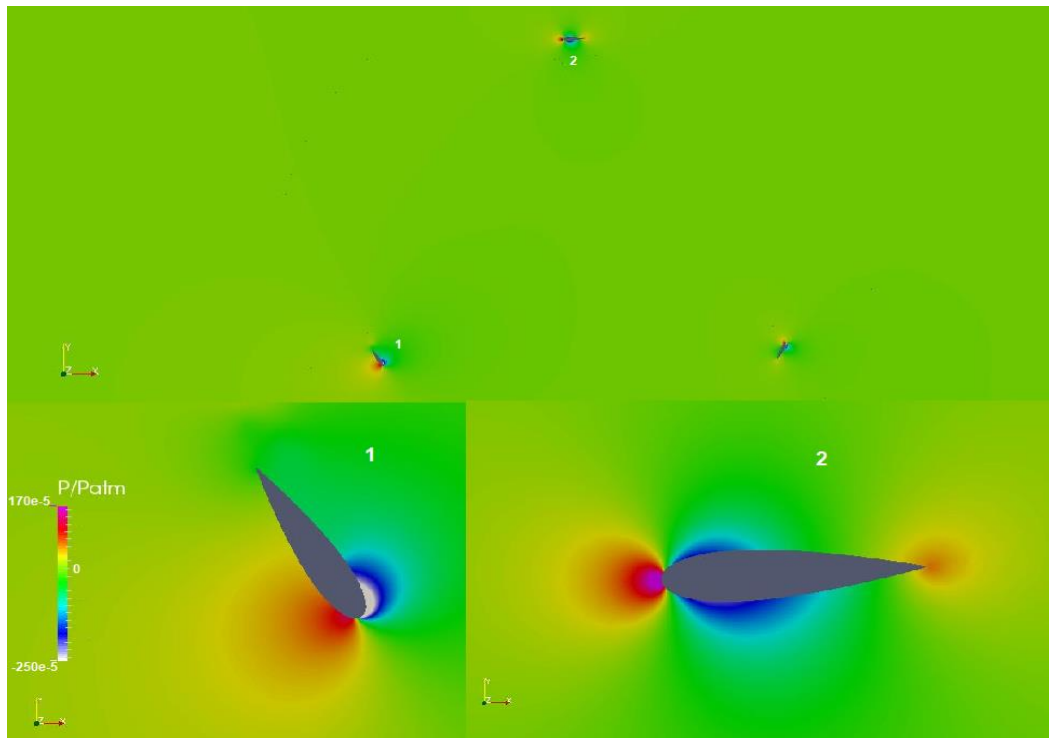


Figure 2.18. Normalized pressure field with fixed 2° pitch, TSR = 3.3, $\theta = 0^\circ$, time $t = 10.9$ s

This chapter has described in detail the simulation setup, and the CFD case was compared with experimental data, showing a remarkable correlation. Based on those results, the simulations can be expected to be accurate enough to predict VAWT performance under ABP. We assume that the performance changes in the VAWT simulations under ABP will produce a similar trend in the physical design. The groundwork of this thesis is now established, and the ABP models for VAWT are ready for simulation.

The next chapters will describe and develop ABP models, which will control the mesh motion on the simulations (as explained in Section 2.2). The simulations will be used to generate results such as the torque profile and average torque produced by a VAWT blade. Finally, the torque results allow us to compare and assess the performance of several ABP strategies.

Chapter 3.

Preliminary Active Blade Pitching for VAWT

This chapter provides a theoretical analysis of VAWTs using Glauert's blade element theory [4]. The analytical model allows a preliminary ABP to be computed. This model does not capture complex secondary fluid dynamics, yet the control function derived from this model shares many characteristics (as well as its general shape) with the control functions derived from other more complex models.

3.1. Blade Element Model Development

Consider the system shown in Figure 3.1 representing a preliminary kinematic diagram for a VAWT blade. The airfoil is rotating at an angular velocity $\vec{\omega}$ at a position \vec{r} from the rotation center, and it interacts with the freestream wind velocity \vec{U}_∞ . Here, θ denotes for the azimuthal angle (relative to the x coordinates), α_0 denotes for the angle of attack at zero pitch, and ϕ is the angle of the effective wind velocity experienced by the blade \vec{U}_{exp} (relative to the x coordinates).

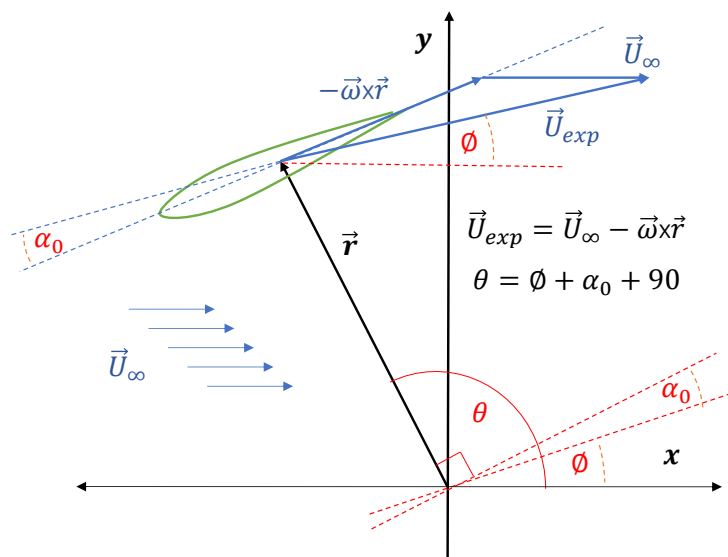


Figure 3.1. VAWT kinematics diagram, for any azimuthal angle

The effective wind velocity \vec{U}_{exp} can be written as a function of \vec{U}_∞ , $\vec{\omega}$, and \vec{r} as

$$\vec{U}_{exp} = \vec{U}_{\infty} - \vec{\omega} \times \vec{r} \quad (3.1)$$

Note that the TSR is defined as

$$\text{TSR} = \frac{\omega r}{U_{\infty}} \quad (3.2)$$

By resolving \vec{U}_{exp} we find that

$$U_{exp_x} = U_{\infty}(1 + \text{TSR} \sin \theta) \quad (3.3)$$

$$U_{exp_y} = -U_{\infty} \text{TSR} \cos \theta \quad (3.4)$$

The magnitude, U_{exp} , and the angle, ϕ , of \vec{U}_{exp} are given by

$$\phi = \angle \vec{U}_{exp} = \arctan \left(\frac{-\text{TSR} \cos \theta}{1 + \text{TSR} \sin \theta} \right) \quad (3.5)$$

$$U_{exp} = |\vec{U}_{exp}| = \sqrt{U_{exp_x}^2 + U_{exp_y}^2} = U_{\infty} \sqrt{1 + 2\text{TSR} \sin \theta + \text{TSR}^2} \quad (3.6)$$

In the absence of blade pitching, the chord line of the blade is oriented along the tangential direction (as seen in Figure 3.1). This angle of attack at zero pitch, α_0 , can be given by

$$\alpha_0 = \theta - \phi - 90^\circ \quad (3.7)$$

Taking (3.5) into (3.7) and resolving α_0 with trigonometric identities,

$$\alpha_0 = \arctan \left(\frac{-\cos \theta}{\sin \theta + \text{TSR}} \right) \quad (3.8)$$

Next, when the blade is pitched by an angle θ_p relative to the tangential direction, the angle of attack α is given by

$$\alpha = \alpha_0 + \theta_p \quad (3.9)$$

The lift and the drag force can be calculated as

$$F_L(a, Re_L) = \frac{1}{2} \rho U_{exp}^2 A_{Blid} \times C_L(a, Re_L) \quad (3.10)$$

$$F_D(a, Re_L) = \frac{1}{2} \rho U_{exp}^2 A_{Blid} \times C_D(a, Re_L) \quad (3.11)$$

where $C_L(\alpha, Re_L)$ and $C_D(\alpha, Re_L)$ denote the local lift and drag coefficients respectively and can be obtained from experimental data found in literature, while A_{Blid} denotes for the reference area of the blade (chord length C times VAWT height H). The local Reynolds number Re_L is given by

$$Re_L = \frac{\rho |\vec{U}_{exp}| C}{\mu} \quad (3.12)$$

Since the lift force F_L is perpendicular to and the drag force F_D is along the wind direction, we will define a new coordinate system with x' oriented along \vec{U}_{exp} , shown in Figure 3.2 and Figure 3.3. Notice that x' is rotated at by $-\phi$ relative to the original x -axis. The coordinates of the center of the blade located at \vec{r}_1 can be given as

$$r_{1x} = (r \cos \theta) \cos \phi + (r \sin \theta) \sin \phi \quad (3.13)$$

$$r_{1y} = -(r \cos \theta) \sin \phi + (r \sin \theta) \cos \phi \quad (3.14)$$

For a symmetric and subsonic airfoil such as the NACA0021, the pressure center of the lift and drag forces are approximately a quarter ahead of the chord center for most angles of attack [39]. The components of the force center located at \vec{r}_2 can be given as

$$r_{2x} = r_{1x} + (C/4) \cos(180^\circ + a) \quad (3.15)$$

$$r_{2y} = r_{1y} + (C/4) \sin(180^\circ + a) \quad (3.16)$$

The total torque for a blade can be written as

$$T_{Blid} = F_L \cdot r_{2x} - F_D \cdot r_{2y} = \frac{1}{2} \rho U_{exp}^2 A_{Blid} \times (C_L \cdot r_{2x} - C_D \cdot r_{2y}) \quad (3.17)$$

From a cursory analysis of equation (3.8), two cases emerge for the frame rotation described earlier. For $90^\circ < \theta < 270^\circ$, corresponding to the upwind area of the VAWT, $\alpha_0 > 0$. Hence, $\theta - \phi > 90^\circ$ from equation (3.7) and this case is depicted in Figure 3.2. For $0^\circ < \theta < 90^\circ$ or $270^\circ < \theta < 360^\circ$, corresponding to the downwind area of the VAWT, $\alpha_0 < 0$. Therefore, from equation (3.7) $\theta - \phi < 90^\circ$, as shown in Figure 3.3.

We can see from Figure 3.2 (front swept force diagram) that for the VAWT to generate positive torque the lift force needs to be directed downwards and from Figure

3.2 (back swept force diagram) that the lift need to be directed upwards. As a result, if the fixed pitch angle is to be optimized for the upwind swept phase it would be detrimental for the downwind section, while a fixed pitch optimized for the downwind swept phase will be suboptimal for the upwind section. Therefore, in order to get maximum performance in both sections, ABP is necessary.

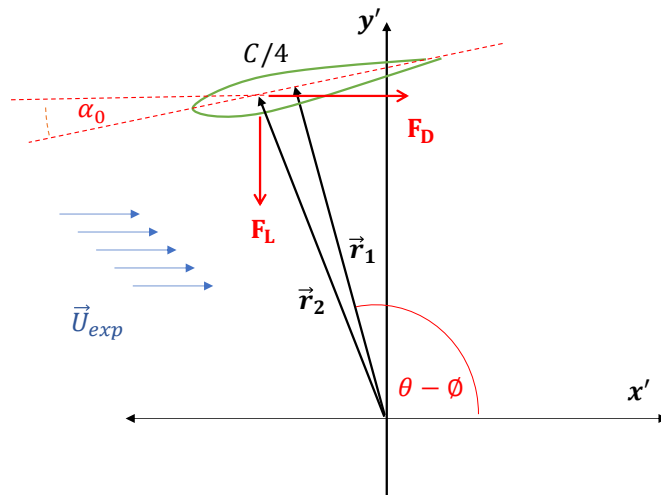


Figure 3.2. VAWT force diagram for upwind sweep ($90^\circ < \theta < 270^\circ$)

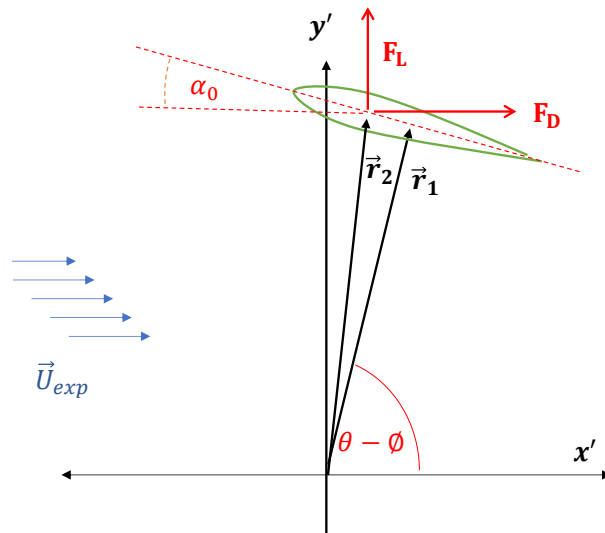


Figure 3.3. VAWT force diagram for downwind sweep ($\theta < 90^\circ$ or $\theta > 270^\circ$)

3.2. Blade Element Model Implementation

To obtain an ABP function, we first need to find the optimal attack angle α_{opt} of a blade; this is done by an exhaustive search of equation (3.17) and the optimization can be framed as determining α to maximize the torque at a fixed θ and TSR.

$$T_{Blid_{max}} = \max_{\alpha} T_{Blid} = \max_{\alpha} \left[\frac{1}{2} \rho U_{exp}^2 A_{Blid} \times (C_L \cdot r_{2x} - C_D \cdot r_{2y}) \right] \quad (3.18)$$

$$\alpha_{opt}(\theta) = \operatorname{argmax}_{\alpha} T_{Blid} \quad (3.19)$$

Once the optimal angle of attack, α_{opt} , is computed, the optimal pitch angle $\theta_{p_{opt}}$ is given by

$$\theta_{p_{opt}} = \alpha_{opt} - \alpha_0 \quad (3.20)$$

As discussed earlier, the lift and drag coefficients C_L, C_D , the components of \vec{r}_2 , and the magnitude of \vec{U}_{exp} are all dependent on the angle of attack α , local Reynolds Re_L , chord length C , azimuthal angle θ , and TSR. Further, the existing literature [38] provides tabulated data for C_L and C_D mapped with α and Re_L . We therefore implemented the following algorithm (Appendix C) in MATLAB to compute $\theta_{p_{opt}}$, α_{opt} , and α_0 as functions of θ :

- Obtain the inputs U_{∞} , TSR, and θ
- Compute ϕ and U_{exp} from (3.5) and (3.6) and determine Re_L using (3.12)
- Perform an exhaustive search over α to maximize T and report the maximum torque T_{max} at the corresponding α
 - For each α interpolate the available data to obtain C_L and C_D at the Re_L
 - Determine r_{2x} from (3.15) and r_{2y} from (3.16)
 - Solve (3.18) to determine T
 - Repeat the above substeps to search for α to maximize T .
 - Report the maximum torque T_{max} and the corresponding $\alpha = \alpha_{opt}$
- Calculate $\theta_{p_{opt}}$ from equation (3.20)
- Repeat the procedure for different θ

3.3. Analytically Derived ABP for TSR 2.3

Figure 3.4 shows the α_0 and α_{opt} at TSR = 2.3 as a function of the azimuthal angle. This TSR is selected as the study case due to the ABP having better effectiveness at lower TSR ranges as suggested in previous literature [1].

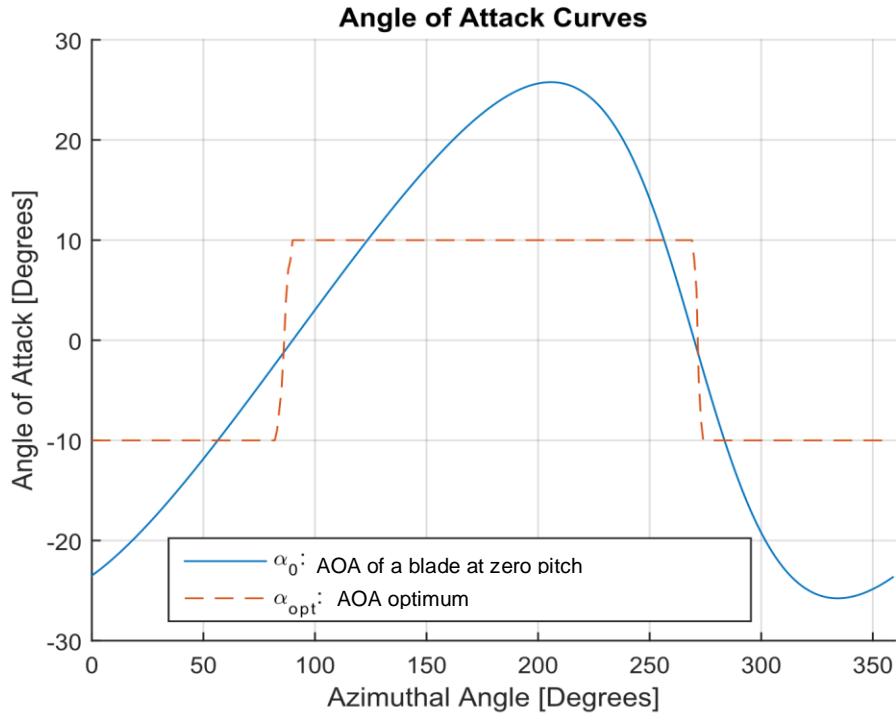


Figure 3.4. Angle of Attack functions, TSR = 2.3

Examining equation (3.8), we notice that α_0 is cyclic and decreases with increasing TSR, with $\alpha_0 = \theta - 90^\circ$ when $TSR = 0$ and $\alpha_0 = 0^\circ$ as $TSR \rightarrow \infty$. At 90° and 270° , $\alpha_0 = 0$ because \vec{U}_∞ becomes collinear with the blade rotational speed $\vec{\omega} \times \vec{r}$, while at 220° and 320° α_0 is maximum. Now, the maximum lift-to-drag ratio occurs close to the angle of attack of $\pm 10^\circ$. As a result, during the front swept phase of the blade ($90^\circ < \theta < 270^\circ$) the optimal angle of attack, $\alpha_{opt} \approx 10^\circ$, and during the back swept phase ($\theta < 90^\circ$ and $\theta > 270^\circ$), $\alpha_{opt} \approx -10^\circ$, with relatively sharp transitions at $\theta \approx 90^\circ$ and $\theta \approx 270^\circ$. This is an indication that the optimal angle of attack in the upwind sweep is opposite to the downwind sweep, consistent with the force diagrams of Figure 3.2 and Figure 3.3.

The optimum pitch angle, $\theta_{p_{opt}}$, is computed using equation (3.20) and the result is shown in Figure 3.5. Note that $\theta_{p_{opt}}$ is α_{opt} subtracted by α_0 ; therefore $\theta_{p_{opt}} \approx 10^\circ - \alpha_0$ for $90^\circ < \theta < 270^\circ$, and $\theta_{p_{opt}} \approx -10^\circ - \alpha_0$ for $\theta < 90^\circ$ and $\theta > 270^\circ$.

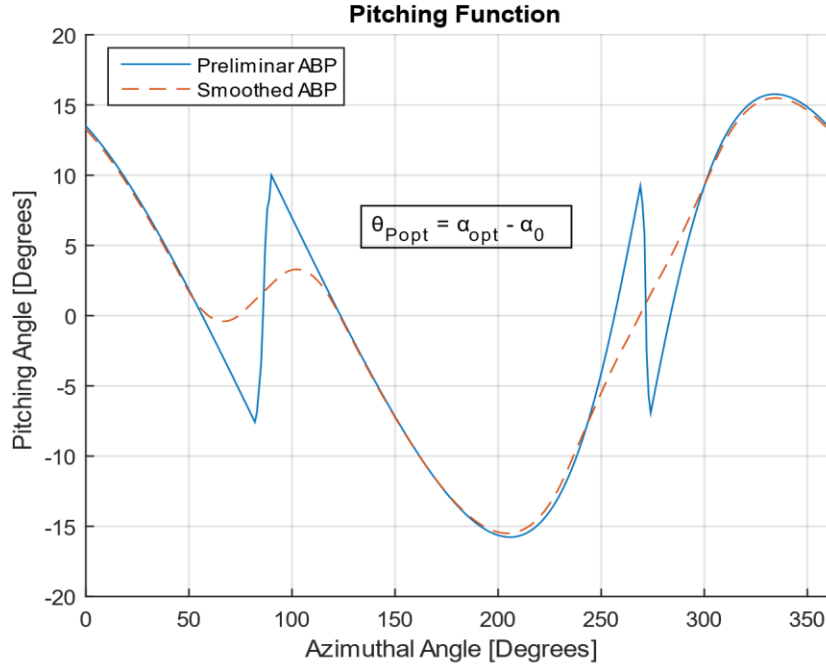


Figure 3.5. Analytic-ABP control function, TSR = 2.3

The sharp transitions seen at 90° and 270° in Figure 3.5 are a direct consequence of the abrupt change observed in α_{opt} , where the blades make the transitions from the upwind to the downwind area and vice versa. These sharp variations are undesirable and preliminary simulations showed vortex effects and high inertia forces on the blades; these effects were reduced by smoothing the analytic-ABP curve, the smoothing consisting of two rounds of a 28-point centered moving average. The smoothing filter was heuristically chosen to attain desired functionality and curve resemblance to the original non-smoothed analytic-ABP. The smoothed analytic-ABP is the one used for comparison against other ABP strategies for the rest of this work.

The analytic-ABP function of Figure 3.5 shares similar features with the ABP functions of earlier studies obtained with the DMSM [1], [3], and [10]. The sharp $\theta_{p_{opt}}$ variations at 90° and 270° are also present in the control functions of the cited studies.

3.4. Comparison of Analytic-ABP Versus Fixed-Pitch

Simulations for the 12-kW VAWT 2D model described in Chapter 2 is simulated for a fixed 2° corresponding to the physical VAWT in the literature [30], and for the analytic-ABP shown in Figure 3.5. for $TSR = 2.3$. The simulations were done with a wind speed U_∞ of 7.78 m/s and a TSR of 2.3. For both cases, the torque profile produced by a blade along a revolution is plotted in Figure 3.6. We see that the ABP has a greater positive area and therefore a higher average torque. The peak torque is lower for the ABP, perhaps due to secondary effects that reduce the lift; the ABP may generate vortex disturbances that impede producing more lift and torque, and the ABP may not be optimal at some ranges. Overall, the average blade torque using ABP is superior to the fixed blade strategy by 33.4%; also, the torque profile becomes more stable which is important for generating a steadier torque output.

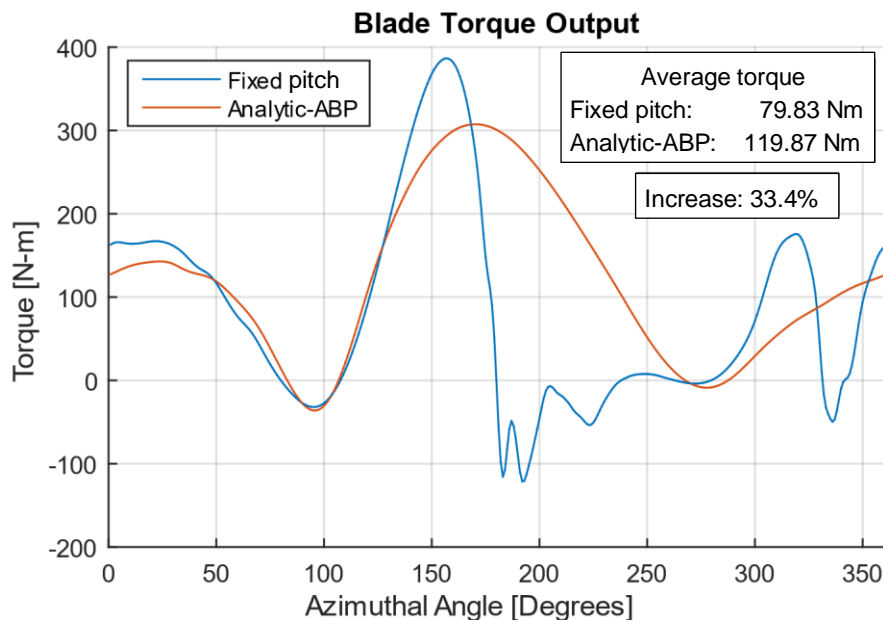


Figure 3.6. Torque output of a VAWT blade, fixed pitch at 2° and analytic-ABP, $U_\infty = 7.78$, $TSR = 2.3$

This chapter has described how an analytic model can be developed to obtain the ABP for a VAWT. The model derived a torque expression from a vector-kinematics analysis of the freestream wind speed and the blade rotation; the analysis assumed that no other secondary physical effects take place. The torque expression served to obtain an optimal angle of attack for a defined TSR and azimuthal angle, and the optimum pitch is then computed. The model served to understand the effective wind flow through the

blades and to derive a preliminary analytic-ABP for any TSR operating conditions over a whole revolution. The analytic-ABP results showed a performance increase compared to a fixed-pitch strategy.

The analytic-ABP function from this chapter will be used as a starting point for the optimization procedures described in the following chapters. We assume that this analytic model generates an ABP function close to an optimal ABP function, which will speed up convergence. Note that this model has no feedback from the CFD simulations (it is a one-way approach), and therefore we expect more room for improvement and that the feedback procedures presented in the next two chapters will generate better results.

Chapter 4.

Optimization of Parameterized Active Blade Pitching Function

In the previous chapter an ABP was computed based on an analytical model that was useful in improving the torque output of the VAWT blades; yet room for improvement remains, mainly because the model does not consider complex fluid dynamic effects. Consequently, a black-box optimization approach must be considered in order to improve the ABP function further.

4.1. Black-Box Optimization Overview

In this work, we use a CFD simulation which is a black-box function for the VAWT system. The system output response will be the torque produced by the blades and it will be dependent on the input stimulus, namely the pitching motion of the blades. If the input stimulus is periodic, the output will converge to a periodic response as well; therefore, we narrow the analysis to steady-state periodic behavior and discard any transient response, as shown in Figure 4.1.

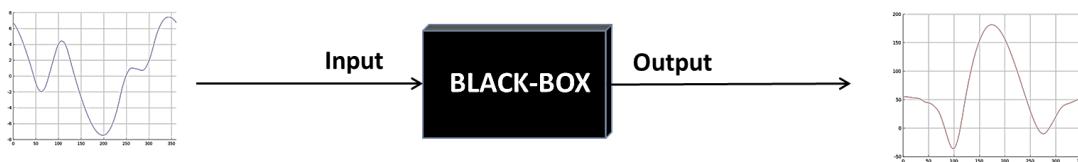


Figure 4.1. CFD simulation as the black-box with periodic pitching of blades as input and periodic instantaneous torque output

The optimization procedure requires variables as inputs and outputs, so we need to define the input ABP as an expression dependent on parameters (this is referred to as the parameterization of the input function). The parameter set becomes the input variable X , and for the output variable Y we take the average value of the instantaneous torque function (see Figure 4.2).

The next section describes the parameterization of the input function, which will be constructed to resemble the analytic-ABP of Chapter 3.

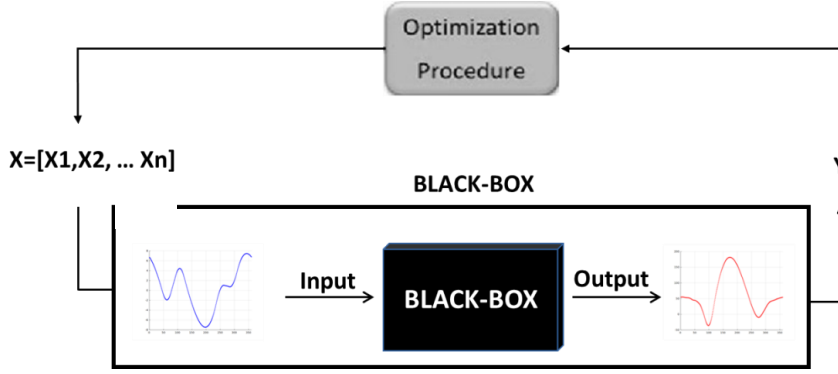


Figure 4.2. Block diagram schematic for a black-box optimization with parameterization of input stimulus and output response

4.2. Parameterization of the Input Stimulus

To parameterize the input ABP function, we chose the amplitude “ a ” and skewness “ b ” as parameters of equation (4.1), with the variables θ and P representing the azimuthal angle and pitching respectively. The periodic function in equation (4.1) is defined over a single blade cycle, $\theta \in [0, 2\pi]$ and was heuristically developed to closely reproduce the ABP using only two variables. The parameters (a, b) were found to be the most significant features of the analytic-ABP and the ABP of previous studies [1], [3] and [10]. The effects of the amplitude a and skewness b in the ABP function defined by equation (4.1) are shown in Figure 4.3. The input variable of the black-box X then becomes a two-dimensional vector $X = [a, b]$.

$$P(\theta) \begin{cases} a \sin \left(\tan^{-1} \left(b \left(\theta + \frac{\pi}{2} \right) \right) + \tan^{-1}(b\pi) \left(1 - \left(\theta + \frac{3\pi}{2} \right) / \pi \right) + \left(\theta + \frac{3\pi}{2} \right) \right), & \theta \in \left[0, \frac{\pi}{2} \right] \\ a \sin \left(\tan^{-1} \left(b \left(\theta - \frac{3\pi}{2} \right) \right) + \tan^{-1}(b\pi) \left(1 - \left(\theta - \frac{\pi}{2} \right) / \pi \right) + \left(\theta - \frac{\pi}{2} \right) \right), & \theta \in \left[\frac{\pi}{2}, 2\pi \right] \end{cases} \quad (4.1)$$

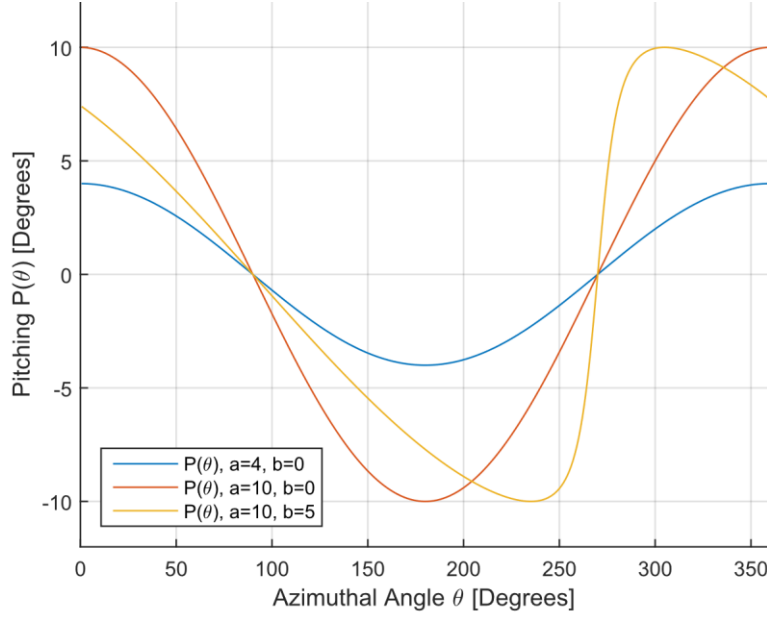


Figure 4.3. Effects of amplitude a and skewness b in equation (4.1)

4.3. Response Surface Methodology Description

The objective of this RSM is to provide a metamodel to search for and find an optimum. Therefore, it is desirable that the peak response (optimum) of the metamodel is within the design space [24]. The procedure begins by evaluating the black-box using a three-level full factorial design (FFD) strategy. Since three points define a quadratic function, three is the minimum number of levels required to quantify a curvilinear behavior. For a system of two design variables (referred to as factors in DOE), nine function evaluations are required ($9 = 3^2$) [21]. There is no need to choose the set center arbitrarily if some information regarding the system behavior is already known. As described initially, the center point should be near to the peak response (optimum). For this case, the optimal input was estimated analytically in Chapter 3, but equation (4.1) can approximate that input with the proper selection of parameters (a , b). Since the parameters a and b are the design variables of our RSM, we define the design space as $a \in [a_{min}, a_{max}]$ and $b \in [b_{min}, b_{max}]$. Following the three-level FFD DOE, the black-box function would be evaluated at

$$(a, b) = \left\{ a_{min}, \frac{(a_{min} + a_{max})}{2}, a_{max} \right\} \times \left\{ b_{min}, \frac{b_{min} + b_{max}}{2}, b_{max} \right\} \quad (4.2)$$

The nine CFD simulations corresponding to each design point (a, b) are evaluated in parallel, and a second-order polynomial metamodel is generated using a quadratic regression. The base function is

$$Y(a, b) = C_0 + C_1a + C_2b + C_3a^2 + C_4b^2 + C_5ab \quad (4.3)$$

where $C_i, i = 1,2,3,4,5$ are the regression coefficients. The formulation of the optimization problem is then as follows:

$$\text{Maximize } Y(a, b) \quad (4.4)$$

subject to:

$$a_{min} \leq a \leq a_{max}$$

$$b_{min} \leq b \leq b_{max}$$

If the optimal point of the metamodel is outside the design space, the FFD data set should be moved toward the optimal point indicated by the metamodel. If the solution is inside the design space, then we add the new point to the data set, fit a new quadratic regression, and find a new optimum. The procedure is repeated until the convergence condition is met. For our procedure, we will repeat the iterative process until the metamodel optimum output converges to within 5% of the previous iteration. The schematic for this procedure is shown in Figure 4.4. More details on metamodeling techniques and design of experiments (DOE) methods can be found in the literature [21–25].

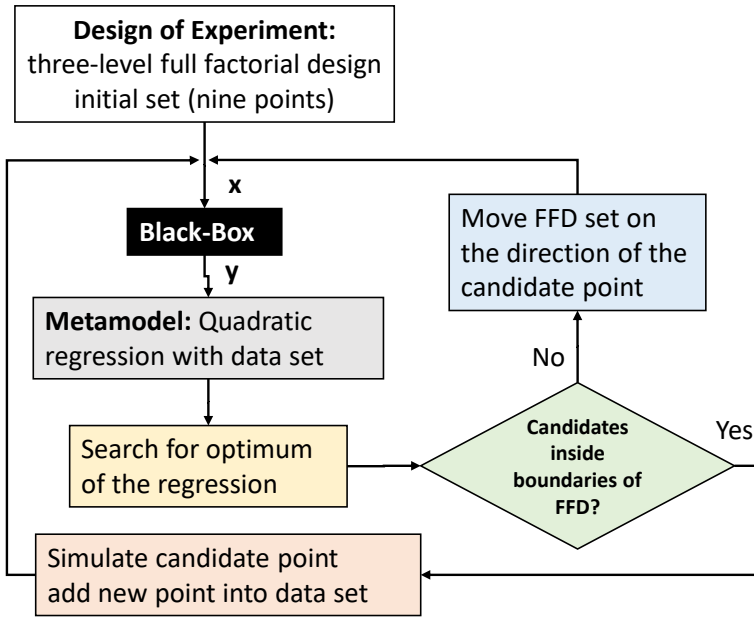


Figure 4.4. Optimization procedure block diagram

Table 4.1 summarizes the variables involved.

Table 4.1. Optimization variables

	Variable	Description
Input	$X = [a, b]$	ABP function parameters
Output	$Y = \text{Torque}$	Average torque output
Objective Function	Black-Box, $Y(X)$	CFD simulation case
Constraint 1	a_{min}, a_{max}	FFD boundary for a
Constraint 2	b_{min}, b_{max}	FFD boundary for b

4.4. Study Case for TSR = 2.3

The simulations will use the parameterized ABP (described in Section 4.2) as input. Since the optimal ABP is likely to be close to the analytic-ABP developed in Section 3.3, we will aim to estimate the parameters a and b that will best reproduce that analytically derived optimal ABP. To this end, (a, b) are obtained from a nonlinear curve fit of the analytic-ABP using equation (4.1) as base function. The parameters a and b were derived heuristically, giving an amplitude of $a = 15.4$ and a skewness of $b = 1.1$; the nonlinear curve fit of the chosen parameters is shown in Figure 4.5. From a curve fit analysis we obtain a maximum error of 6.5° at azimuthal angle 110° ; the root mean square error (RMSE) is 3.09 and the R-square parameter is 0.893. For the purposes of

this work, and as seen in Figure 4.5, the chosen (a, b) provide an adequate starting location to search for the optimal (a, b) .

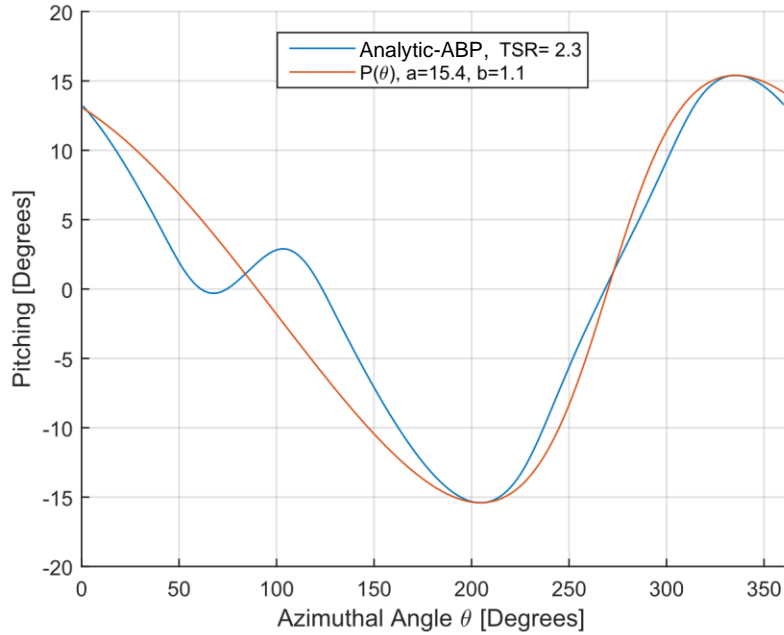


Figure 4.5. Initial parameter values for amplitude a and skewness b

For the three-level FFD initial data set, we have chosen a boundary of $a = [10, 20]$ and $b = [0.5, 1.5]$. The boundaries are at a distance of $(\pm a_{min}, \pm b_{min})$ from the center. The center point is located at $(a, b) = (15, 1)$, which is the rounded value of $(a, b) = (15.4, 1.1)$ previously derived using the nonlinear curve fit. The initial FFD set is shown in Table 4.2 and nine simulations with those parameterized ABPs are run simultaneously. The simulation points of this initial set and the metamodel is shown in Figure 4.6. The equation (4.5) reproduces the quadratic function generated by the regression, an R-square fit coefficient of 0.9999 suggests a strong fit between the base function and data.

$$Y_1(a, b) = 157 - 1.18(a) + 4.86(b) - 0.276(a^2) - 5.83(b^2) + 1.184(ab) \quad (4.5)$$

Table 4.2. Initial FFD set

Point: \vec{X}	Amplitude: a	Skewness: b
1	10	0.5
2	20	0.5
3	15	0.5
4	10	1.5
5	20	1.5
6	15	1.5
7	10	1.0
8	20	1.0
9	15	1.0

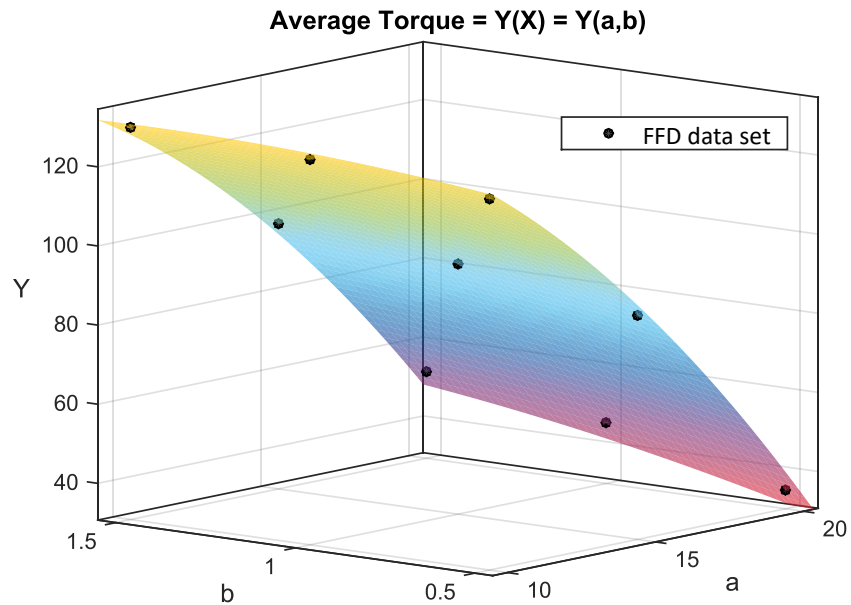


Figure 4.6. First FFD data set and curve fit by quadratic regression

The optimum point candidate acquired from the quadratic regression metamodel ultimately fell outside the design space (optimum not shown in Figure 4.6), so a new data set is placed in the direction of the optimum candidate of the previous regression.

Table 4.3 presents the new FFD set, while Figure 4.7 show the simulation points and metamodel of this set. The quadratic function generated by the regression is presented in equation (4.6); an R-square fit coefficient of 0.9966 suggests a strong fit between the model and data.

$$Y_2(a, b) = 87.9 + 13.13(a) + 3.62(b) - 0.944(a^2) - 0.767(b^2) + 0.046(ab) \quad (4.6)$$

Table 4.3. Second FFD set

Point: \vec{X}	Amplitude: a	Skewness: b
1	5	2.0
2	9	2.0
3	7	2.0
4	5	2.4
5	7	2.4
6	9	2.4
7	5	2.8
8	7	2.8
9	9	2.8

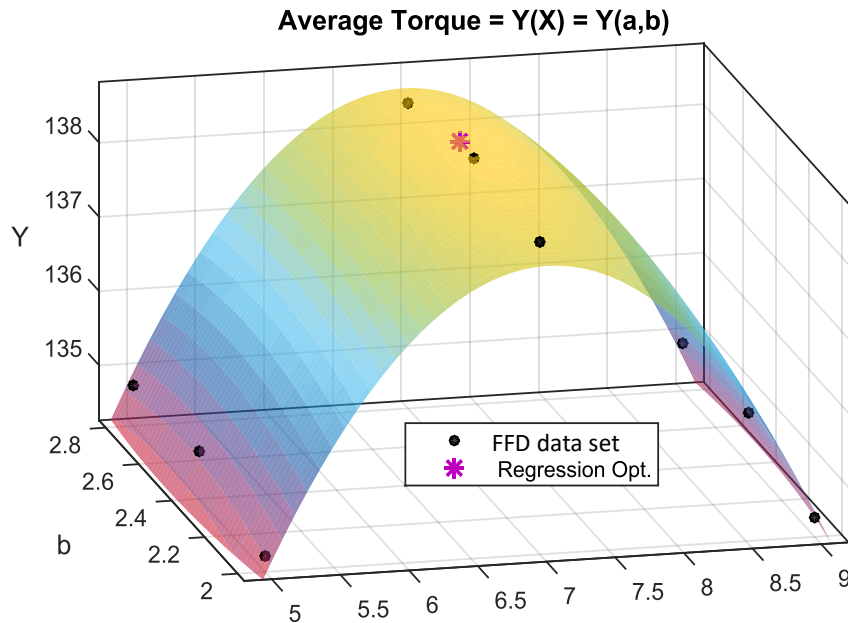


Figure 4.7. Second FFD data set and curve fit by quadratic regression

The optimum of the regression model is $X = [7.01, 2.57]$, the simulation output response of this point is $Y = 138.5$, and the error difference with the central point is negligible and meets convergence criteria, so no more iteration is needed and the procedure terminates.

4.5. Comparison of FFD-ABP Versus Analytic-ABP

The parameter-based FFD-ABP (with $a = 7.01$ and $b = 2.57$) obtained through this chapter's optimization procedure resulted in an increased average torque output of 138.5 Nm compared to the one based on the analytic-ABP strategy (119.5 Nm). The comparison of the two ABP strategies is shown in Figure 4.8 and the torque output profile for both of these strategies is shown in Figure 4.9.

The most notable aspect shown in Figure 4.8 is that the pitching amplitude is reduced in the FFD-ABP. This seems to increase the torque output of the front-swept and back-swept phases (Figure 4.9). Based on the angle-of-attack analysis of Chapter 3, this outcome suggests that there was room to increase the angle of attack in the analytic-ABP. The ABP from the analytic optimization was indeed overpitching to prevent aerodynamic stall. This seems to indicate that stall did occur at angles of attack larger than the critical angle (10°). This effect is supported in current literature, where the stall angle is known to show a hysteresis behavior under a dynamic angle of attack [12] [16] (note that Chapter 3's analysis did not consider dynamic lift and drag coefficients). As the angle of attack increases during the initial trajectory of the front-swept or back-swept phase (Figure 3.4) due to the hysteresis effect, it can go beyond 10° and the blade can keep a higher lift-to-drag ratio and thus higher instantaneous torque. As long as there is no stall at the blade, there is no need to deal with the other side of the hysteresis effect which is to maintain the aerodynamic stall for angles below 10° .

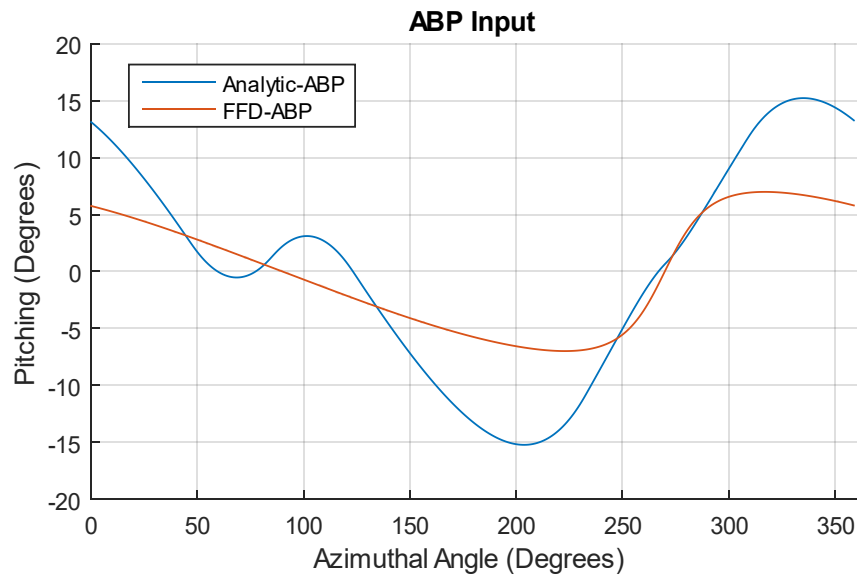


Figure 4.8. Input stimulus for a VAWT blade: analytic-ABP and FFD-ABP

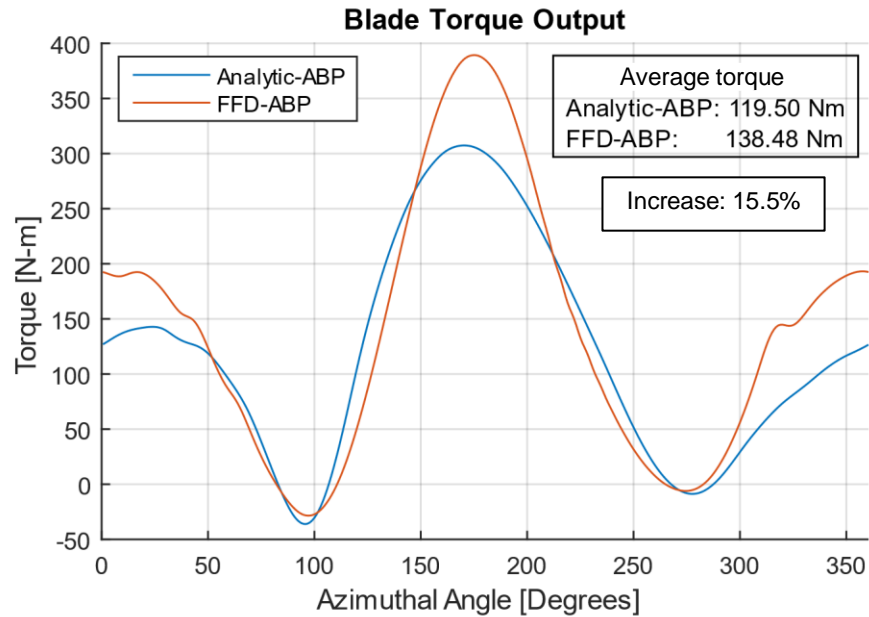


Figure 4.9. Torque output of a VAWT blade using analytic-ABP and optimization-based FFD-ABP, $U_{\infty} = 7.78$, TSR = 2.3

The FFD-ABP strategy achieves a better result than the analytic-ABP because the underlying data for the metamodel was generated using 2D CFD simulations that took into account complex aerodynamic effects such as upwind and downwind flow pattern changes due to VAWT operation and aerodynamic stall hysteresis on the blades. The optimization then corrects the amplitude and skewness in the FFD-ABP to account for these effects. In contrast, complex aerodynamic effects are not considered in the analytic model.

Even though the FFD-ABP obtained a higher optimum value, it required 19 function calls to complete. These were divided into three serial stages: two sets of nine parallel function calls plus the last function call at the end. The next chapter proposes a new optimization methodology that aims to improve the previous result with fewer function evaluations.

Chapter 5.

Optimization of Active Blade Pitching at Discrete Azimuthal Angles

The previous chapter employed a traditional optimization approach to derive an ABP function defined by two parameters (amplitude and skewness). In that approach, the ABP function is limited by two degrees of freedom, but adding more parameters (therefore more degrees of freedom) would increase the required number of function evaluations exponentially. In addition, the previous optimization only considered the average torque, which does not provide any information on the function shape for the instantaneous torque. In this chapter, the optimization procedure is based on the instantaneous pitching and torque data, and aims to improve the power output while keeping the number of function evaluations low.

5.1. Methodology

The procedure aims to construct quadratic metamodels between the pitch angle θ_p and the instantaneous torque T at discretized azimuthal positions θ (in 1° increments). The metamodels are then used to determine the optimal pitch angle at each θ . Since each quadratic regression requires three data points to start, we will need at least three function evaluations. Hence, we begin by running the CFD simulations corresponding to the original analytic-ABP (offset 0°), an analytic-ABP + 2° (offset $+2^\circ$) and an analytic-ABP - 2° (offset -2°). The simulation setup was discussed in Chapter 2. The CFD simulation is run until the instantaneous torque reaches a steady state (refer to Section 2.2.3); note that it uses the instantaneous torque data averaged over the three blades. Once all three simulations have been completed, the first set of metamodels is generated and a discretized optimal $\theta_{p_{opt}}$ is determined for each θ for the whole θ cycle in increments of 1° . In order to approach an optimal ABP progressively, we restrict the metamodel result by constraining θ_p to be no more than 1° outside the current domain. We term the ABP constructed by joining the optimal $\theta_{p_{opt}}$ the first optimal ABP. A follow-up CFD simulation is conducted with the first optimal ABP, and the instantaneous torque data over one whole revolution is recorded. The data sets are updated to include the

latest optimal ABP, and a new set of updated metamodels are generated using the four data sets. The point-wise optimization is repeated to determine a second optimal ABP. A second follow-up CFD simulation is run with the second optimal ABP, and the sequence of steps is repeated until convergence. The convergence criterion is that the torque response of the i th optimal-ABP is within less than 5% difference with the previous $(i - 1)$ th optimal-ABP. Figure 5.1 illustrates the flow chart of the proposed optimization methodology.

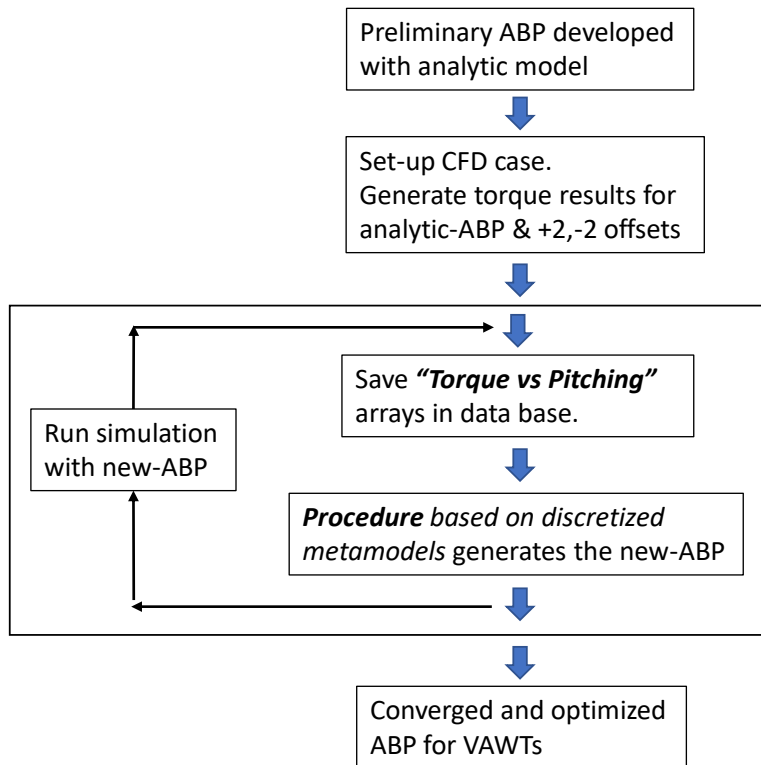


Figure 5.1. Procedure flow diagram for point-wise metamodel optimization

5.2. Initial Data Set Generation

Figure 5.2 shows the analytic-ABP (developed previously in Chapter 3) and two ABP offsets, analytic-ABP $+2^\circ$, and analytic-ABP -2° . As discussed earlier, in order to generate the initial data set for the metamodels, three CFD simulations are needed to generate the blade instantaneous torque; Figure 5.3 shows the correspondent torque versus azimuthal angle for the corresponding ABP strategies. By observing the torque response due to the perturbation of the original analytic-ABP, we can gather useful information on how the ABP should be adjusted to improve the torque response.

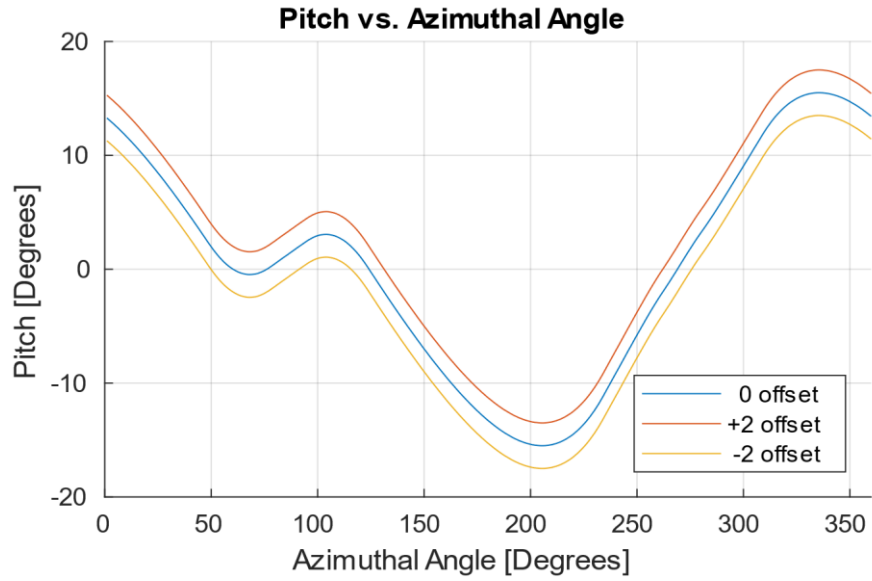


Figure 5.2. Analytic-ABP functions, offsets 0, +2, -2, TSR = 2.3

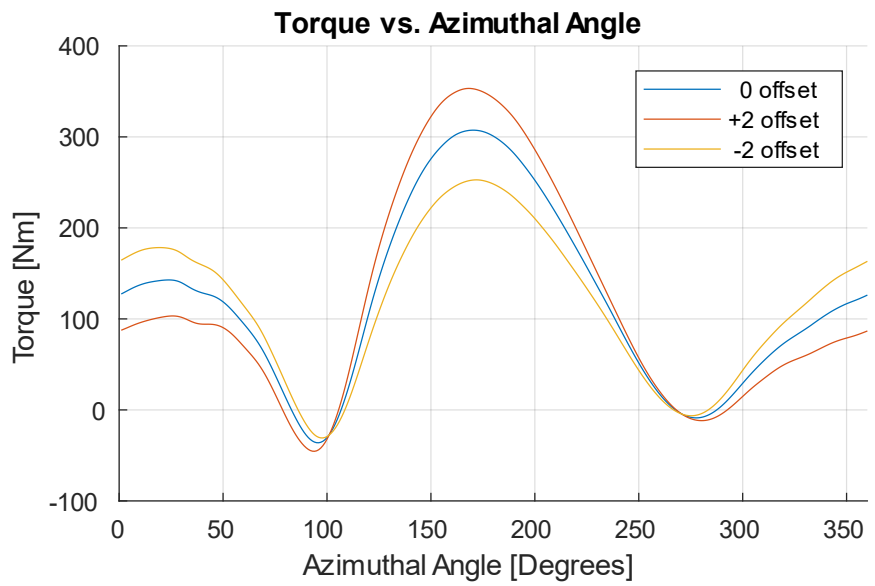


Figure 5.3. Torque output using the three initial ABP functions, TSR = 2.3

5.3. Metamodel Optimization of Torque Versus Pitch

It is clear from Figure 5.3 that there is room for pitch adjustment. Specifically, the instantaneous torque in the upwind swept phases (from 90° to 270°) favors extra positive pitching adjustment while the downwind swept phase favors extra negative pitching adjustment.

- i. The optimum is within the valid domain (this often occurs when $T_0 > T_{-2}, T_{+2}$). This case is better illustrated at an azimuthal angle of 270° ; the metamodel of the torque versus the pitch is shown in Figure 5.4. Here, the regression generates a concave parabola in which the metamodel optimum is in within the domain. This optimum is taken as the optimal blade pitch at 270° .

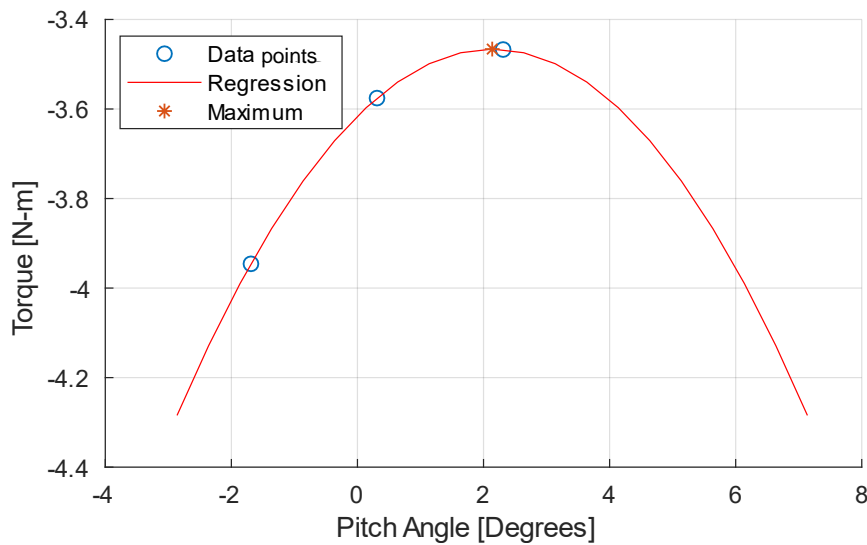


Figure 5.4. Metamodel for three data points at $\theta = 270^\circ$, $TSR = 2.3$

- ii. If the optimum is outside the valid domain, requiring an offset greater than $+2^\circ$; in this case we restrict the ABP to $+1^\circ$ outside the domain. This case can be exemplified at an azimuthal angle of 200° . Here, Figure 5.5 shows the constraint limits of the optimum value defined by the metamodel. The value of 1° encourages slight and gradual variations that will prevent strong variation, thus providing stability. Similarly, if the optimum is outside the valid domain, requiring an offset less than -2° ; in this case we restrict the ABP to -1° outside the domain.

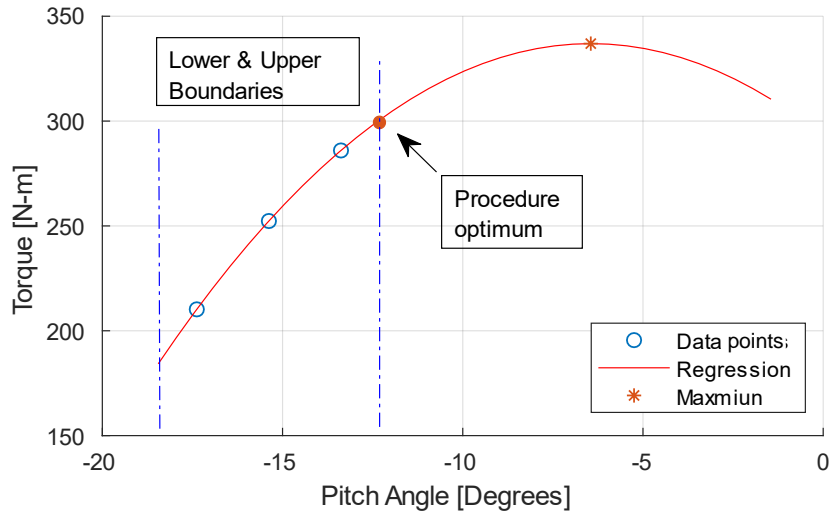


Figure 5.5. Metamodel for three data points at $\theta = 200^\circ$, TSR = 2.3

- iii. For all other cases no valid maximum would exist. However, It may be noted that the majority of the responses correspond to the previous cases, and this case typically occurs when $T_0 \approx T_{-2} \approx T_{+2} \approx 0$. To exemplify this case, Figure 5.6 shows a metamodel with a convex behavior at $\theta = 107^\circ$ (TSR = 3.3 was used as an example here because this case does not exist for TSR = 2.3). The metamodel minimum is taken as the optimal pitch because it is not possible to determine a maximum due to the extremes being in conflict.

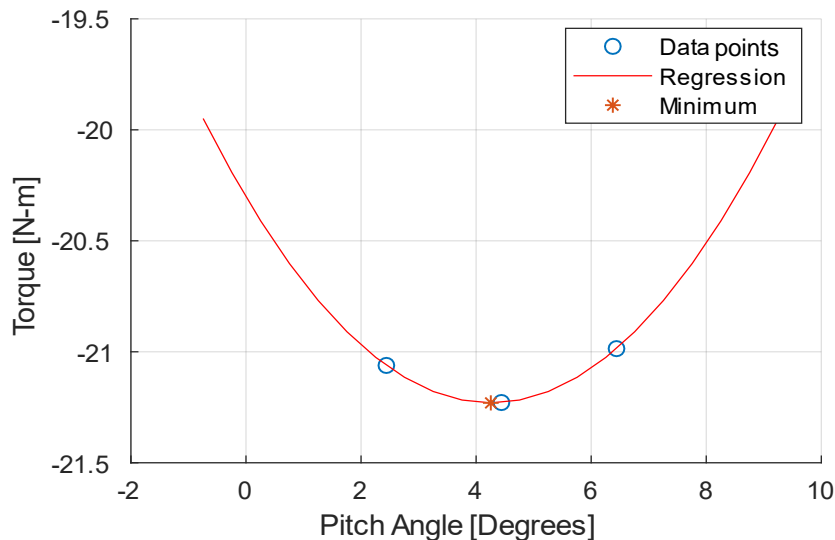


Figure 5.6. Convex metamodel case at $\theta = 107^\circ$, TSR = 3.3

The optimal ABP function is built from the metamodel optimums or their special case equivalents over the whole θ cycle in increments of 1° . In addition, there might be sharp and sudden changes in small azimuthal ranges, and as a consequence, the resulting optimal ABP function is smoothed using a 16-point centered moving average.

5.4. CFD Simulation of the First optimal ABP

The next step is to execute another CFD case with the new optimal ABP to determine the torque output. Figure 5.7 shows the previous and new torque functions corresponding to three previous ABPs and the first optimal ABP. We see from the figure how the metamodel captured the areas which required pitching adjustment, the upwind swept phase (90 to 270°) was positively adjusted while the downwind swept phase was negatively adjusted. The overall increase in average torque is 20%.

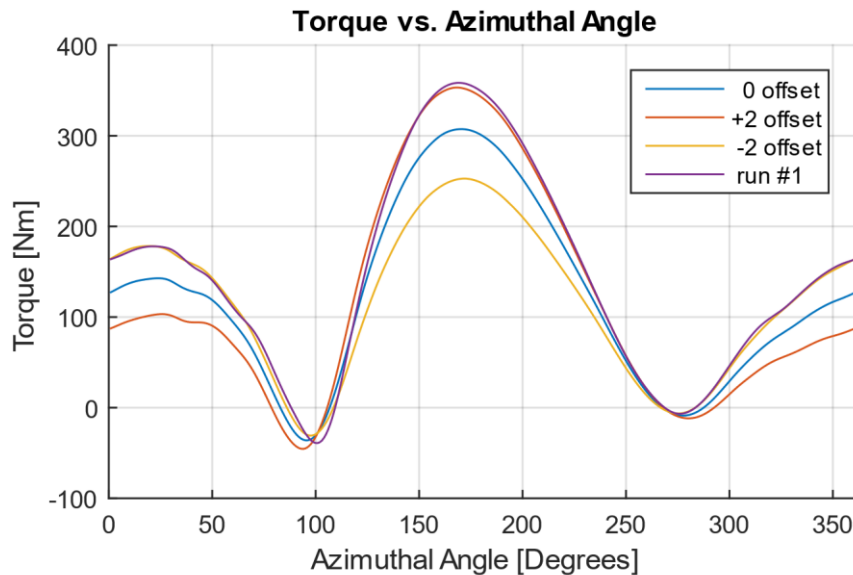


Figure 5.7. Torque output of 1st procedure run, TSR = 2.3

In order to improve the metamodel, we use the preceding input and output data to update the metamodels and repeat the optimization procedure. This is done to progressively approach the optimal ABP while considering the secondary fluid dynamics effects that take place due to a new ABP.

5.5. Iteration and Convergence Procedure

The metamodels are updated with the output data from the first optimal ABP (the metamodel now works with four data sets, the analytic-ABP, its offsets of +2 and -2, and the first optimal ABP). The procedure is re-run to determine a second optimal ABP function. The procedure for updating the metamodel with the simulation results for the $(i - 1)$ th optimum and calculating the i th optimum is repeated until the torque response of the i th optimal-ABP is within 5% of the previous torque response of the $(i - 1)$ th optimal-ABP.

Figure 5.8 and Figure 5.9 show that the ABP and torque functions converge into a narrow band, and that in each subsequent iteration, the increase in the average torque diminishes until it becomes negligible (less than 1%). For subsequent optimization at other TSRs, just two iterations are used, so we effectively use five expensive function calls: the simulation, the analytic-ABP, its offsets +2 and -2, the first optimal-ABP, and the second optimal-ABP. The second optimal-ABP result is considered the optimal-ABP function at the current TSR.

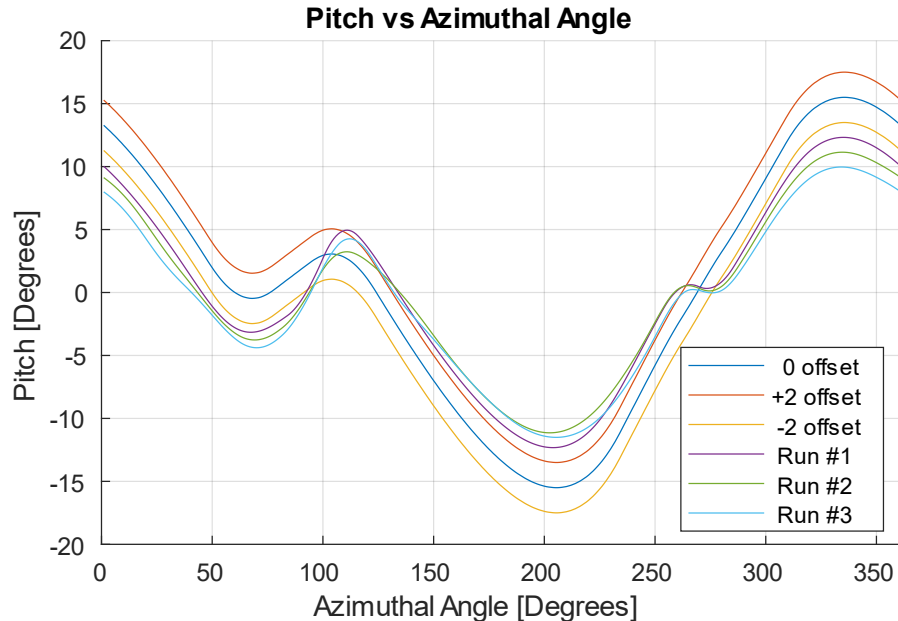


Figure 5.8. Optimum ABP function convergence

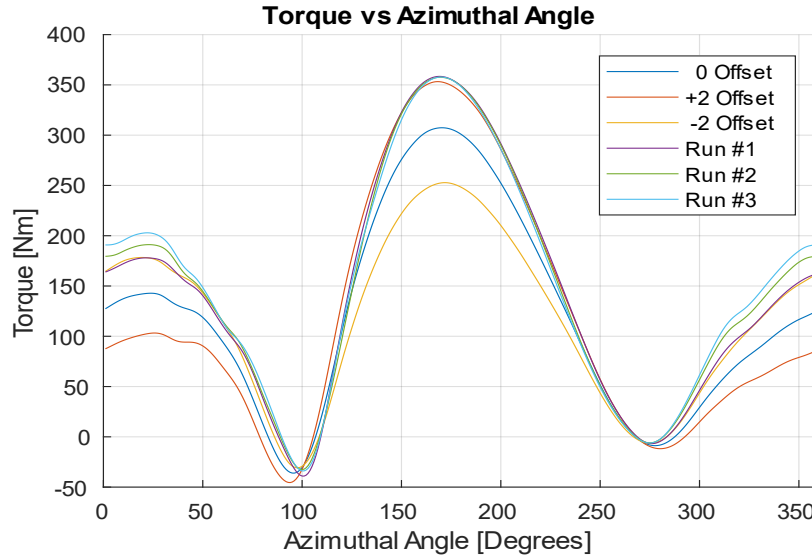


Figure 5.9. Torque function convergence

A MATLAB implementation of the metamodel is presented in Appendix G. It is compatible with the iteration procedure as long as new data is simulated and fed into the metamodel.

5.6. Comparison of Optimal-ABP Versus FFD-ABP

We compare the optimal-ABP obtained with the methodology developed in this chapter with the FFD-ABP (determined in Chapter 4 with a traditional optimization methodology). Both two ABP strategies are shown in Figure 5.10, while Figure 5.11 shows the steady-state blade torque generated by these ABPs. We see that the torque profiles of both ABP strategies are very similar. However, the average torque output generated by the optimal-ABP is 147.5 Nm, which is slightly greater than the previous FFD-ABP of 138.5 Nm. It is important to mention that the number of function calls is reduced from 19 to 5, with both methods having three serial steps.

Figure 5.10 shows that the optimal-ABP, similarly to the FFD-ABP, has a reduced pitching amplitude relative to the analytic-ABP analyzed in Chapter 3. As discussed before, it is likely that the hysteresis of the aerodynamic stall allows the blade angle of attack to increase beyond 10° without stall. Even though the torque profiles of both ABP strategies are very similar, the curvilinear behavior of both ABPs are different, especially at $50^\circ < \theta < 130^\circ$ and at $240^\circ < \theta < 300^\circ$. However, we should notice that these azimuthal angles correspond to the transition from the back-swept to the front-

swept phase and vice versa, and the torque produced in this transition is low or negative [5,6] (as the lift force is collinear to the rotation center during the transition and the VAWT cannot produce positive torque). We conclude that the pitching action at the transition azimuthal angles is not very influential in the torque output profile. Finally, if both ABPs produce a maximum average torque following their respective derivation procedures, we propose that the optimal ABP stimulus might indeed be a family of functions on a band range; these ABP functions would produce a very similar average torque plateau on the VAWT.

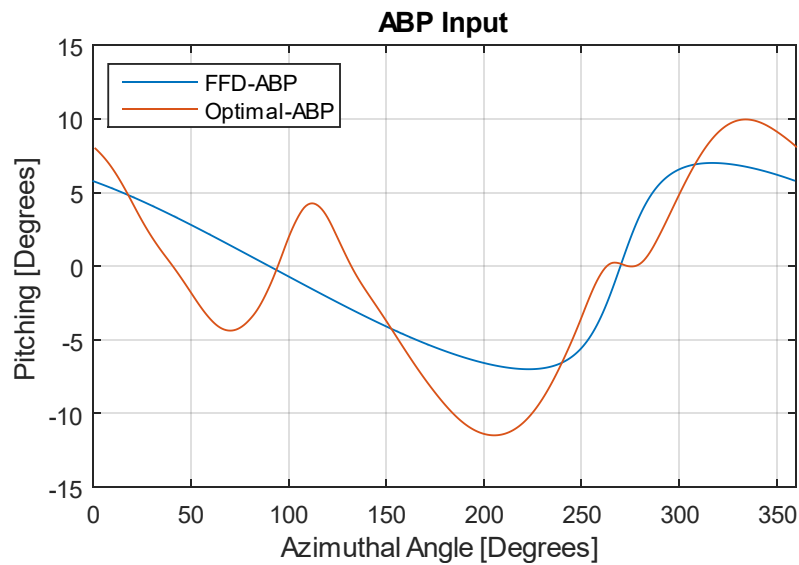


Figure 5.10. Input stimulus for a VAWT blade, FFD-ABP and optimal-ABP

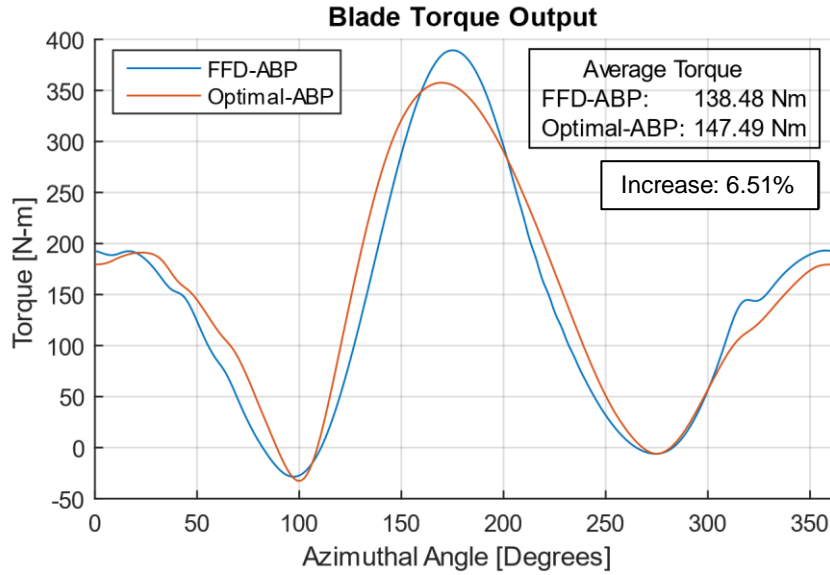


Figure 5.11. Torque output for a VAWT blade, using the FFD-ABP and the optimal-ABP, $U_{\infty} = 7.78$, $TSR = 2.3$

The optimal-ABP function has better quantitative attributes; it has a higher output and was obtained with fewer expensive function calls. The core methodological idea was to use the input and output function data to adjust the input for a better output. In contrast, in the FFD-ABP case, the output data is averaged and the function shape information is lost; consequently, more evaluations might be needed to reach an optimal response. Table 5.1 summarizes the main attributes of the traditional optimization methodology relative to those of the proposed optimization.

Table 5.1. Quantitative attributes of optimization procedures

Quantitative Attributes	Optimal-ABP	FFD-ABP
Function calls	5	19
Optimum value	147.5 Nm	138.5 Nm
Serial steps	3	3

Table 5.2 focuses on a qualitative comparison instead.

Table 5.2. Qualitative attributes of the optimization procedures

Qualitative Attributes	Optimal-ABP	FFD-ABP
Simple solution expression	No	Yes
Convergence speed	Fast	Slow
Computing expense	Low	High
ABP easy to implement in experiments	No	Yes
Easy to provide expression dependent on the TSR	No	No
Easy to converge	Yes	Yes

The optimization developed in this chapter generated a new optimal ABP function that proved to be superior to the previous FFD-ABP. The procedure achieved an optimal result with a low number of function calls. One of the challenges of this study case is that it is necessary to optimize a function instead of a set of values. Traditional optimization procedures require the parameterization of the input and output, but by doing so they constrain the input and lose output information. The solution was to utilize the instantaneous pitch and torque data of three ABP stimuli (original ABP and offsets). This strategy allowed the optimization of the torque versus pitch at discrete azimuthal angles with constrained quadratic regression metamodels. We then built the optimal ABP with metamodel optimum pitch over the entire cycle.

The next chapter will expand this procedure for a wider operating range, which would result in maximum torque and power over the TSR. In addition, we will provide an expression of the optimal pitch as a function of the TSR and θ , and explore the torque behavior at starting (low) TSR.

Chapter 6.

Optimization Procedure Over a Wide TSR Range

From the analytical model of Chapter 3, it is known that ABP is a function of θ and TSR. The previous chapter optimized the ABP function for a single TSR. This chapter extends such procedure for various TSRs (2.3, 2.8, 3.3, 3.8, 4.3), using the results to develop an expression for the optimal ABP as a function of θ and TSR. This chapter also examines the power performance curves (C_p vs. TSR); we find the new maximum power operating point and explore the torque behavior of the VAWT, including its performance at low TSR (TSR of 0.5 and 1.0).

6.1. ABP as a Function of TSR and Azimuthal Angle

The analytic model of Chapter 3 shows that the optimal pitch along a revolution is a function of the TSR; we therefore expect that the ABP obtained from the CFD optimization methodology of Chapter 5 will depend on the TSR as well. Figure 6.1 shows the optimal ABP for various TSRs.

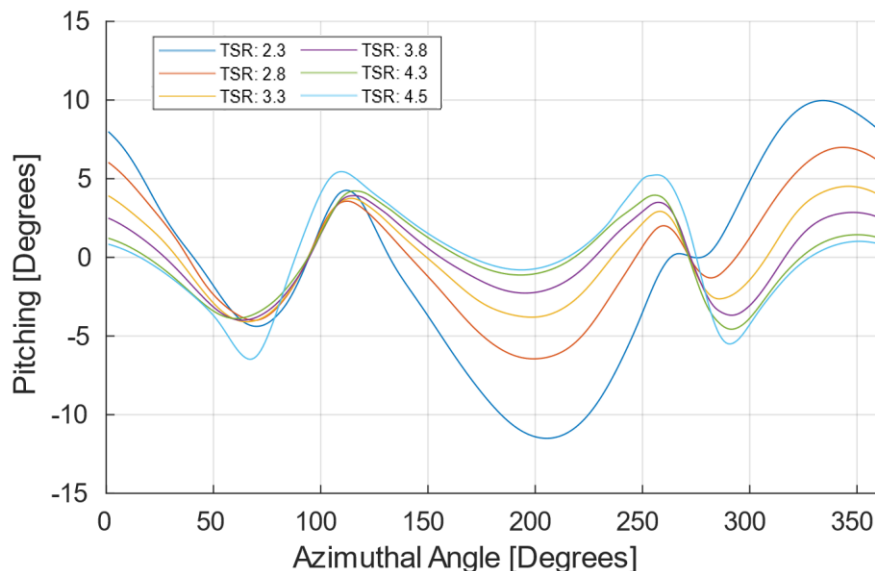


Figure 6.1. Optimized ABP for multiple TSRs

To interpolate between these optimal ABPs, we use a Fourier interpolation function with five coefficients in the form of equation (6.1). The expression would be the base function of the nonlinear surface regression model. The base equation was heuristically built with the following criteria: In order to account for the cyclic behavior of the ABP, a Fourier expansion was chosen to be the base structure, and five harmonics were the smallest number of basic functions that approximate well to the ABP, each one of them composed of a characteristic amplitude and phase that are quadratic functions of the TSR. This allows the surface function to fit well at all ranges of TSR while preserving its cyclic characteristic.

$$ABP(TSR, \theta) = \sum_{i=1}^5 (a_{1i}TSR^2 + b_{1i}TSR + c_{1i}) \cdot \sin(i \cdot \theta + (a_{2i}TSR^2 + b_{2i}TSR + c_{2i})) \quad (6.1)$$

The coefficients a_{1i} , b_{1i} , c_{1i} , a_{2i} , b_{2i} , and c_{2i} are the curve fitting coefficients. The regression analysis was performed using the curve fitting toolbox in MATLAB. The coefficients are provided below in Table 6.1. This regression model for the ABP can be used to transition the VAWT optimally when the TSR changes as a result of changing winds.

Table 6.1. Curve fitting constants

Coefficient	Values					Units
	$i = 1$	$i = 2$	$i = 3$	$i = 4$	$i = 5$	
a_{1i}	1.774	-0.9539	-0.2871	0	0.0823	Nm
b_{1i}	-15.90	8.172	2.114	0.1902	-0.5853	Nm
c_{1i}	34.67	-18.27	-0.968	-0.3252	-0.00293	Nm
a_{2i}	-0.112	0.000	0.020	0.930	2.383	radians
b_{2i}	0.7316	-0.1178	-0.1392	-4.213	-16.18	radians
c_{2i}	0.5074	0.2465	1.735	4.214	26.66	radians

Figure 6.2 shows the ABP curves of Figure 6.1 but plotted on 3D space together with the surface function of equation (6.1) using the coefficients from Table 6.1. We see a good overall fit between the ABP data and the regression model. In order to quantify the data fit, a goodness of fit analysis is done in MATLAB, using the normalized mean square error (NMSE) as cost function. The fit analysis is done by segregating the optimal-ABP (Figure 6.1) and its correspondent regression model data by TSR. A fit (fit_{NMRE}) of 1 represents perfect fit (no error between data and model) while a fit of 0 or lower represents a fit no better than linear regression.

Table 6.2 presents the dependence of the fit on the TSR.

The fit is strong for a TSR of 2.3 ($\text{Fit}_{\text{NMRE}} = 0.9930$) but progressively reduces as the TSR increases to 4.5 ($\text{Fit}_{\text{NMRE}} = 0.6672$). This is explained by the ABP having a strong sinusoidal shape at $\text{TSR} = 2.3$; therefore, fewer Fourier coefficients are needed to approximate the ABP. In contrast, the ABP at $\text{TSR} = 4.5$ significantly differs from a sine function, requiring more Fourier coefficients to approximate the ABP and yielding an inferior fit. The fit improves with the addition of more Fourier coefficients to equation (6.1). However, this increases the complexity of the final equation.

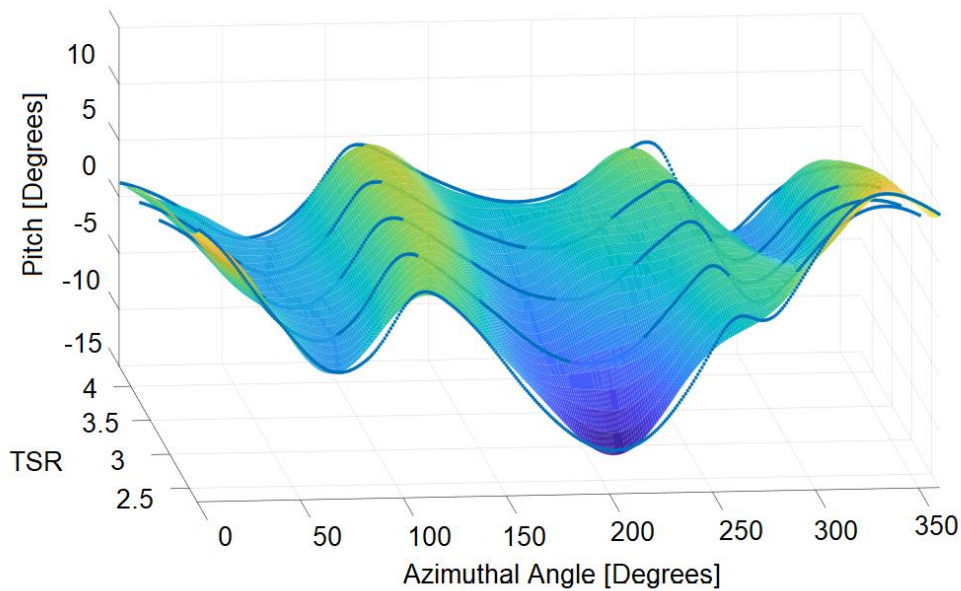


Figure 6.2. 3D surface plot with nonlinear curve fit for optimized pitching

Table 6.2. Normalized mean square error by TSR

TSR:	2.3	2.8	3.3	3.8	4.3	4.5
Fit_{NMRE} :	0.9930	0.9284	0.7178	0.7112	0.9592	0.6672

The surface plot of the ABP in Figure 6.2 follows the explanation given in Chapter 3. The optimal pitch $\theta_{p_{opt}}$ is expressed as $\theta_{p_{opt}} = \alpha_{opt} - \alpha_0$. An analysis of α_{opt} in equation (3.18) show that it will remain relatively constant for various TSR values. This is because α_{opt} would be near the maximum lift to drag ratio (close to aerodynamic stall); in this case $\alpha_{opt} \approx \pm 10^\circ$ (positive at the upwind swept phase and negative at the

downwind swept phase). Subsequently, $\theta_{p_{opt}} \approx 10^\circ - \alpha_0$ (upwind swept phase) and $\theta_{p_{opt}} \approx -10^\circ - \alpha_0$ (downwind swept phase; refer to Chapter 3, Figure 3.4 and Figure 3.5). However, α_0 would not be constant for different TRS values. If we study the function behavior of α_0 , described by equation (3.8), we see that at low TSR, α_0 amplitude variation for a whole cycle is high, while at high TSR, α_0 amplitude variation is low. Figure 6.3 show α_0 for the various TRSs.

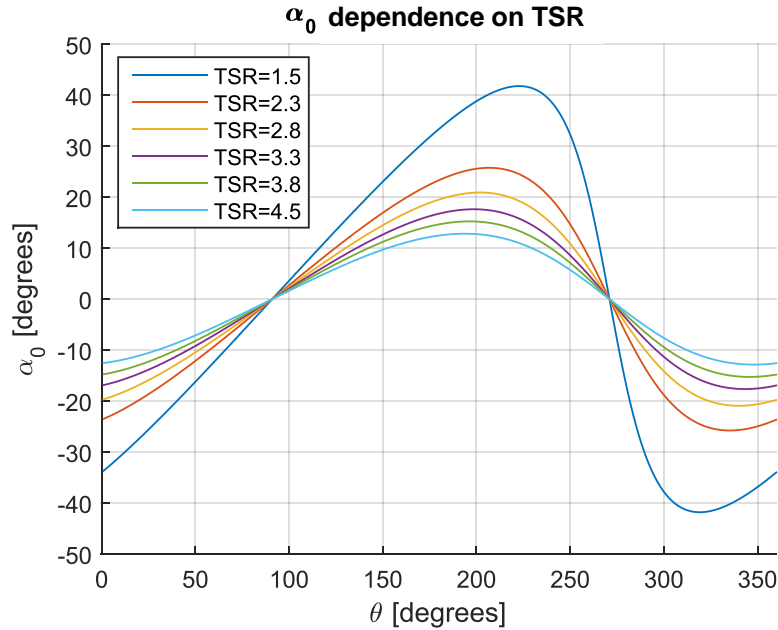


Figure 6.3. Effect of TSR on α_0

From the frame of reference of a VAWT blade, the wind velocity vector \vec{U}_∞ is a cyclic vector that causes the magnitude and angular variation in the vector \vec{U}_{exp} and consequently the variation in α_0 . We conclude that additional compensation is needed at low TSR because of the high α_0 variation, while at high TSR, $\alpha_0 \rightarrow 0$ and the pitching compensation is mainly to reproduce the optimal angle of attack, $\theta_p \rightarrow \alpha_{opt} \approx \pm 10^\circ$.

6.2. Torque Performance Curve

The TSR was varied from 4.5 to 2.3 by varying the wind speed from 3.98 m/s to 7.79 m/s while keeping the rotation speed at 5.97 rad/s. This is the same TSR control strategy used in the validation study. At each TSR the corresponding optimum-ABP is used, namely the ABP functions of Figure 6.1. The average torque (T) of the VAWT over a whole revolution is obtained from the CFD simulations; note that this torque

corresponds to the average torque sum of all three blades. Next, the torque coefficient (C_T) is computed using equation (6.2) for all the TSR cases. We then construct the torque performance curve (C_T vs. TSR) as shown in Figure 6.4.

$$C_T = \frac{T}{0.5\rho ArU_\infty^2} \quad (6.2)$$

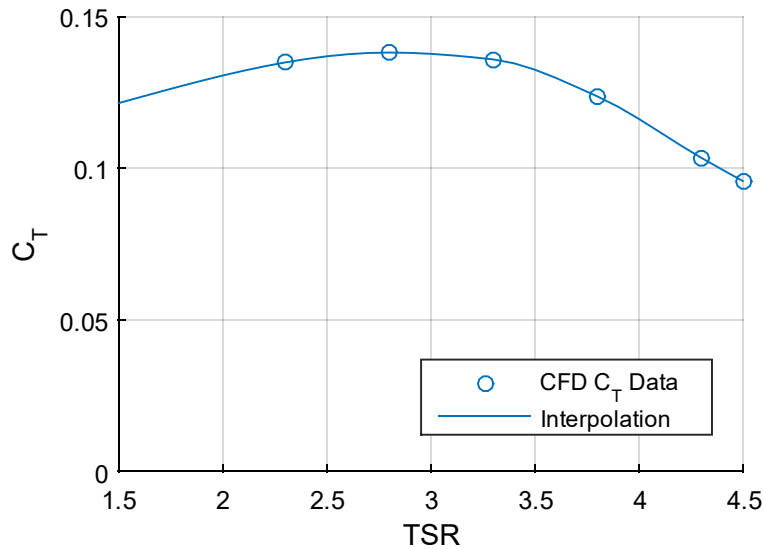


Figure 6.4. Optimal ABP torque performance

Figure 6.4 shows that for TSRs between 2.3 and 3.3 the torque coefficient is fairly constant around 0.13, while for TSRs larger than 3.8 the drag forces appear to become increasingly dominant and the torque begins to decrease, and eventually becomes negative at higher TSRs. This graph is useful for regulating the opposing torque that the generator exerts on the VAWT; the torque is estimated according to the wind conditions and the current rotational speed, and by regulating the electrical power output of the opposing generator the torque may be decreased or increased to stay close to the point of maximum power.

6.3. Power Performance for Maximum Power Tracking

The VAWT power coefficient (C_p) is computed from equation (6.3). Figure 6.5 presents the C_p corresponding to the ABP curves of Figure 6.1. For comparative

analysis, Figure 6.5 also shows the C_p of the fixed pitch strategy obtained during the CFD validations.

$$C_p = C_T \times \text{TSR} \quad (6.3)$$

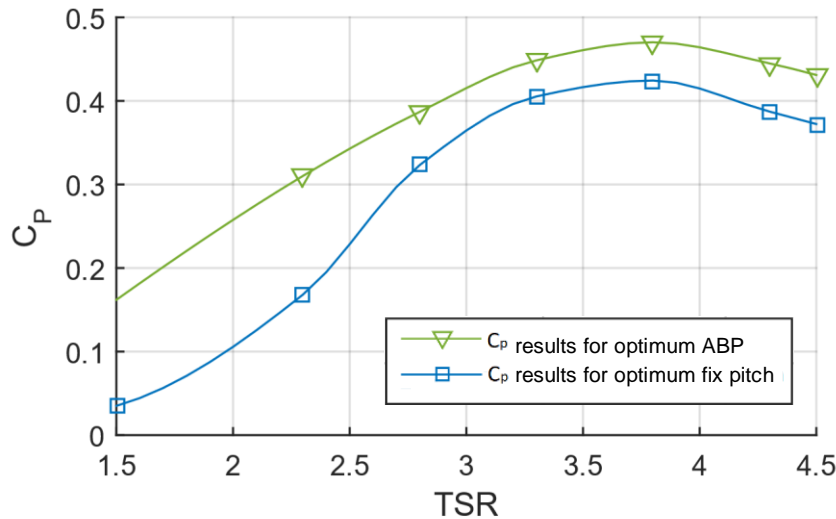


Figure 6.5. Comparison of VAWT C_p performance

Figure 6.5 shows that the maximum C_p is at TSR 3.8, increasing from 0.425 (for a fixed blade of $+2^\circ$) to 0.48, indicating a 13% increase in power. The overall increase in C_p can be attributed to the ability of ABP to suppress the aerodynamic stall on the blades at low TSR and subsequently to reduce the drag and negative torques, while at higher TSR the ABP allows extra lift associated with an optimal angle of attack, which helps to overcome extra drag at higher TSR.

The VAWT will be subject to changing working conditions; as the freestream wind speed changes, we can optimally transition using the ABP formula developed in the previous section, equation (6.1). By governing the ABP and generator rotational speed, it is possible to achieve a better transition, better controllability, a broader operational range, and higher torque at all TSR ranges.

6.4. Torque Performance at Low TSR

The next plots, in Figure 6.6 and Figure 6.7, compare the torque responses of 12-kW VAWT blades under a fixed pitch of 2° and the ABP stimulus derived for a TSR of 2.3. Figure 6.6 is for a TSR of 0.5, and Figure 6.7 for a TSR of 1.0. In both cases, the

ABP stimulus is neither analytically optimized for the corresponding operating condition nor optimized by CFD, yet both plots show clearly that the instantaneous torque is increased for $ABP_{TSR=2.3}$.

These plots show why VAWTs have self-starting problems: the effective wind speed at the blades interacts much faster than the blade sweep along a revolution, generating vortices that interfere with the steady wind required to generate lift, and this effect is in addition to the non-optimal angle of attack discussed in Chapter 3. Finally, even if the ABP is not optimized for the corresponding low TSR, it is more detrimental not to pitch at all; as a consequence, the ABP for regular operating TSR values can still benefit the starting TSR range.

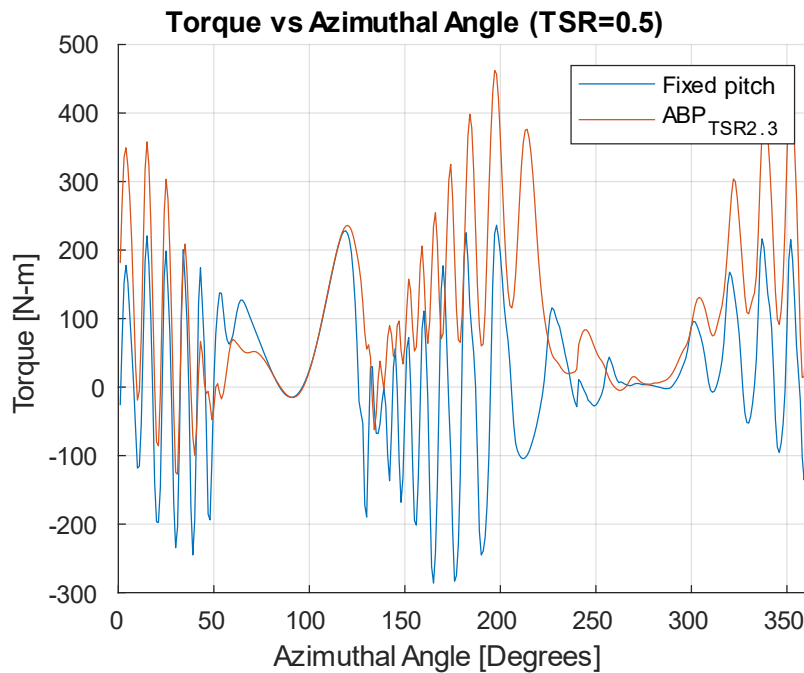


Figure 6.6. Torque profile at TSR = 0.5 for ABP and fixed-pitch strategies

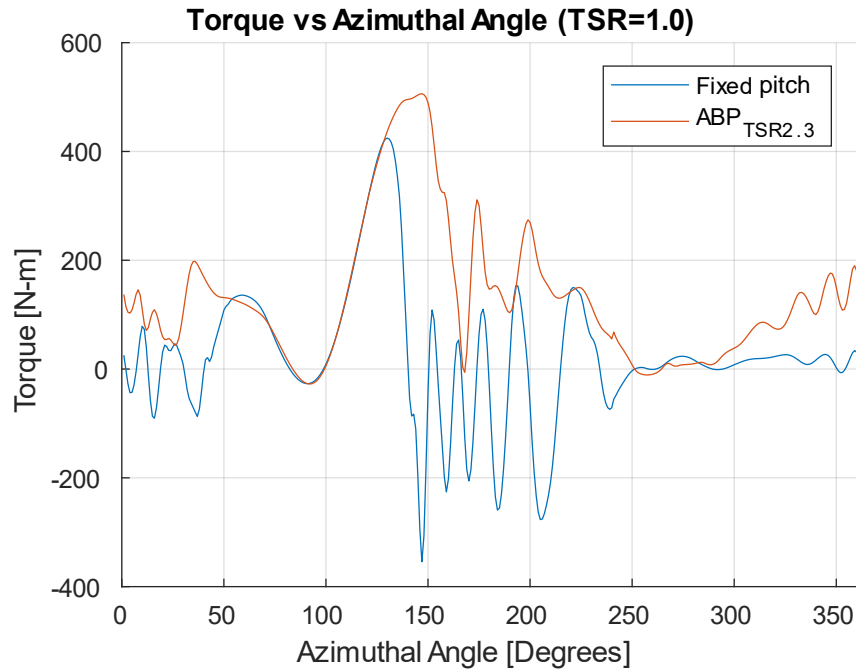


Figure 6.7. Torque profile at TSR= 1.0 for ABP and fixed pitch strategies

Good performance at low TSR can only be achieved with ABP, as it reduces the dynamic stress generated by drag and lift forces (therefore increasing VAWT lifespan) and also improves the self-starting performance of the VAWT due to increased torque.

Chapter 7.

Conclusions and Future Work

This work presents an optimization procedure for ABP of a VAWT over a wide TSR range, using a metamodel fed with CFD simulation data with the transient simulations emulating the ABP by means of dynamic mesh regions.

The optimization procedure begins by estimating the ABP using a preliminary analytic model. The procedure is likely to converge faster if the estimated ABP is close to the optimum. The metamodel initially requires CFD output data; to generate the first data sets we use the first analytical-ABP as well as two perturbations of $+2^\circ$ and -2° offset. The results allow us to generate a modified quadratic regression metamodel of the torque versus the pitch and get the optimum pitch at that azimuthal angle. The new first optimal ABP is simulated for a new CFD case and outperforms its predecessors; the metamodel is then updated with the first optimal ABP, and the procedure is repeated for convergence analysis.

The CFD torque results for a TSR of 2.3 show that the analytic-ABP produces a 33.4% increase in torque compared to the fixed pitch strategy. Later, the ABP function is parameterized, and we perform a traditional optimization to obtain a new control function called FFD-ABP, which increases the torque by 15.5% relative to the analytic-ABP. However, the traditional optimization has some disadvantages such as a high number of function calls. Finally, when the new optimization methodology is employed, it results in a 6.5% increase in torque over the previous FFD-ABP with fewer function calls.

The new optimization procedure was extended to several TSR operating conditions, and an analytic governing formula expressing the pitching as a function of the azimuthal angle and TSR was developed. The equation was constructed using a nonlinear curve fit model. The periodic behavior of the ABP function fitted well to a five-level Fourier expansion in which the harmonics components were dependent on the TSR. Comparing the optimal-ABP with the fixed-pitch results, the point of maximum power operation is increased by 13%, with the overall power performance increase being higher at the lower end of the TSR range. The torque performance at the low TSR

range (from 0 to 1.5) is improved with an ABP derived for $TSR = 2.3$, which suggests that ABP derived for regular operating conditions benefit the self-starting characteristics of the VAWT as well.

The control curve proposed in this work shares similar characteristics with other works that propose control strategies. However, this optimal ABP stand out from the rest because it considers secondary flow effects captured by CFD simulations. To the best of our knowledge, this work is the first of its kind that has implemented a novel CFD-based metamodel optimization over a wide range of TSRs, which is its key contribution to the literature on ABP in VAWTs.

We aim to use the methods developed in this work to produce ABP models for enhancing the self-starting performance of VAWTs, considering a TSR range of 0 to 1. Finally, the metamodel optimization methodology developed in this work is compatible with experimental data (instead of simulation data), for instance by taking torque measurements of the blade using a piezoelectric sensor [28] [29]; use of the proposed work for further experimental research on vertical axis wind turbines is strongly encouraged.

References

- [1] Chen, J. S.-J., Chen, Z., Biswas, S., Miao, J.-J., and Hsieh, C.-H., 2010, "Torque and Power Coefficients of a Vertical Axis Wind Turbine With Optimal Pitch Control," *ASME 2010 Power Conference*, ASME, Chicago, IL, pp. 655–662.
- [2] Shankar, P. N., 1976, "On the Aerodynamic Performance of a Class of Vertical Shaft Windmills," *Proc. R. Soc. A Math. Phys. Eng. Sci.*, **349**(1656), pp. 35–51.
- [3] Miao, J. J., Liang, S. Y., Yu, R. M., Hu, C. C., Leu, T. S., Cheng, J. C., and Chen, S. J., 2012, "Design and Test of a Vertical-Axis Wind Turbine with Pitch Control," *Appl. Mech. Mater.*, **225**, pp. 338–343.
- [4] Glauert, H., 1946, *The Elements of an Airfoil and Airscrew Theory*, Press Syndicate of the University of Cambridge, Cambridge.
- [5] Paraschivoiu, I., 1981, "Double Multiple Streamtube Model for Darrieus Wind Turbines," *DOE/NASE Wind Turbine Dynamics Workshop*, NASA CP-2186, Cleveland, OH, pp. 19–25.
- [6] Gopal B., R., 1976, "The Darrieus Wind Turbine: An Analytical Performance Study," Texas Tech University.
- [7] Hirsch, H., and Mandal, A. C., 1987, "A Cascade Theory for the Aerodynamic Performance of Darrieus Wind Turbines," *Wind Eng.*, **11**(3), pp. 164–175.
- [8] Mandal, A. C., and Burton, J. D., 1994, "The Effects of Dynamic Stall and Flow Curvature on the Aerodynamics of Darrieus Turbines Applying the Cascade Model," *Wind Eng.*, **18**(6), pp. 267–282.
- [9] Strickland JH, Webster BT, N. T., Strickland, J. H., Webster, B. T., Nguyen, T., and Strickland JH, Webster BT, N. T., 1979, "A Vortex Model of the Darrieus Turbine: An Analytical and Experimental Study," *ASME. J. Fluids Eng.*, **101**(4), pp. 500–505.
- [10] Cardona, J. L., 1984, "Flow Curvature and Dynamic Stall Simulated with an Aerodynamic Free-Vortex Model for VAWT," *Wind Eng.*, **8**(3), pp. 135–143.
- [11] Islam, M., Ting, D. S.-K., and Fartaj, A., 2008, "Aerodynamic Models for Darrieus-Type Straight-Bladed Vertical Axis Wind Turbines," *Renew. Sustain. Energy Rev.*, **12**(4), pp. 1087–1109.
- [12] Allet, A., Paraschivoiu, I., and others, 1900, "Aerodynamic Analysis Models for Vertical-Axis Wind Turbines," *Int. J. Rotating Mach.*, **2**(1), pp. 15–21.
- [13] Paraschivoiu, I., 1981, *Double-Multiple Streamtube Model for Daerrius Wind Turbines*.

- [14] Kosaku, T., Sano, M., and Nakatani, K., 2002, "Optimum Pitch Control for Variable-Pitch Vertical-Axis Wind Turbines by a Single Stage Model on the Momentum Theory," *IEEE International Conference on Systems, Man and Cybernetics*, IEEE, Tunisia, p. 6.
- [15] Zhang, L., Liang, Y., Li, E., Zhang, S., and Guo, J., 2012, "Vertical Axis Wind Turbine with Individual Active Blade Pitch Control," *2012 Asia-Pacific Power and Energy Engineering Conference*, IEEE, Shanghai, pp. 1–4.
- [16] Zhang, L. X., Liang, Y. B., Liu, X. H., Jiao, Q. F., and Guo, J., 2015, "Aerodynamic Performance Prediction of Straight-Bladed Vertical Axis Wind Turbine Based on CFD," *Adv. Mech. Eng.*, **5**, pp. 905379–905379.
- [17] Howell, R., Qin, N., Edwards, J., and Durrani, N., 2010, "Wind Tunnel and Numerical Study of a Small Vertical Axis Wind Turbine," *Renew. Energy*, **35**(2), pp. 412–422.
- [18] Rezaeiha, A., Kalkman, I., and Blocken, B., 2017, "Effect of Pitch Angle on Power Performance and Aerodynamics of a Vertical Axis Wind Turbine," *Appl. Energy*, **197**, pp. 132–150.
- [19] Kirke, B. K., and Paillard, B., 2017, "Predicted and Measured Performance of a Vertical Axis Wind Turbine with Passive Variable Pitch Compared to Fixed Pitch," *Wind Eng.*, **41**(1), pp. 74–90.
- [20] Abdalrahman, G., Melek, W., and Lien, F.-S., 2017, "Pitch Angle Control for a Small-Scale Darrieus Vertical Axis Wind Turbine with Straight Blades (H-Type VAWT)," *Renew. Energy*, **114**(July), pp. 1353–1362.
- [21] Montgomery, D. C., 2008, *Design and Analysis of Experiments*, John Wiley & Sons, Hoboken, New Jersey.
- [22] Myers, R. H., 1971, *Response Surface Methodology*, Allyn and Bacon, Boston.
- [23] Haftka, R. T., Scott, E. P., and Cruz, J. R., 1998, "Optimization and Experiments: A Survey," *Appl. Mech. Rev.*, **51**(7), p. 435.
- [24] Gunst, R. F., Myers, R. H., and Montgomery, D. C., 1996, "Response Surface Methodology: Process and Product Optimization Using Designed Experiments," *Technometrics*, **38**(3), p. 285.
- [25] Box, G. E. P., and Draper, N. R., 1987, *Empirical Model-Building and Response Surfaces*, John Wiley and Sons, New York, USA.
- [26] Ferdoues, M. S., Ebrahimi, S., and Vijayaraghavan, K., 2017, "Multi-Objective Optimization of the Design and Operating Point of a New External Axis Wind Turbine," *Energy*, **125**, pp. 643–653.

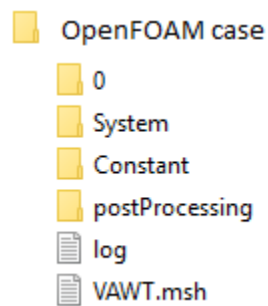
- [27] Ferdoues, M. S., Ebrahimi, S., and Vijayaraghavan, K., 2016, "Optimization of Power and Operation Characteristics of a New External Axis Wind Turbine," *Volume 2A: 42nd Design Automation Conference*, American Society of Mechanical Engineers, Charlotte, North Carolina, USA, p. V02AT03A009.
- [28] Dyachuk, E., Rossander, M., Goude, A., and Bernhoff, H., 2015, "Measurements of the Aerodynamic Normal Forces on a 12-KW Straight-Bladed Vertical Axis Wind Turbine," *Energies*, **8**(8), pp. 8482–8496.
- [29] Rossander, M., Dyachuk, E., Apelfröjd, S., Trolin, K., Goude, A., Bernhoff, H., and Eriksson, S., 2015, "Evaluation of a Blade Force Measurement System for a Vertical Axis Wind Turbine Using Load Cells," *Energies*, **8**(6), pp. 5973–5996.
- [30] Kjellin, J., Bülow, F., Eriksson, S., Deglaire, P., Leijon, M., and Bernhoff, H., 2011, "Power Coefficient Measurement on a 12 KW Straight Bladed Vertical Axis Wind Turbine," *Renew. Energy*, **36**(11), pp. 3050–3053.
- [31] Balduzzi, F., Bianchini, A., Maleci, R., Ferrara, G., and Ferrari, L., 2016, "Critical Issues in the CFD Simulation of Darrieus Wind Turbines," *Renew. Energy*, **85**, pp. 419–435.
- [32] Courant, R., Friedrichs, K., and Lewy, H., 1967, "On the Partial Difference Equations of Mathematical Physics," *IBM J. Res. Dev.*, **11**(2), pp. 215–234.
- [33] Sauvageat, E., Rolin, V., and Port, F., 2016, *Prediction and Comparison of Low-Reynolds Airfoil Performance*, Lausanne (Switzerland).
- [34] Wolfe, W. P., and Ochs, S. S., 1997, "Predicting Aerodynamic Characteristics of Typical Wind Turbine Airfoils Using CFD," *Distribution*.
- [35] Solum, A., Deglaire, P., Eriksson, S., Stålberg, M., Leijon, M., and Bernhoff, H., *Design of a 12kW Vertical Axis Wind Turbine Equipped with a Direct Driven PM Synchronous Generator*, Uppsala.
- [36] Phillips, W. F., and Snyder, D. O., 2000, "Modern Adaptation of Prandtl's Classic Lifting-Line Theory," *J. Aircr.*, **37**(4), pp. 662–670.
- [37] Guermond, J.-L., 1990, "A Generalized Lifting-Line Theory for Curved and Swept Wings," *J. Fluid Mech.*, **211**, pp. 497–513.
- [38] Sheldahl, R. E., and Klimas, P. C., 1981, *Aerodynamic Characteristics of Seven Symmetrical Airfoil Sections through 180-Degree Angle of Attack for Use in Aerodynamic Analysis of Vertical Axis Wind Turbines*, Albuquerque, NM, and Livermore, CA (United States).
- [39] Abbott, I. H., and Von Doenhoff, A. E., 2012, *Theory of Wing Sections: Including a Summary of Airfoil Data*, Courier Dover Publications, New York.

- [40] Greenshields, C., 2016, "OpenFOAM v4 User Guide" [Online]. Available: <https://cfd.direct/openfoam/user-guide-v4/>. [Accessed: 30-Jun-2019].

Appendix A.

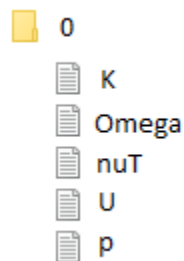
CFD Case Description in OpenFOAM3.0.1

This section describes the CFD case structure in OpenFOAM3.0.1 [40] for the VAWT simulations with ABP. The following structure can be used as a blueprint for similar simulation scenarios. Below we list the files and folders in the first-level structure for the OpenFOAM case.

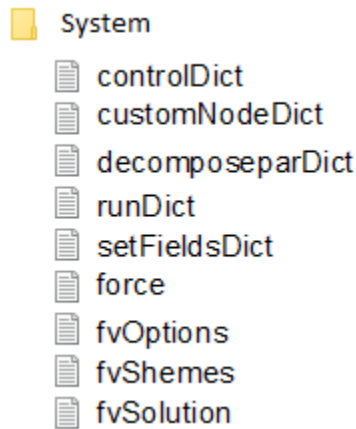


The mesh file (VAWT.msh) is needed to be imported from the Gmsh format into the OpenFOAM2.3.0 format using the command “*gmshToFOAM*”; the mesh format will be generated on dedicated folders inside the “Constant” folder. The “log” folder contains files that show the computation process in real time and is useful for debugging. The “postProcessing” folder contains data that is calculated during the simulation, such as the forces exerted on the blade wall boundary.

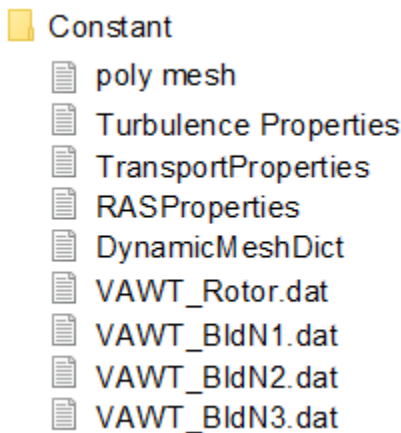
The “0” folder contains the files that specify the initial conditions at time zero, namely the values of the turbulence variables “K”, “Omega”, “nuT”, and the initial values of the pressure and velocity fields (“p” and “U” respectively).



The “System” folder contains files that specify the computational parameters and the data to be extracted for postprocessing. The “controlDict” file contains parameters such as the end time and the time step. Other files specify interpolation/extrapolation solvers, regression solvers, relaxation factors, dynamic mesh handling, and detailed internal computation setup.



The “Constant” folder contains the mesh structure on the “polymesh” folder (generated when importing the mesh), as well as the files that specify constant parameters. The “TurbulenceProperties” and “RASProperties” files define the type of turbulence model and its constants, and the “TransportProperties” define the fluid properties. The “DynamicMeshDict” file defines the movement of the mesh fields; in our case, the movement is taken from the Tabulated data files, which are: “VAWT_Rotor” for the rotor field and “VAWT_BldN#” for the blade fields.



The file scripts of the CFD case can be reviewed in Appendix F. Below are listed the commands needed to start the simulation from the terminal at the folder path.

- of231 // Load OpenFOAM 3.0.1
- gmsh285 // Load Gmsh 2.8.5
- gmshToFOAM VAWT.msh // Import mesh from Gmsh
- pimpleDyMFoam | tee LOG // Execute simulation with specified solver

Appendix B.

Estimation of Drag in VAWT Struts

The struts are rods forming part of the VAWT framework and are designed to resist compression. The struts of the 12-kW VAWT are shown in figure B1.

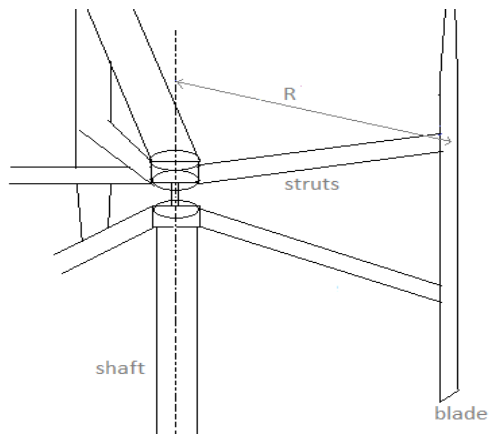


Figure B1. Struts view for VAWT

A first non-exhaustive approach described by blade element theory (BET) considers that the total torque drag T (of one strut) will be the sum of contributions of elements dS along the strut. Each element has a distance S from the hub center and rotates at a distance r from the hub axis after factoring in the angular tilt of 17.6° , while the angular speed is ω . The drag dF_d comes from the relative velocity of the strut element and static air. The model is shown in Figure B2.

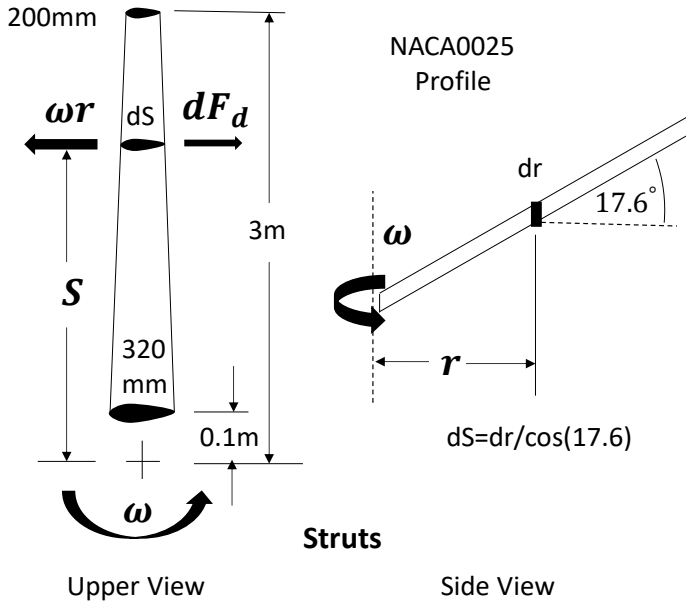


Figure B2. Upper and side view of struts

The above blade element model (BEM) considers only the relative velocity due to the blade rotation; the drag coefficients are taken from static drag tables for NACA0025 [38]. Each element is considered independent and disconnected from the effects of other elements and there are no secondary effects to analyze. The chord length C is 0.32 m at a distance 0.1 m from the hub and linearly reduces to 0.2 m at the tip.

Under the above assumptions, a differential of torque due to an element dS is described by the following equation:

$$dT = dF_d r \quad (B1)$$

Replacing dF_d using the drag coefficient C_d equivalence $dF_d = 1/2\rho(dA)U^2C_d$, where ρ is the air density, dA is a differential area element, and U corresponds to the relative velocity between the element and the static air, we obtain

$$dT = 1/2\rho(dA)U^2C_d r \quad (B2)$$

Further decomposing equation B.2 by the equivalences $dA = C dS$ and $U = \omega r$,

$$dT = 1/2\rho C (dS) \omega^2 r^2 C_d r \quad (B3)$$

The drag coefficient is a function of the angle of attack (fixed at 0) and the Reynolds number, which in turn is a function of the velocity U and chord length C . In this

case, U and C depend on the radial distance r , so C_d is a function of r , the chord length C being a linear function of r ($C = 324.14 - 41.38r$). Furthermore, dS can be decomposed into $dS = dr/\cos(17.6^\circ)$. By regrouping the constants and integrating from radius $r = 0.1$ to $r = 3$, equation B.3 becomes

$$T = \frac{\rho\omega^2}{2\cos(17.6)} \int_{r=0.1}^{r=3} r^3 C_d(r) C(r) dr \quad (\text{B4})$$

We then solve equation B4 for the parameter presented in Table B1. and the strut geometry presented in Section 1.4.

Table B1. Constant Parameter

Parameter	Variable	Value
Rotation speed	ω	5.97 rad/s
Air density	ρ	1.205 kg/m ³
Air viscosity	μ	18.1 μ Pa

The results are shown in Table B2; L represents the function of the integral operation of equation B4.

Table B2. Tabulated values of variables in Equation B4

r	$U(r)$	$C(r)$	$Re(r)$	$C_d(Re)$	r^3	$L = (22.5)r^3 C_d(r) C(r)$
0.1	0.597	0.32000	13E6	0.046	0.001	0.00033
0.5	2.985	0.30450	61E6	0.036	0.125	0.0308
1.0	5.970	0.28276	113E6	0.020	1.000	0.1227
1.5	8.955	0.26207	156E6	0.0175	3.375	0.3483
2.0	11.940	0.24138	192E6	0.015	8.000	0.6517
2.5	14.925	0.22069	230E6	0.014	15.626	1.0863
3.0	17.910	0.20000	297E3	0.013	27.000	1.5795

The curve shown in Figure B3. corresponds to the torque contribution of strut elements along the radius of the VAWT. The area under the curve provides the torque of any given section of strut along the radius of the VAWT. The VAWT is made up of six struts, and the contribution of each strut is 1.513 Nm. Therefore, an estimate of 9 Nm is considered the drag torque due to the six struts rotating at 5.97 rad/s.

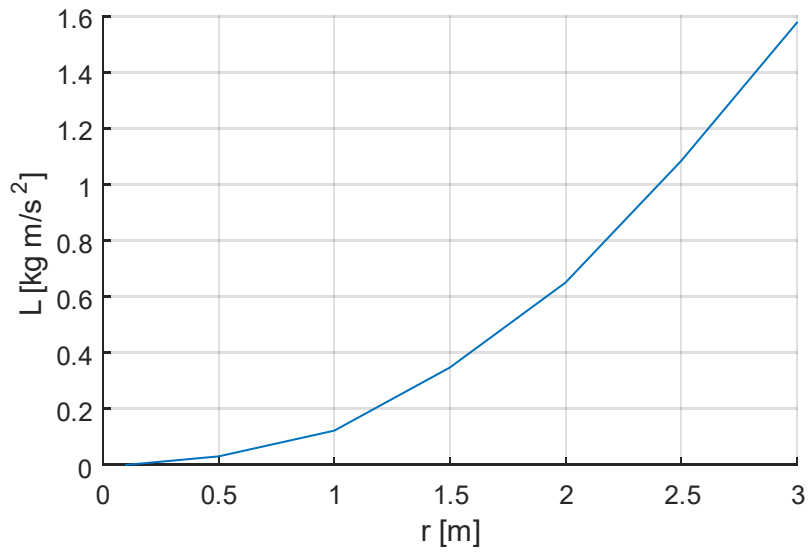


Figure B3. A plot of equation B4; total torque: $T = \int_{r=0.1}^{r=3} L(r)dr = 1.513 \text{ Nm}$

Appendix C.

MATLAB Scripts to Implement the Analytic-ABP

Description:

The following files operate together to implement the analytic-ABP function of this work. These files were written in MATLAB code and are listed in the present appendix. The files functionality is explained, and their code displayed. In order to facilitate the code review and operation, we put together all the files in one compressed folder called “Analytic-ABP_Application” and is included as supplementary material. The code application will start by executing the PitchAng.m file inside.

Filename: Analytic-ABP_Application.rar

The compressed folder contains the following files:

PitchAng.m

This file makes use of several supplementary functions which we define and explain subsequently. This script generates a 360×1 array containing the optimum pitching value for 1° increments in azimuthal angle position (from 0 to 359°). It makes use of the function “OptAtkAng.m” for each azimuthal angle, the raw array is smoothed using a 28-point centered moving average with a user-made function “CurveSmooth.m”.

```
clc;clear;

Re = 80000;    % Reynolds Number      ( cU/v, Global val.)
TSR= 2.0;     % Tip Speed Ratio       (w*R/U, Global val.)
Cu = 57/200;  % Unitary Chord Length (Chord/Radius)

deg=[0:1:359];
for i=1:1:360
theta = i-1
[a_opt(i),a_atk(i),T(i),Fi(i)]=OptAtkAng(theta,Re,TSR,Cu);
end
a_opt2 = CurveSmooth(a_opt,28);
Pitch1 = a_opt - a_atk;
```

```

Pitch2 = a_opt2 - a_atk;
Pitch2 = CurveSmooth(Pitch2,28);

figure; hold on; grid on; plot(deg',[a_atk,a_opt',Pitch1',Pitch2']);
legend('AOA at 0 pitch','AOA optimal','Analytic-ABP raw','Analytic-ABP
smoothed');
xlabel('Azimuthal Angle (Degrees)');
ylabel('Pitch/AOA Angle (Degrees)');
title('Parameters as a function of Azimuthal angle');
%figure; hold on; grid on; plot(Fi);
%figure; hold on; grid on; plot(T);

filename =sprintf('Re%1.0f.TSR%1.1f.txt',Re,TSR);
directory=sprintf('../Tab.Dat.Mov/Pitch_Data/%s',filename)

fileID=fopen(filename,'w')
fprintf(fileID,'%4.2f\n',Pitch2)
fclose(fileID)
movefile(filename,directory,'f')
Matrix=[Pitch1',Pitch2',a_atk',a_opt',Fi',T'];

```

OptAtkAng.m

This function file is responsible for computing the optimal angle of attack relative to the wind velocity experienced by the blade at a certain azimuthal angle. The function considers the vector components of the free wind velocity and rotational velocity to be unaffected by secondary effects and acting directly on the blades. This function file make use of another function called “Torque.m” which computes a dimensionless torque.

```

function [a_opt,AtkAng,T,Fi] = OptAtkAng(theta,Re,TSR,Cu)

Ux_exp = 1 + TSR*sin(theta*pi/180);
Uy_exp = - TSR*cos(theta*pi/180);

Fi = atan2(Uy_exp,Ux_exp);
Fi = Fi*180/pi;
if Fi<0 && theta>180
    Fi=360+Fi;
end

t=-inf;
%A=182;
A=20;
for i=1:1:A+1
    a = A/2+1-i;
    [T(i),P2x(i),P2y(i),Cl(i),Cd(i)] = Torque(Fi,a,Re,TSR,Cu,theta);

```

```

    if T(i)>t
        t = T(i);
        T2 = t;
        a2 = a;
    end
end

a_opt = a2;
T = T2;
AtkAng = theta -90 -Fi;

```

Torque.m

This function computes a dimensionless torque value acting on the VAWT; given a pitch angle, the function computes the torque. It makes use of a function called “NACA4.m” which maps the lift and drag coefficient given the angle of attack of the blade.

```

function [Tu,P2x,P2y,C1,Cd] = Torque(fi,a,Re,TSR,Cu,theta)

fi=fi*pi/180;           % Convert angle from degrees to radians
theta=theta*pi/180;   % Convert angle from degrees to radians

P1x = cos(theta).*cos(fi) + sin(theta).*sin(fi);
P1y = -cos(theta).*sin(fi) + sin(theta).*cos(fi);
P2x = P1x + (Cu/4).*cos(pi+a*pi/180);
P2y = P1y + (Cu/4).*sin(pi+a*pi/180);

Re_L=Re*sqrt((1+TSR*sin(theta))^2+(TSR*cos(theta))^2);
[C1,Cd]=NACA4(Re_L,-a)
Tu = (Re_L^2)*(C1.*P2x - Cd.*P2y);

for i=1:360
Cu(i)=0;
Cu=Cu';
end

```

NACA4.m

This function maps the lift and drag coefficient given the angle of attack of a NACA0021 blade relative to the wind and the Reynolds number, the latter is dependent on the fluid properties, chord length, and wind speed experienced by the blade. This function make use of lift-coefficient and drag-coefficient tables (0021_C1.txt and 0021Cd.txt

respectively). This function interpolates the lift or drag on the 2D space of the Reynolds number and angle of attack domain.

```

function [Cl,Cd] = NACA4(Re,a)
s=1;
if a < 0
    a=-a;
    s=-1;
end

%---- Procedure for Lift Coeff -----

Cl_dat = dlmread('NACA4_DATA/0021_Cl.txt');
[r,c] = size(Cl_dat);
Re_vctr = Cl_dat(1,2:c);
a_vctr = Cl_dat(2:r,1);
Cl_mtrx = Cl_dat(2:r,2:c);

i=1;
while a_vctr(i) < a
    i=i+1;
end
if a_vctr(i) == a
    a1 = a_vctr(i);
    c1 = 0;
else
    a1 = a_vctr(i-1);
    a2 = a_vctr(i);
    c1 = 1;
end

j=1;
while Re_vctr(j) < Re
    j=j+1;
end
if Re_vctr(j) == Re
    Re1 = Re_vctr(j);
    c2 = 0;
elseif Re < Re_vctr(1)
    Re1 = Re_vctr(j);
    c2 = 0;
else
    Re1 = Re_vctr(j-1);
    Re2 = Re_vctr(j);
    c2 = 1;
end

c = c2*10+c1;
switch c
    case 0

```

```

        Cl = Cl_mtrx(i,j);
    case 1
        Cl1= Cl_mtrx(i-1,j);
        Cl2= Cl_mtrx( i ,j);
        Cl = Cl1 + (Cl2-Cl1)*((a-a1)/(a2-a1));
    case 10
        Cl1= Cl_mtrx(i,j-1);
        Cl2= Cl_mtrx(i, j );
        Cl = Cl1 + (Cl2-Cl1)*((Re-Re1)/(Re2-Re1));
    case 11
        Cl11= Cl_mtrx(i-1,j-1);
        Cl12= Cl_mtrx( i ,j-1);
        Cl21= Cl_mtrx(i-1, j );
        Cl22= Cl_mtrx( i , j );
        Cl1 = Cl11 + (Cl12-Cl11)*((a-a1)/(a2-a1));
        Cl2 = Cl21 + (Cl22-Cl21)*((a-a1)/(a2-a1));
        Cl = Cl1 + (Cl2-Cl1)*((Re-Re1)/(Re2-Re1));
end
Cl=Cl*s;

```

```

%---- Procedure for Drag Coeff -----

```

```

Cd_dat = dlmread('NACA4_DATA/0021_Cd.txt');
[r,c] = size(Cd_dat);
Re_vctr = Cd_dat(1,2:c);
Al_vctr = Cd_dat(2:c,1);
Cd_mtrx = Cd_dat(2:r,2:c);
i=1;
while a_vctr(i) < a
    i=i+1;
end
if a_vctr(i) == a
    a1 = a_vctr(i);
    c1 = 0;
else
    a1 = a_vctr(i-1);
    a2 = a_vctr(i);
    c1 = 1;
end

j=1;
while Re_vctr(j) < Re
    j=j+1;
end
if Re_vctr(j) == Re
    Re1 = Re_vctr(j);
    c2 = 0;
elseif Re < Re_vctr(1)
    Re1 = Re_vctr(j);
    c2 = 0;
else
    Re1 = Re_vctr(j-1);

```



```

    Re2 = Re_vctr(j);
    c2 = 1;
end

c = c2*10+c1;
switch c
    case 0
        Cd = Cd_mtrx(i,j);
    case 1
        Cd1= Cd_mtrx(i-1,j);
        Cd2= Cd_mtrx( i ,j);
        Cd = Cd1 + (Cd2-Cd1)*((a-a1)/(a2-a1));
    case 10
        Cd1= Cd_mtrx(i,j-1);
        Cd2= Cd_mtrx(i, j );
        Cd = Cd1 + (Cd2-Cd1)*((Re-Re1)/(Re2-Re1));
    case 11
        Cd11= Cd_mtrx(i-1,j-1);
        Cd12= Cd_mtrx( i ,j-1);
        Cd21= Cd_mtrx(i-1, j );
        Cd22= Cd_mtrx( i , j );
        Cd1 = Cd11 + (Cd12-Cd11)*((a-a1)/(a2-a1));
        Cd2 = Cd21 + (Cd22-Cd21)*((a-a1)/(a2-a1));
        Cd = Cd1 + (Cd2 -Cd1 )*((Re-Re1)/(Re2-Re1));
end
end

```

CurveSmooth.m

```

function Y=CurveSmooth(X,a)
c1= X(1:90);
c2= X(271:360);
A1= [c2,X,c1];
A2= filter(ones(1,a)/a,1,A1);
s = a/2;
Y = A2(91+s:450+s);
end

```

Lift Coefficient Table for NACA4 0021: 0021_CI.txt

	20000	40000	80000	160000	360000	700000	1000000	2000000
0	0.0000	0.0000	0.0000	0.0000	0.0000	0.0000	0.0000	0.0000
1	0.0243	0.0752	0.0921	0.0842	0.1100	0.1100	0.1100	0.1100
2	0.0393	0.1465	0.1839	0.1879	0.2200	0.2200	0.2200	0.2200
3	0.0472	0.2103	0.2731	0.2861	0.3024	0.3300	0.3300	0.3300
4	0.0619	0.2730	0.3564	0.3800	0.4044	0.4128	0.4400	0.4400
5	0.0505	0.3086	0.4320	0.4687	0.4998	0.5146	0.5192	0.5500
6	0.0475	0.3382	0.4953	0.5486	0.5891	0.6100	0.6191	0.6268
7	0.0266	0.3427	0.5445	0.6209	0.6728	0.6988	0.7102	0.7254
8	0.0120	0.3420	0.5751	0.6745	0.7434	0.7802	0.7939	0.8143
9	0.0000	0.3162	0.5874	0.7148	0.8026	0.8493	0.8690	0.8986
10	-0.0100	0.2691	0.5780	0.7374	0.8500	0.9091	0.9364	0.9739
11	-0.0200	0.2176	0.5564	0.7443	0.8779	0.9543	0.9862	1.0398
12	-0.0250	0.1660	0.5228	0.7363	0.8938	0.9843	1.0257	1.0906
13	-0.0200	0.1247	0.4762	0.7178	0.8973	1.0020	1.0492	1.1305
14	-0.0100	0.0833	0.4296	0.6993	0.8937	1.0122	1.0657	1.1580
15	0.0000	0.0907	0.3878	0.6740	0.8840	1.0105	1.0709	1.1747
16	0.0331	0.0981	0.3459	0.6487	0.8717	1.0056	1.0690	1.1823
17	0.0756	0.1300	0.3340	0.6293	0.8603	0.9973	1.0641	1.1824
18	0.1180	0.1619	0.3221	0.6098	0.8489	0.9911	1.0588	1.1814
20	0.2124	0.2414	0.3475	0.5920	0.8397	0.9858	1.0554	1.1812
22	0.3103	0.3345	0.4091	0.6023	0.8453	0.9940	1.0644	1.1893
25	0.4618	0.4802	0.5297	0.6664	0.8866	1.0350	1.1018	1.2230
30	0.8550	0.8550	0.8550	0.8550	0.8550	0.8550	0.8855	0.9550
35	0.9800	0.9800	0.9800	0.9800	0.9800	0.9800	0.9800	0.9800
40	1.0350	1.0350	1.0350	1.0350	1.0350	1.0350	1.0350	1.0350
45	1.0500	1.0500	1.0500	1.0500	1.0500	1.0500	1.0500	1.0500
50	1.0200	1.0200	1.0200	1.0200	1.0200	1.0200	1.0200	1.0200
55	0.9550	0.9550	0.9550	0.9550	0.9550	0.9550	0.9550	0.9550
60	0.8750	0.8750	0.8750	0.8750	0.8750	0.8750	0.8750	0.8750
65	0.7600	0.7600	0.7600	0.7600	0.7600	0.7600	0.7600	0.7600
70	0.6300	0.6300	0.6300	0.6300	0.6300	0.6300	0.6300	0.6300
75	0.5000	0.5000	0.5000	0.5000	0.5000	0.5000	0.5000	0.5000
80	0.3650	0.3650	0.3650	0.3650	0.3650	0.3650	0.3650	0.3650
85	0.2300	0.2300	0.2300	0.2300	0.2300	0.2300	0.2300	0.2300
90	0.0900	0.0900	0.0900	0.0900	0.0900	0.0900	0.0900	0.0900
95	-0.0500	-0.0500	-0.0500	-0.0500	-0.0500	-0.0509	-0.0509	-0.0500
100	-0.1850	-0.1850	-0.1850	-0.1850	-0.1850	-0.1850	-0.1850	-0.1850
105	-0.3200	-0.3200	-0.3200	-0.3200	-0.3200	-0.3200	-0.3200	-0.3200
110	-0.4500	-0.4500	-0.4500	-0.4500	-0.4500	-0.4500	-0.4500	-0.4500
115	-0.5750	-0.5750	-0.5750	-0.5750	-0.5750	-0.5750	-0.5750	-0.5750
120	-0.6700	-0.6700	-0.6700	-0.6700	-0.6700	-0.6700	-0.6700	-0.6700
125	-0.7600	-0.7600	-0.7601	-0.7600	-0.7600	-0.7600	-0.7600	-0.7600
130	-0.8500	-0.8500	-0.8500	-0.8500	-0.8500	-0.8500	-0.8500	-0.8500
135	-0.9300	-0.9300	-0.9300	-0.9300	-0.9300	-0.9300	-0.9300	-0.9300
140	-0.9800	-0.9800	-0.9800	-0.9800	-0.9800	-0.9800	-0.9800	-0.9800
145	-0.9000	-0.9000	-0.9000	-0.9000	-0.9000	-0.9000	-0.9000	-0.9000
150	-0.7700	-0.7700	-0.7700	-0.7700	-0.7700	-0.7700	-0.7700	-0.7700
155	-0.6700	-0.6700	-0.6700	-0.6700	-0.6700	-0.6700	-0.6700	-0.6700
160	-0.6350	-0.6350	-0.6350	-0.6350	-0.6350	-0.6350	-0.6350	-0.6350
165	-0.6800	-0.6800	-0.6800	-0.6800	-0.6800	-0.6800	-0.6800	-0.6800
170	-0.8500	-0.8500	-0.8500	-0.8500	-0.8500	-0.8500	-0.8500	-0.8500
175	-0.6600	-0.6600	-0.6600	-0.6600	-0.6600	-0.6600	-0.6600	-0.6600
180	0.0000	0.0000	0.0000	0.0000	0.0009	0.0000	0.0000	0.0000

Drag Coefficient Table for NACA4 0021: 0021_Cd.txt

	160000	360000	700000	1000000	2000000	5000000
0	0.0103	0.0079	0.0067	0.0065	0.0064	0.0064
1	0.0104	0.0080	0.0068	0.0066	0.0064	0.0064
2	0.0108	0.0084	0.0070	0.0068	0.0066	0.0066
3	0.0114	0.0089	0.0075	0.0071	0.0069	0.0068
4	0.0124	0.0098	0.0083	0.0078	0.0073	0.0072
5	0.0140	0.0113	0.0097	0.0091	0.0081	0.0076
6	0.0152	0.0125	0.0108	0.0101	0.0090	0.0081
7	0.0170	0.0135	0.0118	0.0110	0.0097	0.0086
8	0.0185	0.0153	0.0128	0.0119	0.0105	0.0092
9	0.0203	0.0167	0.0144	0.0134	0.0113	0.0098
10	0.0188	0.0184	0.0159	0.0147	0.0128	0.0106
11	0.0760	0.0204	0.0175	0.0162	0.0140	0.0118
12	0.1340	0.0217	0.0195	0.0180	0.0155	0.0130
13	0.1520	0.0222	0.0216	0.0200	0.0172	0.0143
14	0.1710	0.1060	0.0236	0.0222	0.0191	0.0159
15	0.1900	0.1900	0.1170	0.0245	0.0213	0.0177
16	0.2100	0.2100	0.2100	0.1280	0.0237	0.0198
17	0.2310	0.2310	0.2300	0.2310	0.1380	0.0229
18	0.2520	0.2520	0.2520	0.2520	0.2520	0.1480
19	0.2740	0.2740	0.2740	0.2740	0.2740	0.2740
20	0.2970	0.2970	0.2970	0.2970	0.2970	0.2970
21	0.3200	0.3200	0.3200	0.3200	0.3200	0.3200
22	0.3440	0.3440	0.3440	0.3440	0.3440	0.3440
23	0.3690	0.3690	0.3690	0.3690	0.3690	0.3690
24	0.3940	0.3940	0.3940	0.3940	0.3940	0.3940
25	0.4200	0.4200	0.4200	0.4200	0.4200	0.4200
26	0.4460	0.4460	0.4460	0.4460	0.4460	0.4460
27	0.4730	0.4730	0.4730	0.4730	0.4730	0.4730
30	0.5700	0.5700	0.5700	0.5700	0.5700	0.5700
35	0.7450	0.7450	0.7450	0.7450	0.7450	0.7450
40	0.9200	0.9200	0.9200	0.9200	0.9200	0.9200
45	1.0750	1.0750	1.0750	1.0750	1.0750	1.0750
50	1.2150	1.2150	1.2150	1.2150	1.2150	1.2150
55	1.3450	1.3450	1.3450	1.3450	1.3450	1.3450
60	1.4700	1.4700	1.4700	1.4700	1.4700	1.4700
65	1.5750	1.5750	1.5750	1.5750	1.5750	1.5750
70	1.6650	1.6650	1.6650	1.6650	1.6650	1.6650
75	1.7350	1.7350	1.7350	1.7350	1.7350	1.7350
80	1.7800	1.7800	1.7800	1.7800	1.7800	1.7800
85	1.8000	1.8000	1.8000	1.8000	1.8000	1.8000
90	1.8000	1.8000	1.8000	1.8000	1.8000	1.8000
95	1.7800	1.7800	1.7800	1.7800	1.7800	1.7800
100	1.7500	1.7500	1.7500	1.7500	1.7500	1.7500
105	1.7000	1.7000	1.7000	1.7000	1.7000	1.7000
110	1.6350	1.6350	1.6350	1.6350	1.6350	1.6350
115	1.5550	1.5550	1.5550	1.5550	1.5550	1.5550
120	1.4650	1.4650	1.4650	1.4650	1.4650	1.4650
125	1.3500	1.3500	1.3500	1.3500	1.3500	1.3500
130	1.2250	1.2250	1.2250	1.2250	1.2250	1.2250
135	1.0850	1.0850	1.0850	1.0850	1.0850	1.0850
140	0.9250	0.9250	0.9250	0.9250	0.9250	0.9250
145	0.7550	0.7550	0.7550	0.7550	0.7550	0.7550
150	0.5750	0.5750	0.5750	0.5750	0.5750	0.5750
155	0.4200	0.4200	0.4200	0.4200	0.4200	0.4200
160	0.3200	0.3200	0.3200	0.3200	0.3200	0.3200
165	0.2300	0.2300	0.2300	0.2300	0.2300	0.2300
170	0.1400	0.1400	0.1400	0.1400	0.1400	0.1400
175	0.0550	0.0550	0.0550	0.0550	0.0550	0.0550
180	0.0250	0.0250	0.0250	0.0250	0.0250	0.0250

Appendix D

Mesh Generation Script Files for 2D VAWT Model

Description:

The following files operate together to generate the mesh used for the CFD simulations of this work. The files were written in GMSH code, each file generates a different section of the mesh and their function was explained before on pages 11 and 12 of the thesis. The software GMSH version 2.8.5 (or higher) is recommended for the mesh reconstruction. In order to facilitate the code review, we put together all the mesh generation files in one compressed folder called “12kW_VAWT” which is included as supplementary material. The mesh generation starts by executing the “makemesh” bash script on the Ubuntu terminal command line.

Filename: 12kW_VAWT.rar

- parameters.geo
- NACA4.geo
- Rotor.geo
- Stator.geo
- merge.awk
- makemesh

Appendix E.

Script File for Generating Tabulated Data

Description:

The subsequent file contains the bash script file that is used to generate the arbitrary mesh movement for the different mesh patches. The movement must be in a tabulated data format which is described in Section 2.2.2 of this thesis. In the bash script, there are several user-defined parameters that can be changed manually. Some of those parameters are rotational speed, wind speed, amount of revolutions, etc. These are required to produce the expected movement pattern on the mesh patches. The bash script file for the tabulated data is accompanied by a folder which contains some sample pitching functions, each in a 360-array on a text file. The text file corresponds to the discretized pitching versus azimuthal angle curve over one revolution, and 360 degrees is the discretization in one-degree steps. The data tabulation starts by executing the bash script on the Ubuntu terminal command line.

Filename: Tabulated_Data.rar

Appendix F.

VAWT Simulation Script Files OpenFOAM

Description:

To allow an interested third party to re-do the simulations, we provide in the subsequent files an OpenFOAM CFD case for the 2D 12-kW VAWT model of this thesis. The mesh is already loaded into the CFD case and it is partitioned for parallel simulation of four cores. The simulation examples correspond to the fixed blade case validation study. Therefore, the operating conditions are $TSR = 3.3$ and $\omega = 5.98$. The two folders correspond to the setup in OpenFOAM version 2.3.1 and 3.0.1 respectively, OpenFOAM documentation [40] is provided for additional information on differences between versions.

Filename:

of231_VAWT_TSR3.3_Rev8_FBP2.rar
of301_VAWT_TSR3.3_Rev8_FBP2.rar

The instructions in the Ubuntu terminal command-line to run the CFD case is shown below. The command “of231” is used to load OpenFOAM version 2.3.1 while “of301” is for version 3.0.1.

Command line: ~\$ cd [/Directory/]

Command line: ~[/Directory/]\$ of231

Command line: ~[/Directory/]\$ mpirun -np 4 pimpleDyMFoam -parallel 2>&1 | tee LOG

Appendix G.

Metamodel Implementation in MATLAB

Description:

The metamodel procedure is explained in Chapter 5. In this appendix, we provide the implementation of the metamodel at the 4th iteration for TSR = 3.3. This implies that the torque and ABP results for six previous simulations are already provided. The simulations are the following: The original ABP for TSR = 3.3, the ABP with an offset of +2, the ABP with an offset of -2, The 1st optimal-ABP by the metamodel (which employed the three previous results), the 2nd optimal-ABP, and the 3rd optimal-ABP (which employed all previous results). The file contains six folders with the results of the previous ABP results. The metamodel implementation starts when we execute the MATLAB script file “NewBase.m”, which will process and save the results in a dedicated folder. Support functions scripts are included for further analysis of the results.

Filename: Metamodel_ABP_TSR3.3.rar

To start the metamodel implementation, execute NewBase.m MATLAB script file. Note that the six previous ABP results folders must be in the same directory.

The following folders and files are given in the supplementary material

<i>mesh0_ABP0:</i>	Folder with results of the original analytic-ABP for TSR = 3.3
<i>mesh1_ABP+2:</i>	Folder with results of the analytic-ABP with an offset of +2
<i>mesh2_ABP-2:</i>	Folder with results of the analytic-ABP with an offset of -2
<i>mesh3_run1:</i>	Folder with results of the 1 st run of the metamodel implementation
<i>mesh4_run2:</i>	Folder with results of the 2 nd run of the metamodel implementation
<i>mesh5_run3:</i>	Folder with results of the 3 rd run of the metamodel implementation
Plots:	Result folder with plots generated by the metamodel
<i>NewBase.m:</i>	MATLAB script file which executes the metamodel
<i>CurveSmooth.m:</i>	Support function file for NewBase.m script
<i>NewBaseLine.txt:</i>	Result text file of new optimal-ABP generated by procedure
<i>Torque-per-Run.txt:</i>	Result text file of the torque average of all previous simulations

Appendix H.

Simulation Data and Post-Processed Results

Description:

The data provided in this appendix contain the data and results for all ABP and fixed-pitch simulations for all the TSR operating conditions that were subject to study. This data and processed results are the ones that this thesis utilizes in the tables and figures. The procedure to reproduce the simulations was given in Appendix F, to reproduce the data presented in these files only a few parameters are required change, following the description presented in the chapter of this work.

Filename: Thesis_Data_and_Results.rar

The following folders and files are given in the supplementary material

Metamodel - All TSR: Folder with the post-processed results of all TSR range
Metamodel TSR 2.3: Folder for the metamodel procedure results for TSR = 2.3
Metamodel TSR 2.8: Folder for the metamodel procedure results for TSR = 2.8
Metamodel TSR 3.3: Folder for the metamodel procedure results for TSR = 3.3
Metamodel TSR 3.8: Folder for the metamodel procedure results for TSR = 3.8
Metamodel TSR 4.3: Folder for the metamodel procedure results for TSR = 4.3
Metamodel TSR 4.5: Folder for the metamodel procedure results for TSR = 4.5
VAWT low TSR-ABP: Folder with results of $ABP_{TSR2.3}$ for TSR of 1.0 and 0.5
VAWT low TSR-FP: Folder with fix pitch results for TSR of 0.25, 0.3, 0.5, 0.75, 0.8, 1.0
VAWT Validation: Folder with fix pitch results of the validation procedure
ABP-Index_Ct_Cp: Torque and power coefficients results for ABP simulations
Retrieve Data Steps: Instructions to reproduce the data